Mesoscale Modelling for the Wind Atlas of South Africa (WASA) Project – Phase II

Hahmann, Andrea N.; Pian, Aki; Lennard, Chris; Mortensen, Niels Gylling

Publication date:
2018

Mesoscale Modelling for the Wind Atlas of South Africa (WASA) Project – Phase II

Department of Wind Energy E Report 2019

Andrea N. Hahmann, Aki Pian, Chris Lennard, and Niels G. Mortensen

DTU Wind Energy E-0188

December 2018

DTU Wind Energy
Department of Wind Energy

Authors: Andrea N. Hahmann, Aki Pian, Chris Lennard and Niels G. Mortensen

Title: Mesoscale Modelling for the Wind Atlas of South Africa (WASA) Project – Phase II

DTU Wind Energy E-0188188

December 2018

Summary (max 2000 characters)

This document reports on the methods used to create and the results of the WRF-based numerical wind atlases developed for the Wind Atlas for South Africa Phase 2 (WASA2) project. The report is divided into four main parts. In the first part, we document the method used to run the mesoscale simulations and to generalise the WRF model wind climatologies. The second part compares the results from the downscaled numerical wind atlas against the observed wind statistics from the 15 WASA masts. In the third part, the report documents the variability of the 62 m AGL wind speed at the 15 sites in the seasonal and diurnal time scale and compares it with the WRF-simulated winds. In the last part, we document the preliminary results of the ensemble simulations carried out for WASA2 to estimate the uncertainty of the mesoscale simulations.

There have been various updates from the configuration of the WASA simulations in 2014 documented in Hahmann et al. (2015a). Among the most important:

1. Domain covering all South Africa at 3 1/3 km × 3 1/3 km grid spacing.

2. New atmospheric forcing data from latest reanalysis ERA5 at 0.3° × 0.3° spatial resolution; new high-resolution OSTIA SST at a resolution of 1/20° (approx. 5 km).

3. New land cover and land use dataset from ESA/CCI at 300 m resolution.

4. Increased number of vertical levels, from 41 to 61, which results in a much smaller spacing between levels in the PBL.

5. Use of adaptive time step that considerably speeds up the simulations without loss of quality.

6. New PBL and surface layer parameterizations.

7. New translation table from ESA/CCI land cover types to land surface roughness length adapted for South Africa vegetation types.

ISBN no.
978-87-93549-56-2

Project no.
44032 I-1

Sponsorship
Danida

Front page

Pages: 96
Tables: 6
References:

Technical University of Denmark
Department of Wind Energy
Frederiksborgvej 399
Building 118
4000 Roskilde
Denmark
Telephone 46775027

nimo@dtu.dk
www.vindenergi.dtu.dk

Wind Atlas for South Africa (WASA)

Mesoscale Modelling for the Wind Atlas for South Africa (WASA) Project Phase II

Andrea N. Hahmann, Aki Pian, and Niels G. Mortensen
Technical University of Denmark (DTU)

Chris Lennard
Climate Systems Analysis Group, University of Cape Town (UCT)
Cape Town, South Africa

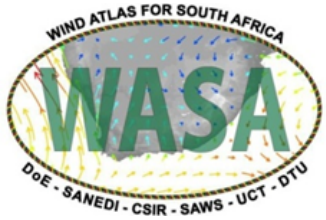

December 2018

Contents

List of Figures

List of Tables

Chapter 1

Introduction

The regional wind climate, i.e. the long-term spatial and temporal distribution of the wind speed and direction over an area of the earth surface, is vital information for locating optimal areas for the siting of wind power plants and for developing regional action plans for reduction of the use of fossil fuels for the generation of electricity. The output from long-term simulations using a mesoscale model is now widely used to generate the wind climatology necessary for calculating the wind energy resources of a given geographical area (Tammelin et al., 2012; Nawri et al., 2014; Hahmann et al., 2015c). These wind climatologies are useful when verified against measurements and serve as input to microscale models for further downscaling (Badger et al., 2014). With this in mind, the main objective of this report is to document the methods used and validate the model results against observations in a similar manner to that done in the mesoscale report to WASA Phase 1 (Hahmann et al., 2015a).

Mesoscale model simulations using the Weather, Research and Forecasting (WRF; Skamarock et al., 2008) model are verified against measurements from the 10 masts in the first phase of the Wind Atlas of South Africa (WASA) and the 5 additional masts installed during the second phase of the project (WASA2). The verification is carried out for the raw WRF winds (Chapter 4) and the downscaled WRF winds (section 4.4.15) using the method described in Chapter 2.

In addition to the verification of the wind atlas, we also present the possibility to estimate the uncertainty of the wind resource estimate based on and ensemble of WRF simulations. These ensemble simulations are created by runs with different physical parameterizations or by introducing variations in the initial atmosphere and surface conditions. The results of the ensemble simulations can be processed to give a "map" of the spread of the wind resource estimation. These method and the preliminary results are presented in Chapter 5.

In Chapter 6 we present the maps of mesoscale simulated winds, geostrophic winds and generalised winds and power densities. The variability of the annual mean annual wind speed are also presented here. Finally in Chapter 7 we summarise the results and offer factors that contribute to the uncertainty of the results.

Chapter 2

Methods

2.1 WRF generalisation

The wind atlas method is based on the generalisation of the wind climatologies derived from the mesoscale modelling. This generalisation post-processing method has been used extensively in a number of wind resource assessment studies.

The post-processing allows a proper verification to be carried out, in which wind climate estimates derived from mesoscale modelling and measurements can be compared. Without the post-processing step no verification is possible, because the surface description within the model does not agree with reality, and therefore model winds will not agree with measured winds, except perhaps in extremely simple terrain or over water far from coasts.

2.1.1 Generalisation parameters

Near-surface winds simulated by a mesoscale model (e.g. WRF) are influenced by the orography and surface roughness length as represented in the mesoscale model and interpreted by the surface and planetary boundary layer (PBL) parameterizations. To free the model output from this dependence, four parameters can be derived from the model orography, that together with boundary layer theory relationships can be used to estimate the wind speed that would be simulated under the idealised conditions of a flat surface with homogeneous standard surface roughness, assuming a stationary flow.

The four parameters are derived from the orography and surface roughness length used in the mesoscale model simulations: (i) a factor that accounts for how the mesoscale model description of the orography impacts the local flow (δA_{oro}), (ii) a parameter that takes into account how the orography alters the mesoscale wind direction ($\delta\phi_{oro}$), (iii) a parameter that accounts for the local flow perturbation on the wind speed due to roughness length variations (δA_{rou}), and finally an (iv) upstream surface roughness length ($\hat{z}_o$). The flow perturbation factors due to orography and roughness depend on the direction and height above ground; the upstream roughness length is only direction dependent. More details on how these parameters are defined and calculated can be found in Badger et al. (2014). These parameters are stored in a netCDF file and used in the generalisation of the WRF time series.

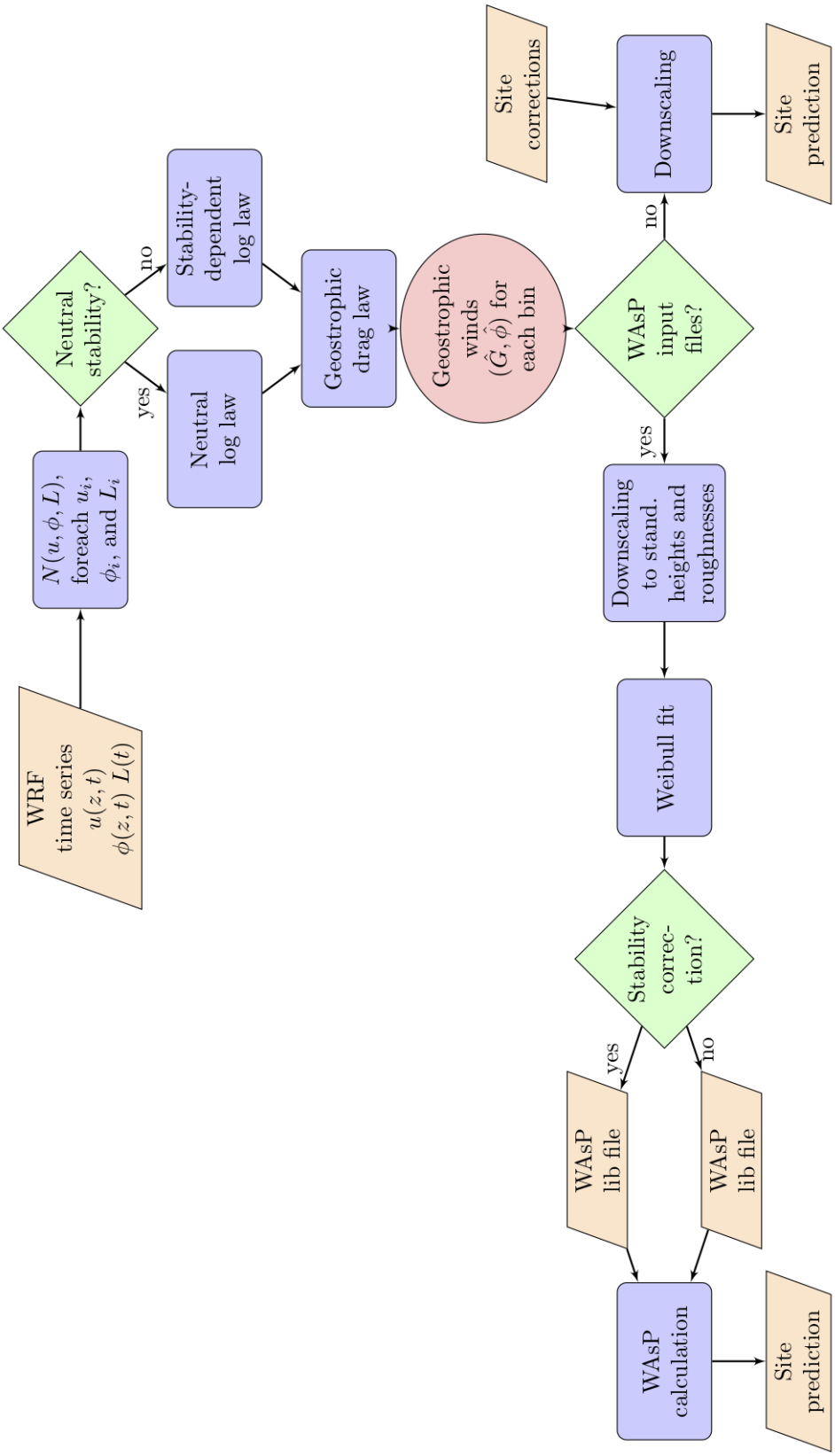

Figure 2.1 – Schematic representation of the generalisation procedure from WRF time series to direct downscaling and lib files.

2.1.2 Sectorisation

The generalisation procedure is schematically explained in Fig. 2.1. To apply it to the WRF-model output, winds from the mesoscale model simulations are binned according to wind speed (usually in 1.0 $\mathrm{m\,s^{-1}}$ bins), wind direction (usually 30 sectors of 10° width) and seven stability class based on the Obukhov length that is also an output from the WRF simulation. The ranges for the stability classes are listed in Table 2.1 together with the "typical" length used in the generalisation.

Table 2.1 – Stability ranges and typical values used in the generalisation procedure.

Stability class	Obukhov length range (m)	Typical Obukhov value $\tilde{L}$ (m)
Very unstable	$-50 < \mathrm{L} < -100$	-75
Unstable	$-100 < \mathrm{L} < -200$	-150
Near unstable	$-200 < \mathrm{L} < -500$	-350
Neutral	$\lvert\mathrm{L}\rvert > 500$	10000
Near stable	$200 < \mathrm{L} < 500$	350
Stable	$50 < \mathrm{L} < 200$	125
Very stable	$10 < \mathrm{L} < 50$	30

The procedure is carried out for each model grid point independently. In practice, time series of wind speed and direction at the desired vertical levels and $1/L$ are extracted from the model output files. The generalisation procedure is then carried out on each time series file.

2.1.3 Basic generalisation equations

In the first step, the time series of wind speed and direction are corrected for orography and roughness change, which are a function of wind direction and height. Given a time series of wind speed, $u = u(z,t)$, and wind direction, $\phi = \phi(z,t)$, which are functions of height and time, intermediate values, $\hat{u}$ and $\hat{\phi}$, are given by

$$\hat{u} = \frac{u}{(1+\delta A_o)(1+\delta A_r)} \tag{2.1}$$

$$\hat{\phi} = \phi - \delta\phi_o, \tag{2.2}$$

where δA_o, $\delta\phi_o$ and δA_r and are generalisation factors for orography in wind speed and direction and roughness change, respectively, described in section 2.1.1 above. From the time series of corrected wind speed and direction "wind classes" are determined. The binning is based on wind direction sectors, wind speed and surface stability according to the Obukhov length as described in section 2.1.2. From the binning, mean values of wind speed, $\overline{u}$, and wind direction, $\overline{\phi}$ and typical Obukhov length $\tilde{L}$, together with the frequency of occurrence, F, of each bin are determined. For simplicity, we will drop the over-bar from the equations that follow, but it is understood that they are applied to the mean values of each bin and not the individual time series values.

From the corrected wind speed value we obtain an intermediary friction velocity, $\hat{u}_*$

$$\hat{u}_* = \frac{\kappa \hat{u}}{\ln[(z/\hat{z}_0) + \psi(z/\tilde{L})]} \tag{2.3}$$

where $\hat{z}_0$ is the downstream surface roughness length and ψ is a stability correction function that adjust the logarithmic wind profile due to non-neutral stability conditions and κ is the von Kármán constant. The stability correction uses the relationship:

$$\psi(z/L) = \begin{cases} -31.58[1 - \exp(-0.19z/L)] & \text{if } x \geq 0 \\ 2\log[0.5(1+x)] + \log[0.5(1+x^2)] - 2\tan^{-1}(x) + 1.5746 & \text{if } x < 0 \end{cases} \tag{2.4}$$

where $x = (1 - 19z/L)$. We use this function with a typical value of the Obukhov length from each wind class bin (see table 2.1). This procedure avoids using the similarity theory on wind profiles that lie outside the bounds of validity of the theory and that sometimes occur in the WRF simulations.

In the next step, we use the geostrophic drag law, which is used for neutral conditions to determine nominal geostrophic wind speeds, $\hat{G}$, and wind directions, α_G, are calculated, using the intermediate friction velocity and wind direction:

$$\hat{G} = \frac{\hat{u}_*}{\kappa} \sqrt{\left(\ln \frac{\hat{u}_*}{f\, \hat{z}_0} - A \right)^2 + B^2}, \tag{2.5}$$

$$\hat{\phi}_G = -sin^{-1} \left(\frac{B\, \hat{u}_*}{\kappa \hat{G}} \right), \tag{2.6}$$

where $A = 1.8$ and $B = 5.4$ are two empirical parameters and f is the Coriolis parameter, and $\hat{\phi}_G$ is the angle between the near-surface winds and the geostrophic wind.

To obtain a new generalised friction velocity, $\hat{u}_{*G}$, for a standard roughness length $z_{0,std}$, Equation 2.5 is reversed by an iterative method,

$$\hat{G} = \frac{\hat{u}_{*G}}{\kappa} \sqrt{\left(\ln \frac{\hat{u}_{*G}}{f\, z_{0,std}} - A \right)^2 + B^2}, \tag{2.7}$$

Finally, the generalised wind speed, u_G, is obtained by using the logarithmic wind profile law

$$u_G = \hat{u}_{*G}\, \kappa\, ln(z/z_{0,std}). \tag{2.8}$$

2.1.4 Weibull distribution fit

The frequency distribution of the horizontal wind speed can often be reasonably well described by the Weibull distribution function (Tuller and Brett, 1984):

$$F(u) = \frac{k_w}{A_w} \left(\frac{u}{A_w} \right)^{k_w - 1} \exp\left[- \left(\frac{u}{A_w} \right)^k \right], \tag{2.9}$$

where $F(u)$ is the frequency of occurrence of the wind speed u. In the Weibull distribution the scale parameter A_w has wind speed units and is proportional to the average wind speed

calculated from the entire distribution. The shape parameter $k(\geq 1)$ describes the skewness of the distribution function. For typical wind speed distributions, the k_w-parameter has values in the range of 2 to 3.

From the values of A_w and k_w, the mean wind speed $\overline{U}$ ($\mathrm{m\,s^{-1}}$) and mean power density $\overline{E}$ ($\mathrm{W\,m^{-2}}$) in the wind can be calculated from:

$$\overline{U} = A_w \Gamma \left(1 + \frac{1}{k_w}\right) \tag{2.10}$$

$$\overline{E} = \frac{1}{2}\rho A_w^3 \cdot \Gamma \left(1 + \frac{3}{k_w}\right) \tag{2.11}$$

where ρ is the mean density of the air and Γ is the gamma function. We use the moment fitting method as used in the Wind Atlas Analysis and Application Program (WAsP) for estimating the Weibull parameters. The method is described in detail in Troen and Petersen (1989). Basically this method estimates A_w and k_w to fit the power density in the time series instead of the mean wind speed.

The Weibull fit is done for the ensemble of wind speeds in each wind direction bin (usually 12 direction sectors) for each standard height (usually 5 heights: 10, 25, 50, 100 and 200 m) and standard roughness lengths (usually 5 roughness: 0.0002 (water), 0.03, 0.1, 0.4, 1.5 m). The 25 Weibull fits for each wind direction sector use the method described above.

This sector-wise transformation of Weibull wind statistics—i.e. transforming the Weibull A_w and k_w parameters to a number of reference heights over flat land having given reference roughnesses—uses not only the geostrophic drag law, but also a perturbation of the drag law, with the latter part including a climatological stability treatment. The transformation and stability calculation is consistent with that implemented in WAsP and outlined in Troen and Petersen (1989), with further details given in Kelly and Troen (2016). The transformation is accomplished via perturbation of both the mean wind and expected long-term variance of wind speed, such that both Weibull-A_w and k_w are affected. When purely neutral conditions (zero stability effects) are presumed for the wind statistics to be transformed, there is still a perturbation introduced, associated with the generalised (reference) conditions in the wind atlas. This perturbation uses the default stability parameter values found in WAsP; it is negated upon subsequent application of the generalised wind from a given reference height and roughness to a site with identical height and surface roughness, using WAsP with its default settings. The climatological stability treatment in the generalisation depends on the unperturbed Weibull parameters and effective surface roughness (Troen and Petersen, 1989), as well as the mesoscale output heights and wind atlas reference heights (though the latter disappears upon application of wind atlas data via WAsP).

Figure 2.2 shows the structure of the resulting WAsP "lib" file. It is structured as Weibull A_w's and k_w's for each sector, height and standard roughness length. The first row contains information about the geographical location of the wind climate represented in the lib-file. The second row lists the number of roughness classes (5), heights (5), and sectors (12), respectively. In the third and fourth row, the actual roughness (m) and heights (m) are listed. Below these header lines, a succession of frequencies of wind direction (1 line), values of Weibull-A_w (1 line) and Weibull-k_w (1 line) for each roughness class and height are printed for each sector (12 sectors per line). This type of file can be used and displayed (Figure 2.3) in WAsP.

WASA_wrf_32.856S_18.111E.lib

```
WASA_wrf   42  124   61 0.1000 <coordinates>18.11099,-32.85556,0.0</coordinates>
  5  5 12
0.000 0.030 0.100 0.400 1.500
 10.0  25.0  50.0 100.0 200.0
11.39  2.24  1.26  1.10  3.40  7.45 24.14 28.33  4.75  3.66  4.14  8.15
 7.13  5.31  1.55  0.91  1.73  5.42  7.00 10.09  5.94  6.06  6.09  6.87
2.150 2.432 0.947 0.732 0.885 1.432 1.572 3.400 1.908 1.967 1.416 1.670
 8.26  5.04  2.63  2.47  2.71  5.71  7.75 10.50  6.60  6.50  6.22  8.01
3.268 1.783 1.393 1.846 1.209 1.436 1.705 2.365 2.139 2.111 1.369 2.029
 8.79  5.32  2.44  2.42  3.82  5.16  9.53 11.35  6.63  6.27  6.66  8.46
3.490 1.748 1.178 1.518 1.736 1.217 2.154 2.752 1.939 1.709 1.404 2.111
 8.79  6.40  3.27  2.66  3.83  7.10 10.72 12.79  6.08  6.26  6.90  8.93
2.076 1.643 1.365 1.229 1.256 1.658 2.229 3.607 1.451 1.506 1.283 1.982
10.16  8.82  3.85  2.99  5.27  7.95 12.64 12.70  5.85  5.28  6.67  9.17
1.971 1.369 1.127 1.189 1.396 1.463 2.365 2.275 1.213 1.100 1.104 1.627
 9.30  1.52  1.12  1.40  4.28  9.59 31.39 18.43  4.84  3.98  3.83 10.31
 4.73  2.38  1.04  1.65  1.31  4.29  6.45  6.71  4.38  4.78  3.62  5.41
1.787 1.100 0.838 1.850 0.787 1.447 1.955 2.607 1.752 2.049 1.037 1.963
 6.07  2.64  1.63  2.07  2.64  4.79  7.76  8.27  4.96  4.93  4.19  6.55
2.670 1.080 1.084 1.752 1.209 1.443 2.479 2.576 1.674 1.588 1.068 2.326
 6.93  3.85  1.84  1.91  2.93  5.59  9.10  9.29  5.36  5.38  5.35  7.61
2.771 1.533 1.092 1.287 1.217 1.607 2.666 2.795 1.654 1.654 1.244 2.803
 8.66  5.18  3.05  3.10  4.54  7.13 11.20 10.64  6.22  6.35  6.23  8.81
3.049 1.611 1.541 1.518 1.459 1.814 3.139 2.627 1.725 1.748 1.299 2.537
11.54  9.40  3.57  3.66  6.35 10.32 13.81 12.94  7.20  6.75  8.55 10.73
2.205 1.674 1.143 1.338 1.506 1.912 2.838 2.561 1.549 1.346 1.420 2.002
 9.20  1.89  0.96  1.91  5.06 12.68 33.25 13.13  4.33  3.82  4.17  9.59
 4.14  1.95  1.16  1.03  1.91  4.11  5.84  5.50  3.71  4.18  3.31  4.75
1.803 1.057 1.100 0.979 0.904 1.787 2.162 2.213 1.670 2.029 1.072 2.029
 5.54  2.20  2.00  2.10  3.24  4.09  6.91  7.14  4.57  4.41  4.10  5.69
```

Figure 2.2 – Structure of a WAsP "lib" file.

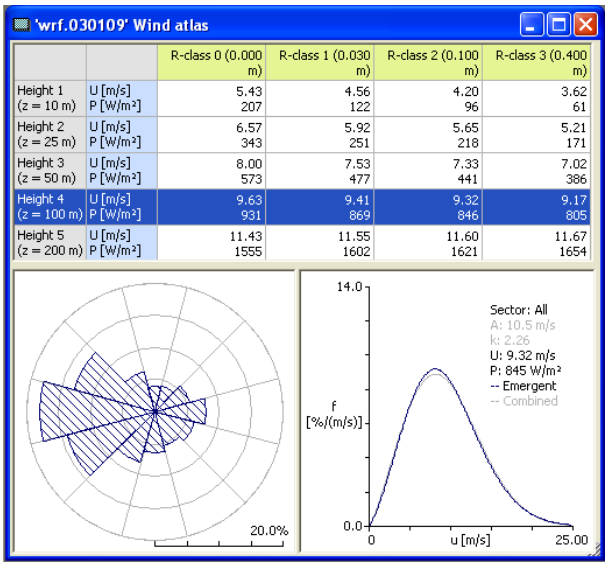

Figure 2.3 – Graphical view of a WAsP "lib" file.

2.1.5 Geostrophic drag law

The geostrophic drag law (GDL) relates the geostrophic wind, u_g, to the flow conditions at the surface, which are described by the friction velocity u_* and the surface roughness z_0. For homogeneous, neutral and barotropic conditions, the GDL is given by Eq. 2.5 (Gill, 1968). Usually, conditions are not homogeneous, neutral and barotropic, and the expressions for A and B in more complex conditions have been discussed by Floors (2013), Kristensen and Jensen (1999), Deacon (1973) and others.

Since the geostrophic drag law should relate the wind at the surface to that above the level at which the surface is 'felt', then it should be sensitive to the precise way in which

energy is removed from the atmosphere by the drag forces at the surface. In the case of a mesoscale model, the way in which the surface interacts with the atmosphere is parametrized in the surface layer and boundary layer physics, and will not necessarily be the same as the relationships in the real atmosphere.

Several approaches could be taken to address this problem: A purely empirical, statistical relationship between the geostrophic wind, surface roughness and friction velocity could be developed. Or, the analytical form of the geostrophic drag law could be retained, but with new, model dependent values for A and B. We chose the second approach, since it retained the latitude dependence of relationship. Homogeneous, near-neutral, barotropic WRF simulations were used, where the geostrophic wind could be reliably calculated from the pressure gradient. Experiments were conducted for a range of surface roughness, geostrophic wind speeds and latitudes. Interestingly, it was found that fitting a single value of A and B for all latitudes gave inferior results, on average, than the standard values. On the other hand, fitting A and B as linear functions of $\sin\phi$, where ϕ is the latitude, gave results with a similar overall error to using the standard values of A and B, but with somewhat different mean winds for the 10 verification sites.

2.2 Wind shear parameter

We use the power exponent parameter α defined from the power law:

$$u(z) = u_r \left(\frac{z}{z_r} \right)^{\alpha}, \tag{2.12}$$

where u_r and z_r are a reference wind speed and height. For a given set of heights, the value of α depends on atmospheric stability and roughness length. Alternatively, Eq. 2.12 can be rewritten as

$$\alpha = \frac{du}{dz}\frac{z}{u}. \tag{2.13}$$

We use the value of α as a diagnostic parameter for the wind shear in the surface layer.

Chapter 3

Mesoscale modelling

3.1 WRF model description

The Weather, Research and Forecasting (WRF) Model (Skamarock et al., 2008) is a mesoscale numerical weather prediction system designed to serve both operational forecasting and atmospheric research needs. The simulations used to generate the WASA numerical wind atlas utilise the Advanced Research WRF (ARW-WRF) version 3.8.1 model released on August 12, 2016. The WRF modelling system is in the public domain and is freely available for community use. It is designed to be a flexible, state-of-the-art atmospheric simulation system that is portable and efficient on available parallel computing platforms. The WRF model is used worldwide for a variety of applications, from real-time weather forecasting, regional climate modelling, to simulating small-scale thunderstorms.

3.2 Model setup

The final simulations for the WASA2 wind atlas were integrated on a grid with horizontal spacing of 30 km $\times$ 30 km (outer domain, d01, with 140 $\times$ 160 grid points), 10 km $\times$ 10 km (first nested domain, d02, with 271 $\times$ 331 grid points) and 3.33 km $\times$ 3.33 km (second nest, d03, with 454 $\times$ 631 grid points). A map of the model setup location, which was rotated to better cover the region of interest over southern Africa, is displayed in Fig. 3.1. Details of the grid projection configuration are given in Table 3.1.

In the vertical the model was configured with 61 levels with model top at 50 hPa. The lowest 20 of these levels are within 1000 m of the surface and the first level is located at approximately 5 m AGL. Table 3.2 list the details of the model configuration, including the model parameterisations used in the simulations.

There have been various updates from the configuration of the WASA simulations in 2014 documented in Hahmann et al. (2015a). Among the most important:

1. Domain covering all South Africa at 3 1/3 km $\times$ 3 1/3 km grid spacing.

2. New atmospheric forcing data from latest reanalysis ERA5 at 0.3° $\times$ 0.3° spacial resolution; new high-resolution OSTIA SST at a resolution of 1/20° (approx. 5km).

3. New land cover and land use dataset from ESA/CCI at 300 m resolution.

Parameter	Value
projection	Lambert conformal
standard longitude	15.0°E
reference longitude	25.0°E
reference latitude	28.5°S
true latitudes	40.0 and 10°S

Table 3.1 – Projection parameters used in the domain setup of the WRF model.

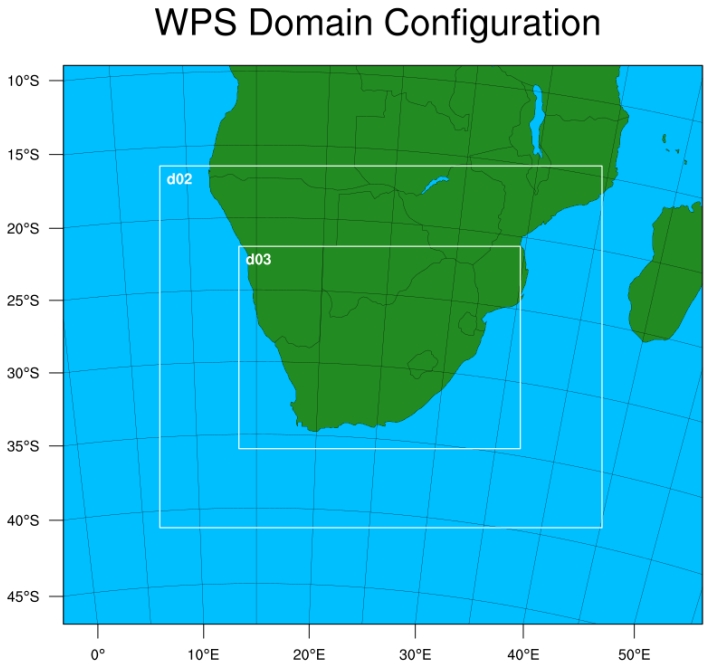

Figure 3.1 – Location of the domains used in the WRF simulations.

4. Increased number of vertical levels, from 41 to 61, which results in a much smaller spacing between levels in the PBL.

5. Use of adaptive time step that considerably speeds up the simulations without lost of quality.

6. New PBL and surface layer parameterizations.

7. New translation table from ESA/CCI land cover types to land surface roughness length adapted for South Africa vegetation types (see section 3.3).

Table 3.2 – Summary of model and physical parameterizations used in the WASA2 simulations.

Model setup:
WRF (ARW) Version 3.8.1. WRF V3.8.1 website
Mother domain (d01; 140 $\times$ 160 grid points) with 30 km grid spacing; 2 nested domains: d02 (271 $\times$ 331 grid points) using 10 km and d03 (454 $\times$ 631 grid points) 3.33 km horizontal grid spacing on a Lambert conformal projection (see Fig. 3.2).
61 vertical levels with model top at 50 hPa; 20 of these levels are placed within 1000 m of the surface; The first 10 levels are located approximately at: 5.6, 21.8, 40.4, 56.6, 72.8, 90.7, 113.2, 140.1, 170.7, 205.3 m.
Land-cover classification from European Space Agency (ESA) Climate Change Initiative land cover maps at 300 m spacial resolution, converted to USGS land categories.
Simulation setup:
Initial, boundary conditions, and fields for grid nudging come from the European Centre for Medium Range Forecast (ECMWF) ERA5 Reanalysis Link to ERA5 description at 0.3° $\times$ 0.3° resolution.
Runs are started (cold start) at 00:00 UTC every 10 days and are integrated for 11 days, the first 24 hours of each simulation are disregarded.
Sea surface temperature (SST) and sea-ice fractions come from the dataset produced at the UK Met Office (OSTIA; Donlon et al., 2011) and are updated daily.
Model output: 30 minutes (lowest 13 vertical levels) for d03. Adaptive time step with maximum allowed CFL of 0.84.
One-way nested domains; 5 grid point nudging zone.
Spectral nudging on d01 only and above level 20; nudging coefficient 0.0003 s^{-1} for wind, temperature and specific humidity. No nudging in the PBL. Min wavelength of 14 and 10 in W-E and S-N directions, respectively.
Physical parameterizations:
Precipitation: WRF Single-Moment 5-class scheme (option 4), Kain-Fritsch cumulus parameterization (option 1) turned off on D3.
Radiation: RRTMG scheme for longwave (option 4); and shortwave (option 1), radiation time step of 12, 9 and 3 minutes, for d01, d02 and d03, respectively.
PBL and land surface: Noah Land Surface Model (option 2) Mellor-Yamada Nakanishi and Niino Level 2.5 PBL scheme (Niino and Nakanishi, 2006) (option 5), MYNN (option 5) surface-layer scheme, modified by setting $\mathrm{bl\_mynn\_mixlength} = 0$ and $\mathrm{COARE\_OPT} = 3.0$.
Diffusion: Simple diffusion (option 1); 2D deformation (option 4); 6th order positive definite numerical diffusion (option 2); rates of 0.06, 0.08, and 0.1 for d01, d02, and d03, respectively; vertical damping.
Positive definite advection of moisture and scalars.

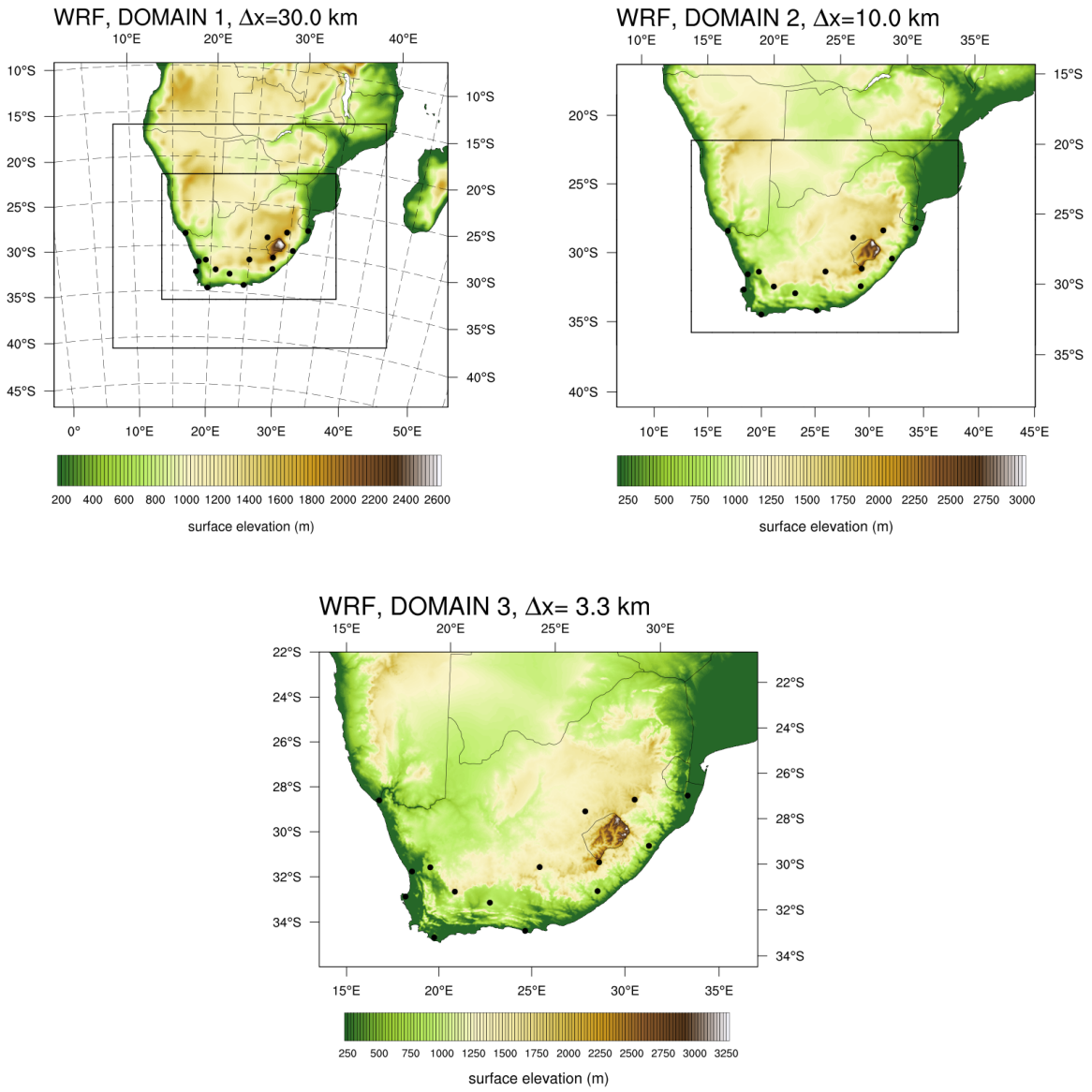

Figure 3.2 – WRF model domains configuration and terrain elevation (m). Top left: 30 km × 30 km domain (d01), Top right: 10 km x 10 km (d02) and Bottom: 3.33 km × 3.33 km (d03). The inner lines show the position of d02 and d03 in d01 and d02, respectively. The location of the WASA masts is shown by the dots.

Most choices in the model setup are fairly standard and used by other modelling groups. The only special setting for wind energy applications is the use of a constant surface roughness length, thus disabling the annual cycle available in the WRF model. This choice is consistent with the generalisation procedure discussed in Chapter 2.

The final simulation covered the period January 2010 – April 2018, and were run in a series of 11-day long overlapping simulations, with the output from the first day being discarded. This method is based on the assumptions described in Hahmann et al. (2010). The simulation used grid nudging that continuously relaxes the model solution towards the gridded reanalysis but this was done only on the outer domain and above the boundary layer (level 20 from the surface) to allow for the mesoscale processes near the surface to develop freely. Because the

simulations were re-initialised every 10 days, the runs are independent of each other and can be integrated in parallel reducing the total time needed to complete a multi-year climatology. The spectral nudging and 10-days re-initialisation keeps the model solution from drifting from the observed large-scale atmospheric patterns, while the relatively long simulations guarantee that the mesoscale flow is fully in equilibrium with the mesoscale characteristic of the terrain.

One major change to the standard WRF modelling system was the change in landuse (and its associated surface roughness length) for the WASA simulations. Detailed inspection of the standard landuse maps in WRF showed serious problems. The new map based on the ESA/CCI dataset is presented in Fig. 3.3.

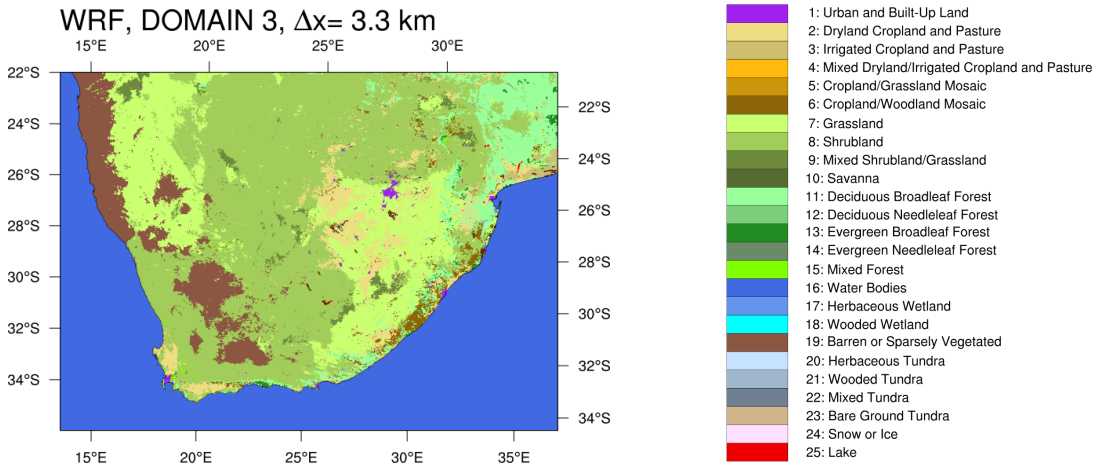

Figure 3.3 – WRF landuse map derived from the ESA/CCI global land cover map.

3.3 Updated vegetation

Surface roughness were modified from those used in the standard WRF V3.8.1 setup for USGS. The new values are presented in Table 3.3. In addition to the new values, the annual variation in surface roughness used in WRF was disabled by setting the minimum and maximum values to a single value. The modified values are presented in Table 3.3. Grasslands and shrublands have lower roughness lengths in the WASA simulations, while all forest roughness lengths have been increased from 0.5 to 0.6 m. The resulting surface roughness map is presented in Fig. 3.3.

Table 3.3 – Surface roughness length as a function of landuse class for the standard WRF (minimum and maximum) and the modified for the WASA simulations.

Min/Max stand roughness (m)	New roughness (m)	USGS landuse class (class number)
0.05/0.15	0.05	dryland cropland and pasture (2)
0.02/0.10	0.05	irrigated cropland and pasture (3)
0.05/0.15	0.05	mixed dryland/irrigated cropland and pasture (4)
0.05/0.14	0.10	cropland/grassland mosaic (5)
0.10/0.12	0.05	grassland (7)
0.01/0.05	0.03	shrubland (8)
0.01/0.06	0.05	mixed shrubland/grassland (9)
0.50/0.50	0.60	deciduous broadleaf forest (11)
0.50/0.50	0.60	deciduous needleleaf forest (12)
0.50/0.50	0.60	evergreen broadleaf forest (13)
0.50/0.50	0.60	evergreen needleleaf forest (14)
0.20/0.50	0.30	mixed forest (15)
0.20/0.20	0.001	herbaceous wetland (new tidal zone) (17)
0.05/0.10	0.05	bare ground tundra (23)

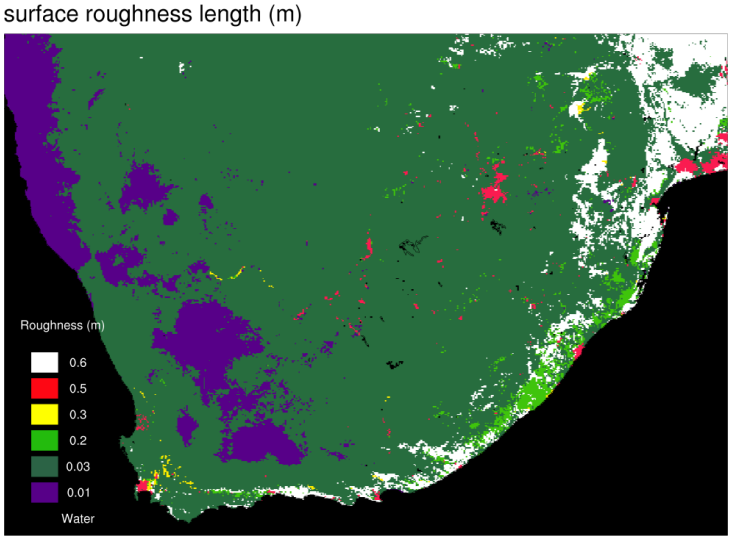

Figure 3.4 – Map of surface roughness length (m) for WASA2 WRF domain based on the ESA/CCI land cover map and Table 3.3

.

3.4 Data processing

Wind speeds and directions are derived from the WRF model output, which represents 30-minutes instantaneous values. For evaluating the model wind speed climatology, the zonal and meridional wind components on their original staggered Arakawa-C grid were interpolated to the coordinates of the mass grid. The interpolated wind components were then used to compute the wind speed and rotated to the true north to derive the wind direction. For a given height, e.g., 100 m, wind speeds are interpolated between neighbouring model levels using linear interpolation in logarithmic height. It was found that this interpolation procedure preserves more of the original features in the model wind profile compared to other schemes (e.g., linear or polynomial interpolation of the wind components).

Chapter 4

Wind atlas validation

4.1 Correlation analysis

In this section the correlation coefficients between the observed wind measurements at the mast and the WRF model simulation are computed for the overlap periods of data. The results are then illustrated in the correlation matrix, Table 4.1.

For each mast (sites 1–15, 1st column of Table 4.1) the number of wind measurements available in both observed data and WRF model simulations are counted and showed in the second column of the Table 4.1. The correlation coefficients are computed on the data based on the half-hour wind speed, hourly mean wind speed and monthly mean wind speed.

Table 4.1 – Correlation coefficient (ρ) of the wind speed at 62 m AGL: number of the site, number of measurements available, correlation based on 30 minutes, hourly, and monthly averaged wind speed.

Site	Num. values	ρ 30'	ρ hourly	ρ monthly
1	131100	0.763	0.776	0.892
2	128044	0.668	0.687	0.672
3	131849	0.747	0.761	0.902
4	53483	0.740	0.756	0.947
5	122832	0.817	0.828	0.772
6	127604	0.774	0.792	0.962
7	131559	0.709	0.727	0.710
8	122946	0.730	0.746	0.817
9	111651	0.705	0.720	0.889
10	121735	0.616	0.637	0.868
11	35804	0.777	0.792	0.971
12	37800	0.597	0.621	0.794
13	38721	0.686	0.709	0.815
14	38405	0.688	0.711	0.966
15	35777	0.614	0.642	0.953

4.2 Comparison of observed and simulated wind climatologies

The wind measurements obtained by the wind mast, erected at each site, are compared to the wind data provided by the WRF simulations. During the first phase of WASA (WASA1), the WRF-simulated data compared well against the mast-derived wind climatologies (see WASA1 final report). As the WASA2 simulations use an updated WRF mesoscale modelling framework (see section Chapter 3), we update the validation at masts WM01-10 in addition to the validation of the new masts (WM11-15). If there are significant differences between the WASA1 and WASA2 WRF-simulated wind climatologies these are mentioned in the text. If there is no mention of differences between the WASA1 and WASA2 results this indicates WRF-simulated wind climatologies were similar between WASA1 and WASA2.

The data available for the validation cover a period of about 8 years for most of the sites, except for the WM04 where only three years were available, and for the sites 11–15 where there were only two years and half of data coincide with the WRF model simulation.

All the results are illustrated in the Figures 4.1–4.2.15. The wind speed used to validate the WRF simulation is the wind speed measured at 62 m AGL. For all the masts a diurnal and annual cycle analysis of the wind speed is realised and the following assessments are made:

- Histogram of wind speed (all sectors)
- Seasonal cycle
- Diurnal cycle
- Annual speed cycle
- Wind rose of the wind distribution
- Monthly speed cycle per year (if more than 5 years of data are available)

The comparison of the wind speed distribution is illustrated in the histogram, while the mean seasonal and the mean diurnal cycle are also showed as comparison between the observed values and the WRF simulations and are given in a normalised wind speed (top panel). The average wind speed of each hour of the 24-hour day is computed for each months of the period available and the results are showed in a colormap (top colormap) in which the diurnal cycle at a monthly scale can be compared using the colorbar in $0 - 12ms^{-1}$ located below the colormap.
For the sites where the data available cover a reasonable time period, more than 5 years of wind data, the following assessment is also realised: This is illustrated in the bottom colormap, where the average wind speed of each month of the year are computed for each year of the measurements and this allows to compare average monthly variation against the years of measurements. Again, the colorbar is located below the bottom colomap and it is in 3–10 $\mathrm{m\,s^{-1}}$.

Finally, for all the sites a comparison of the wind measurements, from the observations and the WRF simulations is done for all the height available (10m, 20m, 40m, and 62m) and the following evaluation are realised:

- Height comparison

- Height correlation
- Height variance

The height comparison is given by the mean wind speed computed at each height of both the observed data and the WRF simulations and the results are plot together showing the wind profile for the listed height, then a correlation between the wind measurements available at each height is carried out and again illustrated along all the height. While the last figure shows the ration of the variance between the WRF model and the observed data (bottom panel). The last three validation metrics were not available during the WASA1 validation.

4.2.1 Alexander Bay (WM01)

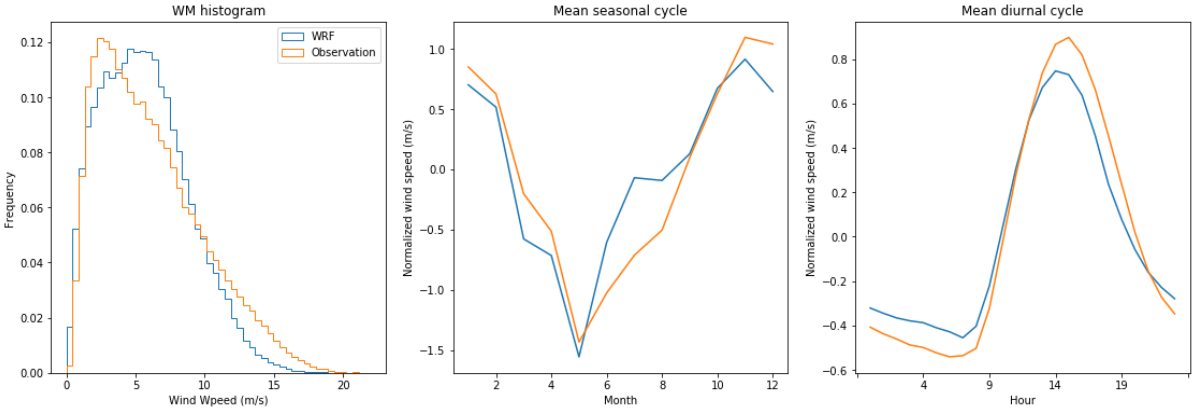

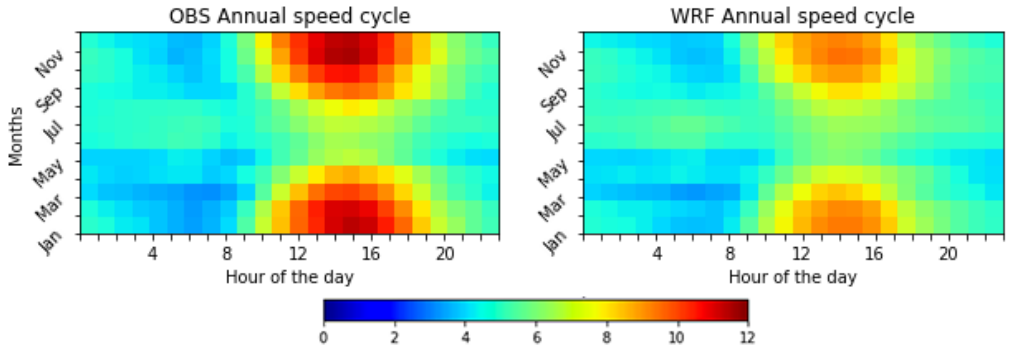

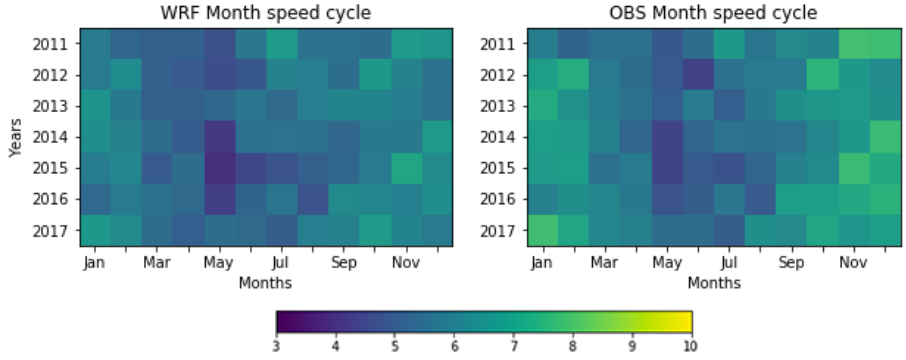

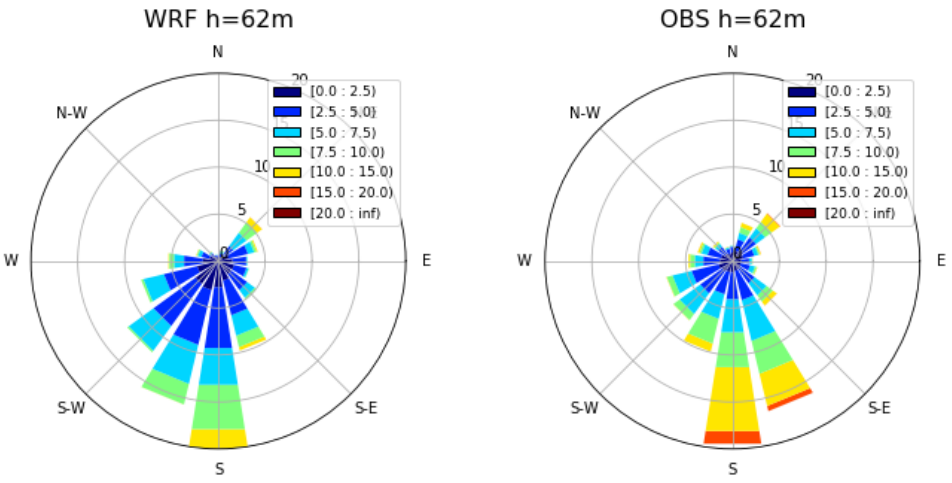

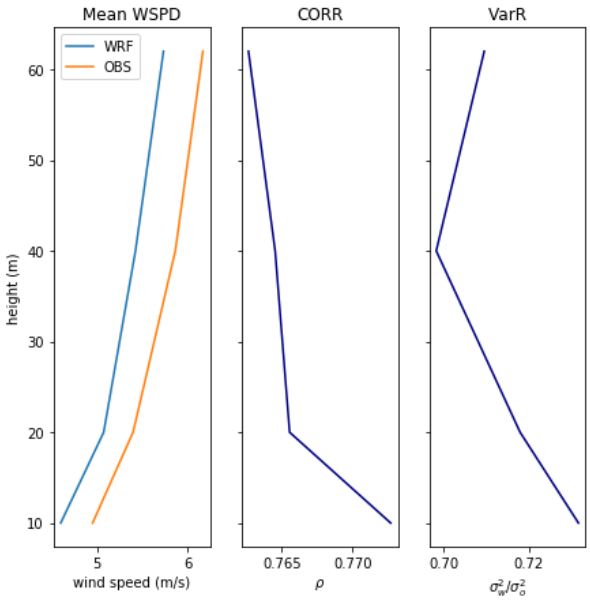

Figure 4.1 – Comparison of wind speed ($\mathrm{m\,s^{-1}}$) for observed measurements (orange) versus WRF model simulations (blue) at 62m AGL at WM01: wind speed distribution (top left), mean seasonal cycle (top center), mean diurnal cycle (top right). Annual speed cycle: mean wind speed (ms^{-1}) at 62m AGL as a function of time of the day (x-axis) and month of the year (y-axis), (top colormap) for the observed measurements (left) and WRF simulations (right). Monthly wind speed cycle: mean wind speed ($\mathrm{m\,s^{-1}}$) at 62m AGL as a function of months (x-axis) and years (y-axis), (bottom colormap) for the observed measurements (left) and WRF simulations (right). Wind rose of wind direction frequency distribution (ms^{-1}) at 62m AGL for observed measurements (left) and WRF simulations (right). Comparison of mean wind speed ($\mathrm{m\,s^{-1}}$) for all the height, observed (orange) and WRF (blue), (bottom left), correlation (bottom centre), ratio of variance (bottom right).

At this mast the histogram shows that model slightly underestimates the frequency of wind speeds between 2–4 $\mathrm{m\,s^{-1}}$ with a corresponding slight overestimation if wind speeds in the 5–7 $\mathrm{m\,s^{-1}}$ range. The WRF model captures the shape of the mean seasonal cycle very well with only a small over-simulation (under-simulation) of wind speeds in June and July (August to December). The model also captures the shape of the diurnal cycle of wind speed extremely well, however it under-simulates the high wind speeds in the late afternoon during summer. In WASA1 there was a phase error in the peak of the maximum wind speed which in the observations was 16:00 but in the WRF model was 18:00; in the current simulations this phase error is corrected, and the model simulates maximum daily wind speeds at the same time as observations. The wind rose shows that the WRF simulations successfully reproduce the generally southerly wind component. However, the model does not capture the highest wind speeds and also over-simulates winds from the south west and under-simulates winds from the south-east. In the vertical structure the slight under-simulation of wind speeds is also evident. The correlation between modelled and observed wind speeds at each measuring point on the mast is highest at 10 m and becomes smaller with height, however, these correlations are still good ($0.760 < \mathrm{CORR} < 0.775$). The WRF model over simulates wind speed variance if the ratio of variance between the WRF model and the observed data is greater than 1 and under-simulates variance when this ratio is between 0–1. At this mast lower wind speed variance is simulated by the model compared to the observed wind speed variance.

4.2.2 Clavinia (WM02)

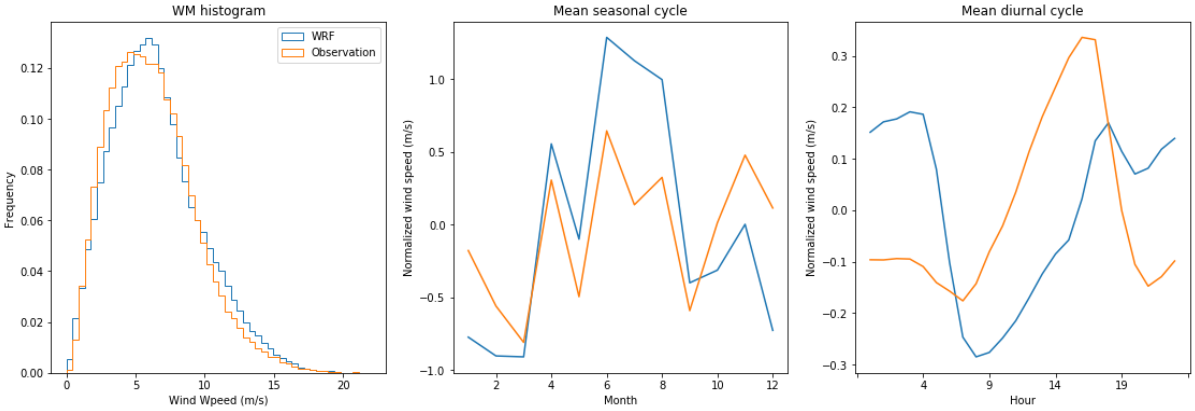

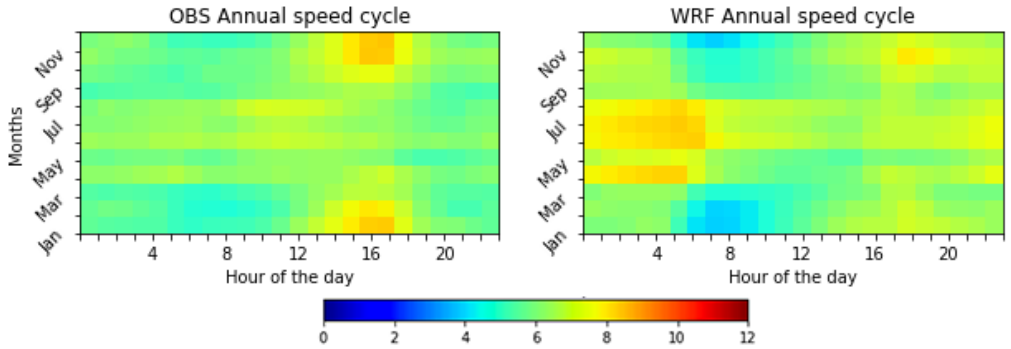

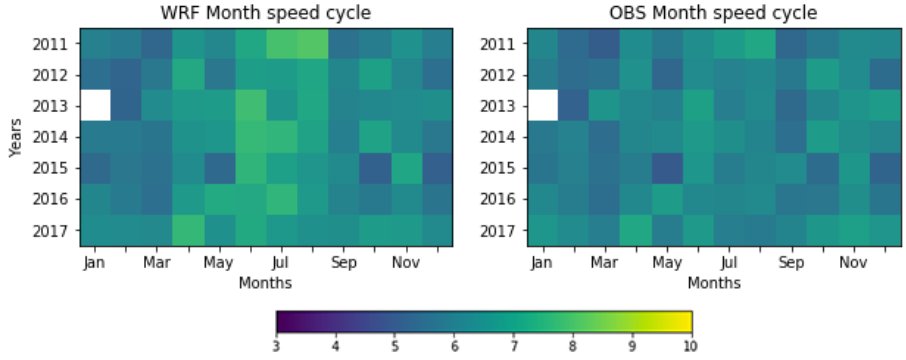

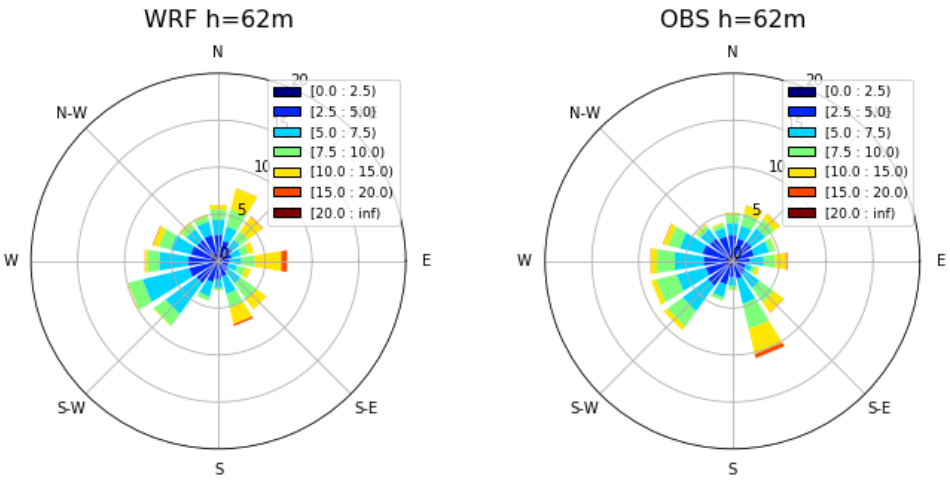

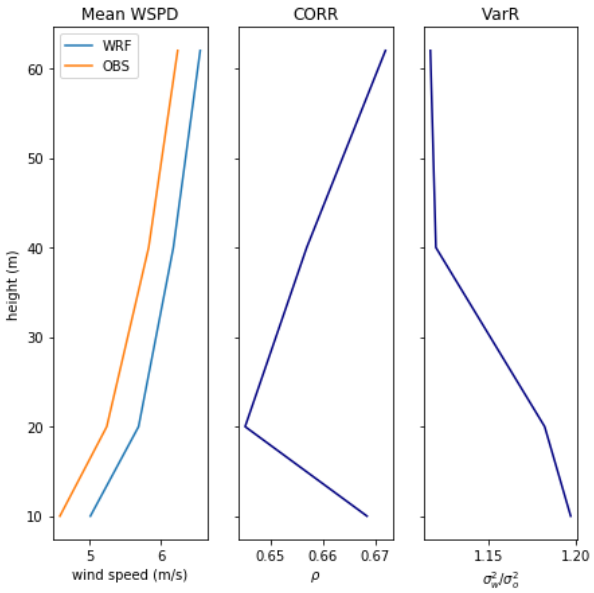

Figure 4.2 – As of 4.1 but for WM02.

At WM02 (Fig.4.2), the histogram shows that model slightly over-simulates the frequency of high wind speeds. The WRF model captures the general shape of the mean seasonal cycle however, it over simulates winter wind speeds and under simulates summer wind speeds. The diurnal cycle of wind speed is not captured by the model and the WASA1 results were actually more accurate. The wind rose shows that the WRF simulations generally reproduces the directional frequency distribution but there is an over-simulation of winds from the north and east. In the vertical structure the over-simulation of wind speeds is also evident. The correlation between modelled and observed wind speeds at each measuring point are lower than at WM01 and are highest at 10 m and 62 m ($0.64 < \text{CORR} < 0.67$). At this mast higher wind speed variance is simulated by the model compared to the observed wind speed variance.

4.2.3 Vredendal (WM03)

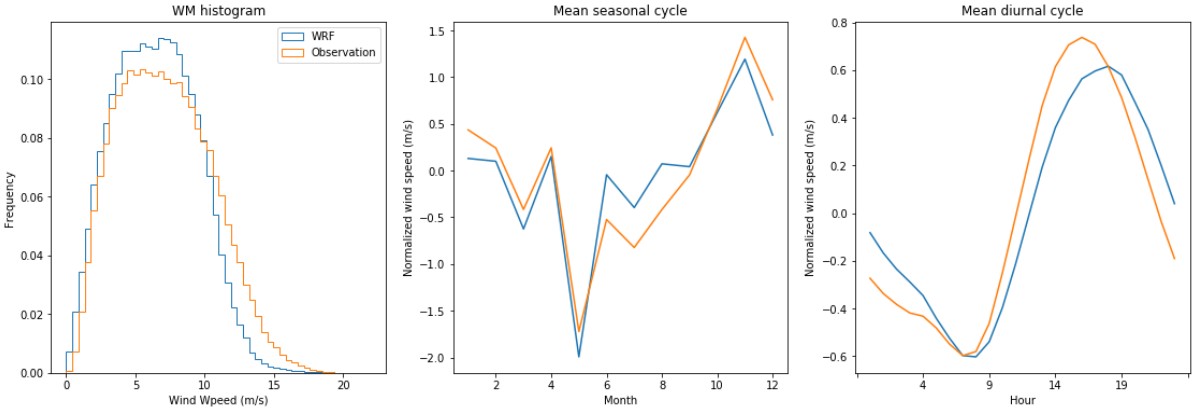

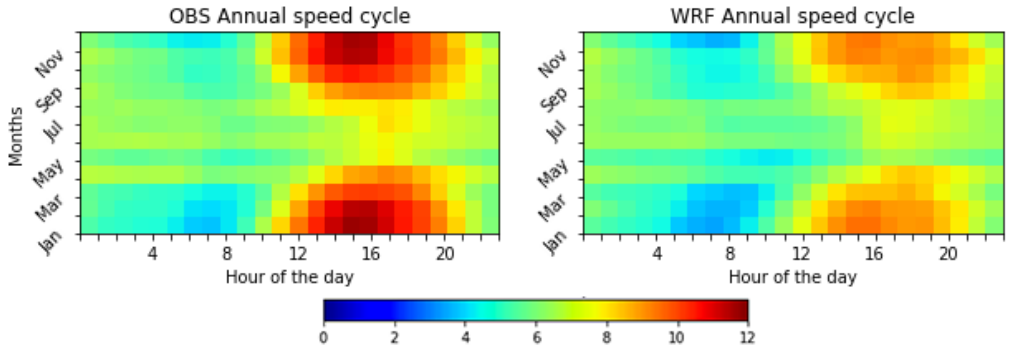

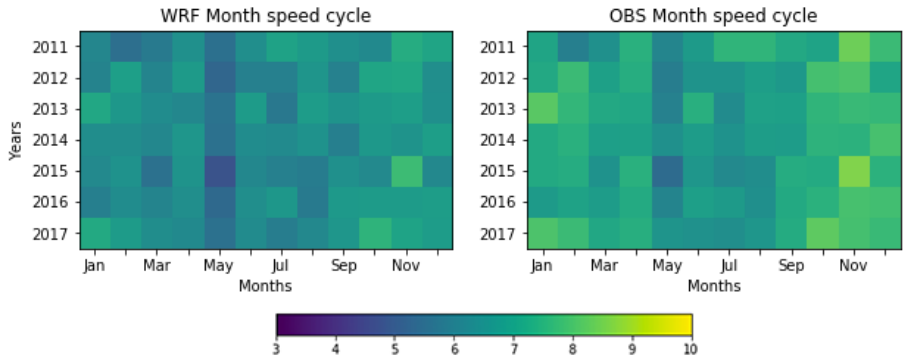

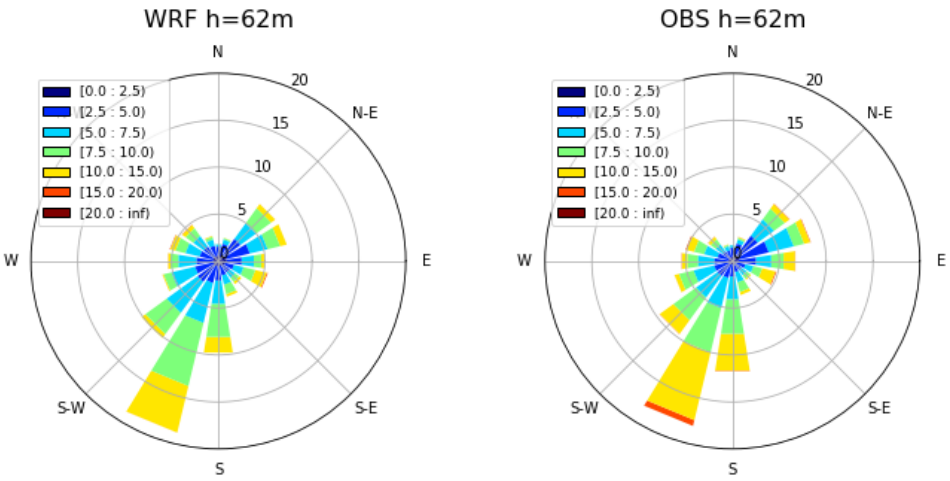

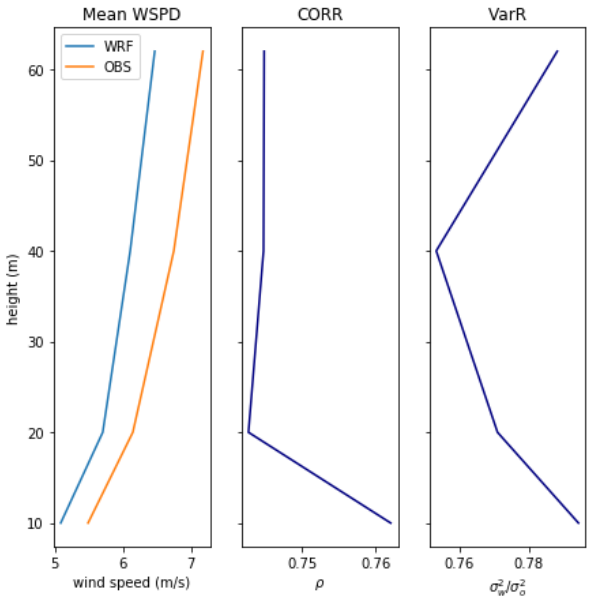

Figure 4.3 – As of 4.1 but for WM03.

At WM03 (Fig.4.3), the histogram shows that model slightly over-estimates the frequency of mean wind speeds but under-simulates the frequency of high wind speeds. The WRF model captures the shape of the mean seasonal cycle very well with only a small over-simulation of winter wind speeds in June-August. The model also captures the shape of the diurnal cycle of wind speed; however it under-simulates the high wind speeds in the late afternoon during summer and there is a slight phase error introduced compared to the WASA1 simulations that simulates peak wind speeds 1–2 hours later than observed. The wind rose shows that the WRF simulations reproduce the directional frequency distribution very well. In the vertical structure the slight under-simulation of wind speeds is also evident. The correlation between modelled and observed wind speeds at each measuring point on the mast is highest at 10 m and becomes smaller with height, however, these correlations are still good ($0.74 < \text{CORR} < 0.76$). At this mast lower wind speed variance is simulated by the model compared to the observed wind speed variance.

4.2.4 Vredenburg (WM04)

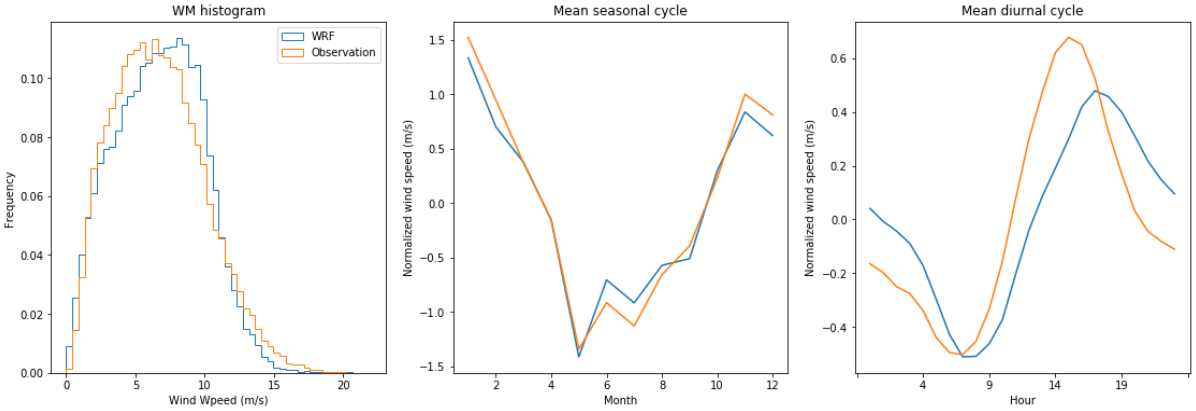

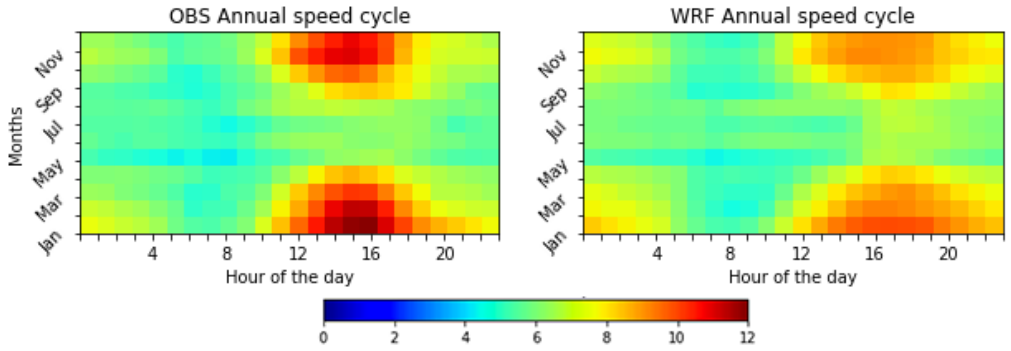

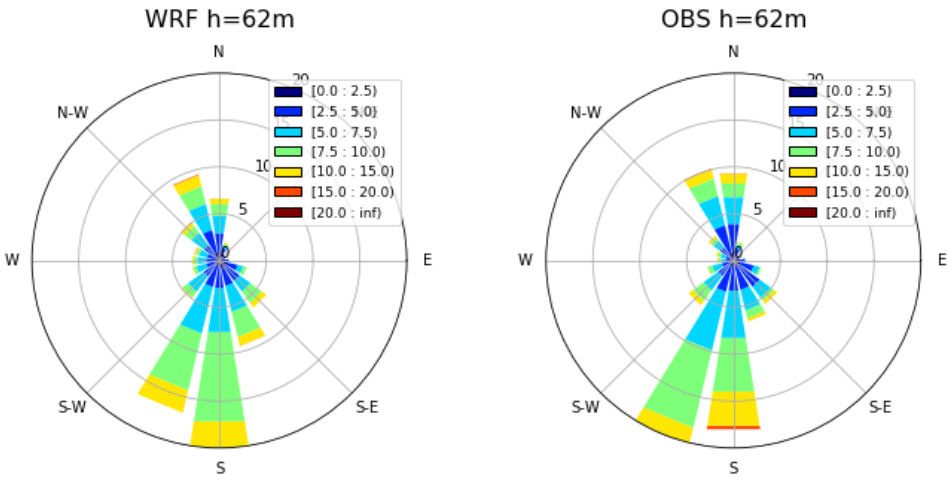

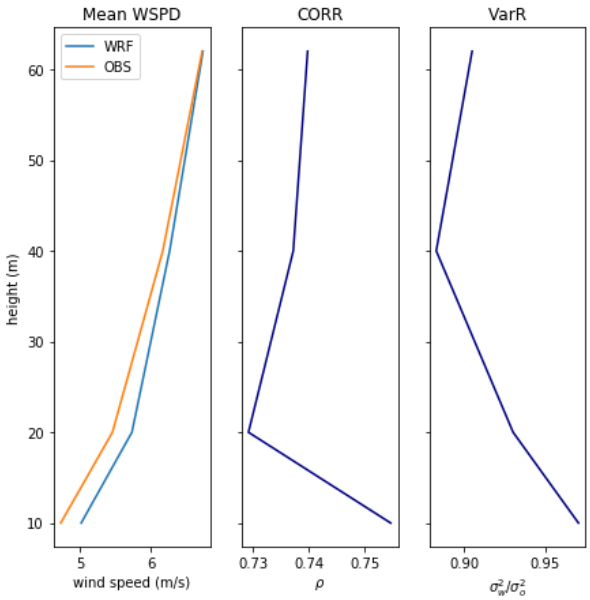

Figure 4.4 – As of 4.1 but for WM04.

At WM04 (Fig.4.4), the histogram shows that the model over-simulates the frequency of wind speeds between 6–10 $\mathrm{m\,s^{-1}}$ but under-simulates wind speeds higher than 10 $\mathrm{m\,s^{-1}}$. The WRF model captures the shape of the mean seasonal cycle very well. The model also captures the shape of the diurnal cycle of wind speed; however, it over-simulates night-time wind speeds and under-simulates day-time wind speeds; there is also a slight phase error introduced compared to the WASA1 simulations that simulates peak wind speeds 1-2 hours later than observed. The wind rose shows that the WRF simulations reproduce the directional frequency distribution well, although the model has a maximum frequency in the south west sector whereas this is in the south sector in the observations. In the vertical structure there is a slight under-simulation of wind speeds at the lower levels but at the 62-meter level there is no difference in the mean. The correlation between modelled and observed wind speeds at each measuring point on the mast is highest at 10 m and becomes smaller with height, however, these correlations are still good ($0.73 < \mathrm{CORR} < 0.75$). At this mast the WRF model slightly under-simulates wind speed variance, however, the ratio values are very close to 1, indicating similar variance between the model and observed. It should be noted that this mast was sabotaged and only 3 years of data are available.

4.2.5 Napier (WM05)

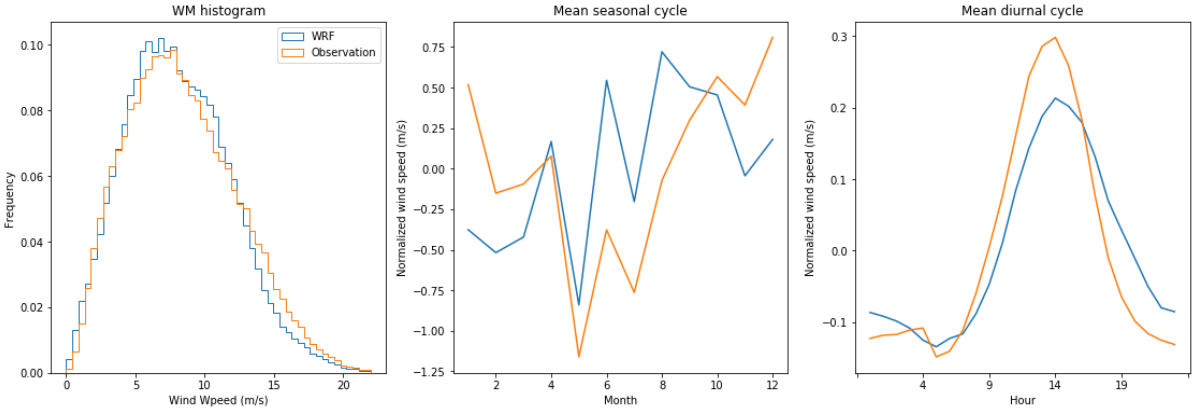

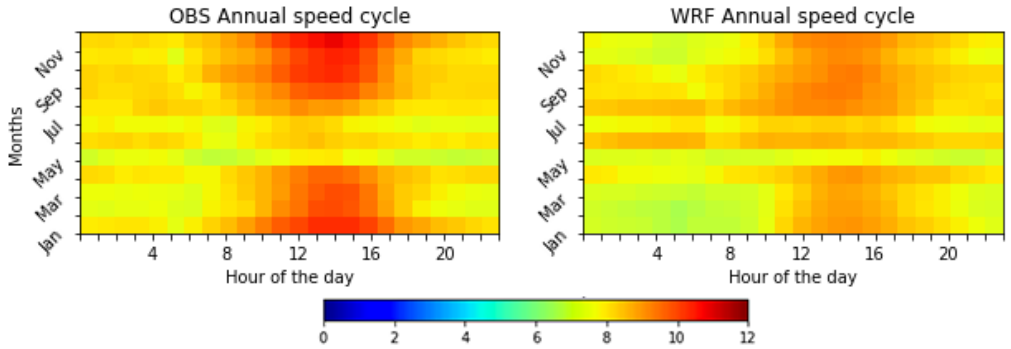

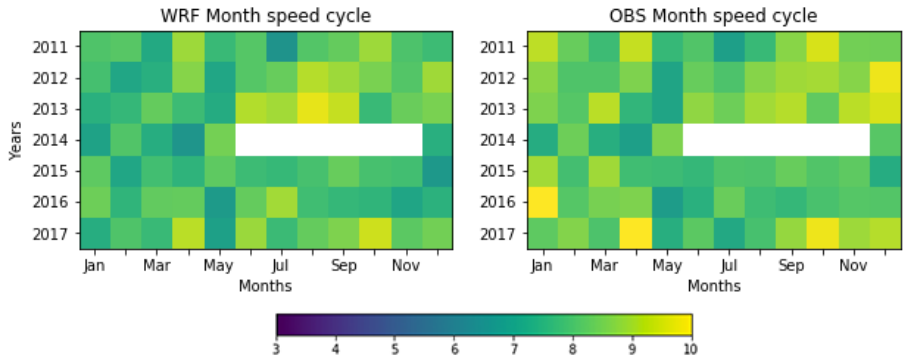

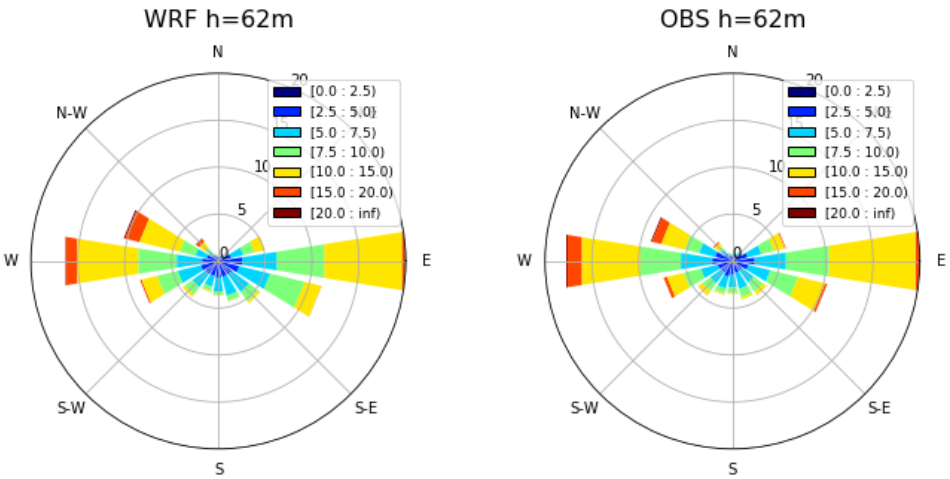

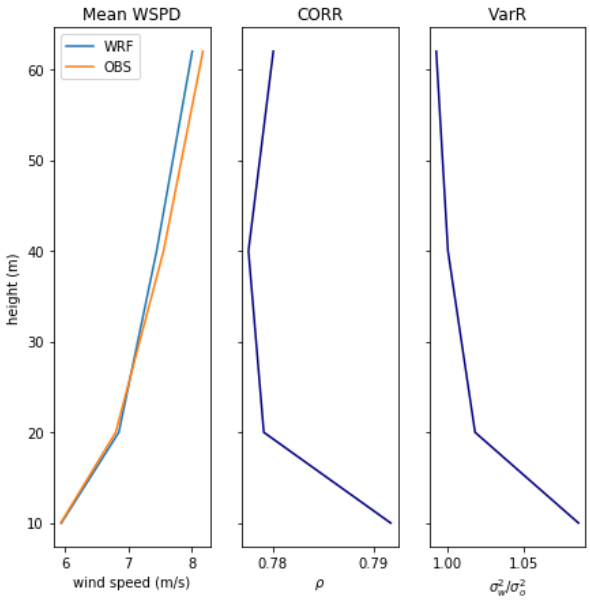

Figure 4.5 – As of 4.1 but for WM05.

At WM05 (Fig.4.5), the wind speed histogram is very well reproduced by the model although there is a small over-simulation of frequency of wind speeds between 5–7 m s^{-1} and an under-simulation of wind speeds higher than about 13 m s^{-1}. The WRF model captures the shape of the mean seasonal cycle but not the magnitude as it over-simulates winter wind speeds and under-simulates simmer wind speeds; the seasonal cycle of wind speed was captured more accurately in the WASA1 simulations. The model captures the shape of the diurnal cycle of wind speed well, however it over-simulates evening wind speeds and under-simulates daytime wind speeds including peak afternoon wind speeds. The wind rose shows that the WRF simulations reproduce the directional frequency distribution well with dominant easterly and westerlies. In the vertical structure there is good simulation of the wind speeds with good correlations between modelled and observed wind speeds (CORR = 0.79). At this mast the wind speed variance ratio values are very close to 1, indicating similar variance between the model and observed at each height.

4.2.6 Sutherland (WM06)

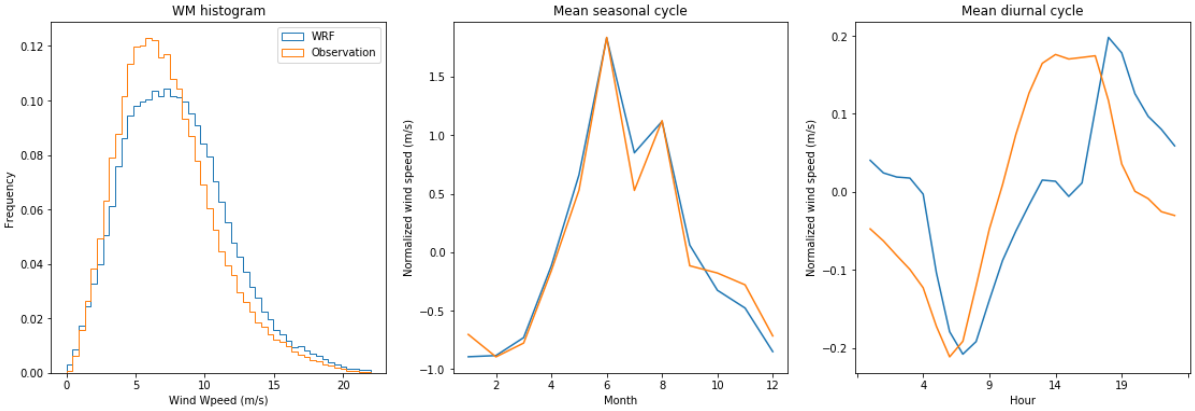

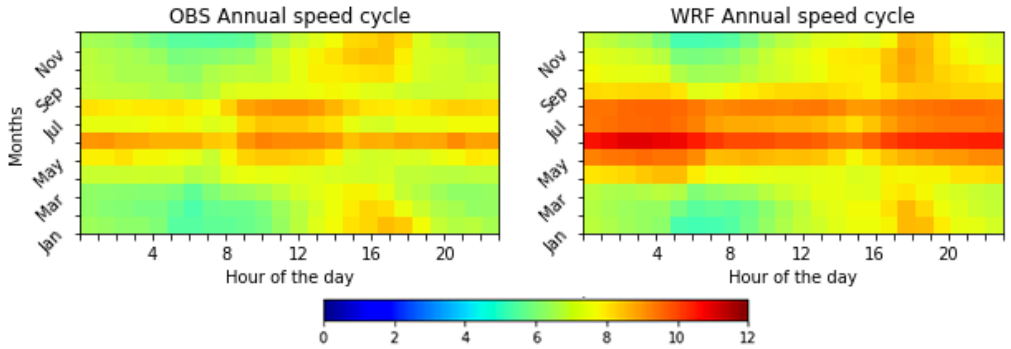

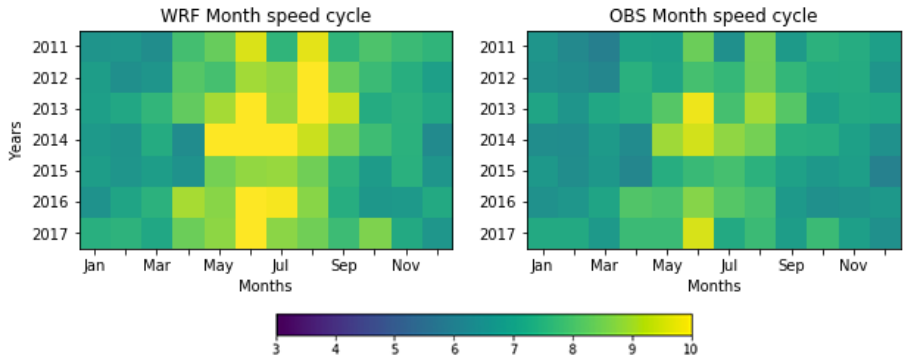

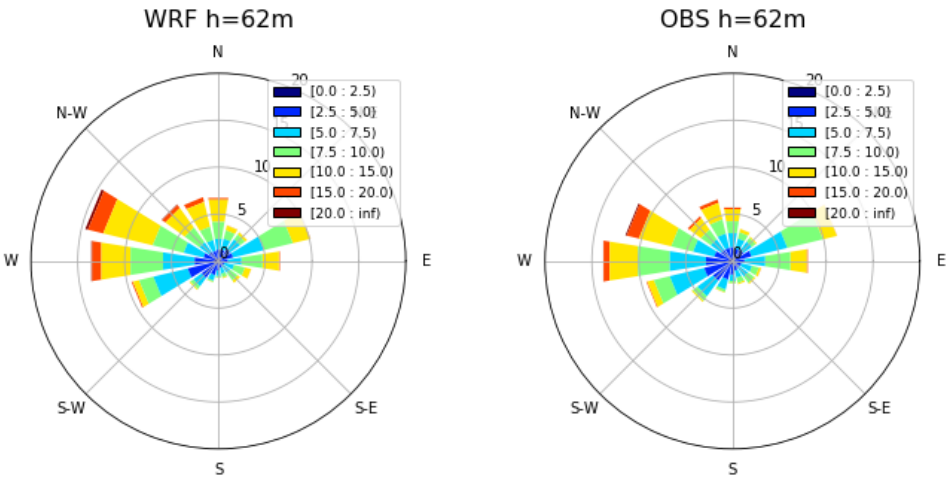

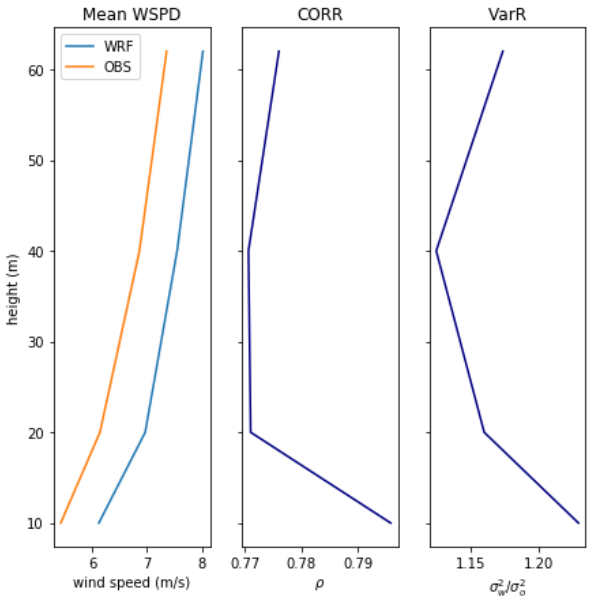

Figure 4.6 – As of 4.1 but for WM06.

At WM06 (Fig.4.6), the histogram shows that the model under-simulates the frequency of wind speeds between 5–8 $\mathrm{m\,s^{-1}}$ but over-simulates wind speeds higher than about 10 $\mathrm{m\,s^{-1}}$. The WRF model captures the shape of the mean seasonal cycle well and improves on the WASA1 results, although it slightly over-simulates winter wind speeds. The model captures the general shape of the diurnal cycle of wind speed, however it is out of phase with observations by between 1–3 hours, over-simulates night-time wind speeds and under-simulates day-time wind speeds including peak afternoon wind speeds; the diurnal cycle of wind speed was captured more accurately in the WASA1 simulations. The wind rose shows that the WRF simulations reproduce the directional frequency distribution well with dominant westerlies. In the vertical structure there the model wind speeds are generally higher by almost 1 $\mathrm{m\,s^{-1}}$ and the best correlation is at the 10-meter level ($0.77 < \mathrm{CORR} < 0.80$). At this mast higher wind speed variance is simulated by the model compared to the observed wind speed variance.

4.2.7 Beaufort West (WM07)

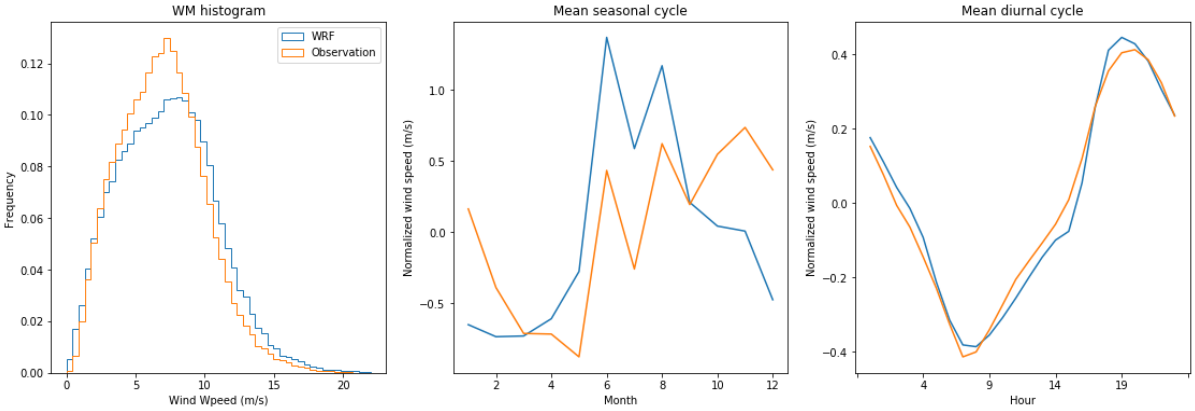

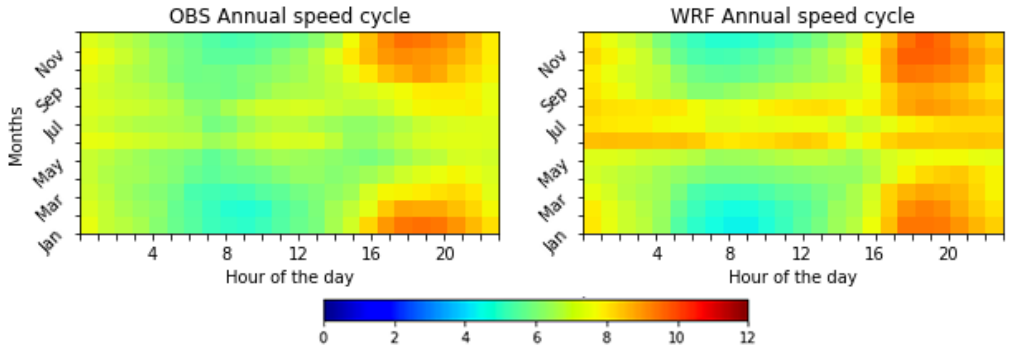

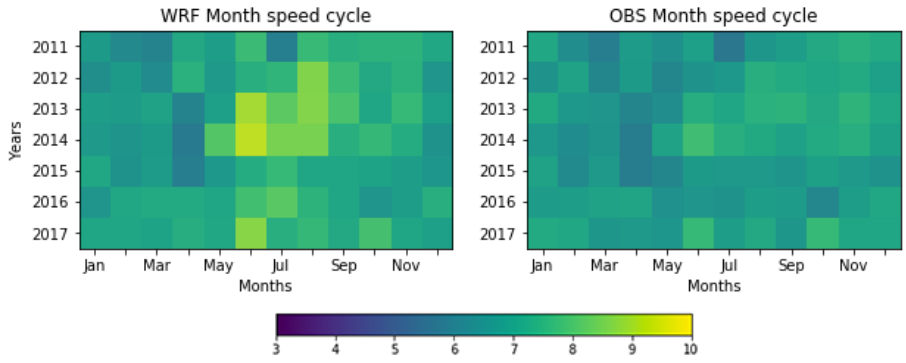

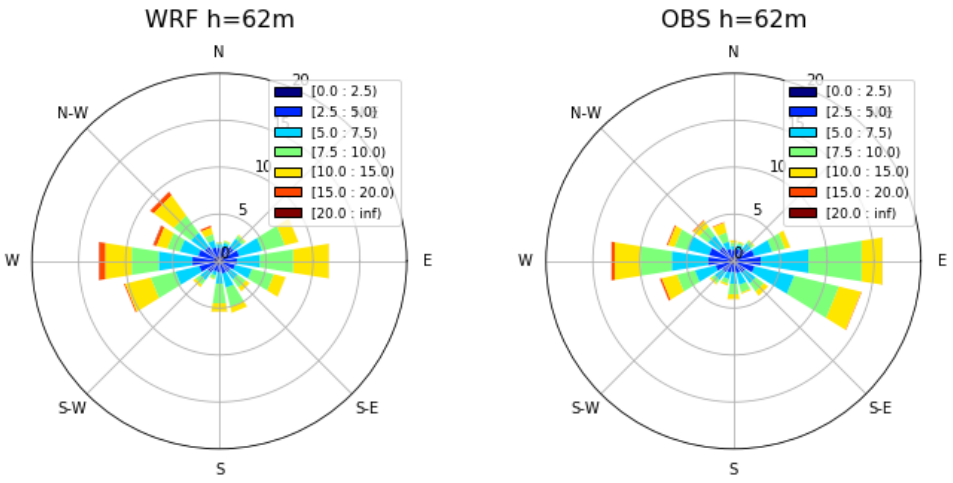

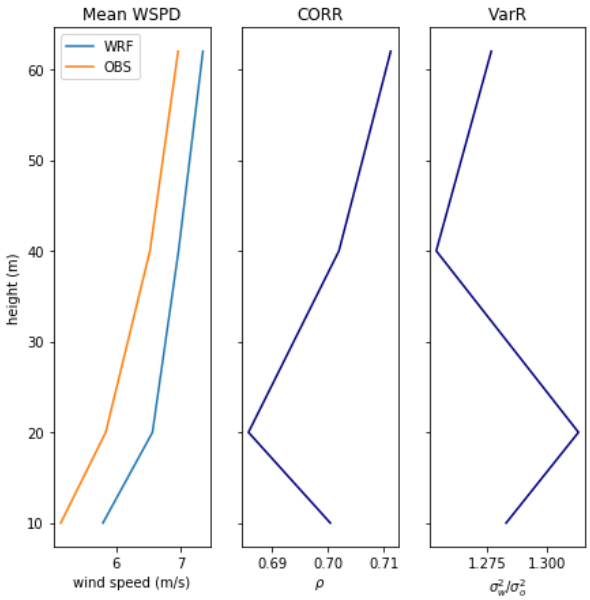

Figure 4.7 – As of 4.1 but for WM07.

At WM07 (Fig.4.7), the histogram of wind speeds shows that the model under-simulates the frequency of wind speeds between 5–9 $\mathrm{m\,s^{-1}}$ but over-simulates wind speeds higher than about 10 $\mathrm{m\,s^{-1}}$. The WRF model does not capture the shape of the mean seasonal cycle well, as was the case in the WASA1 simulations, as it over-simulates autumn and winter wind speeds and under-simulates spring and summer wind speeds. The model captures the shape of the diurnal cycle of wind speed very well. The wind rose shows that the WRF simulations produce too few easterly and south easterly winds and too many north westerly events. In the vertical structure there the model wind speeds are higher by typically 0.5 $\mathrm{m\,s^{-1}}$ and the best correlation is at the 62-meter level, although correlations are relatively low ($0.69 < \mathrm{CORR} < 0.71$). At this mast higher wind speed variance is simulated by the model compared to the observed wind speed variance.

4.2.8 Humansdorp (WM08)

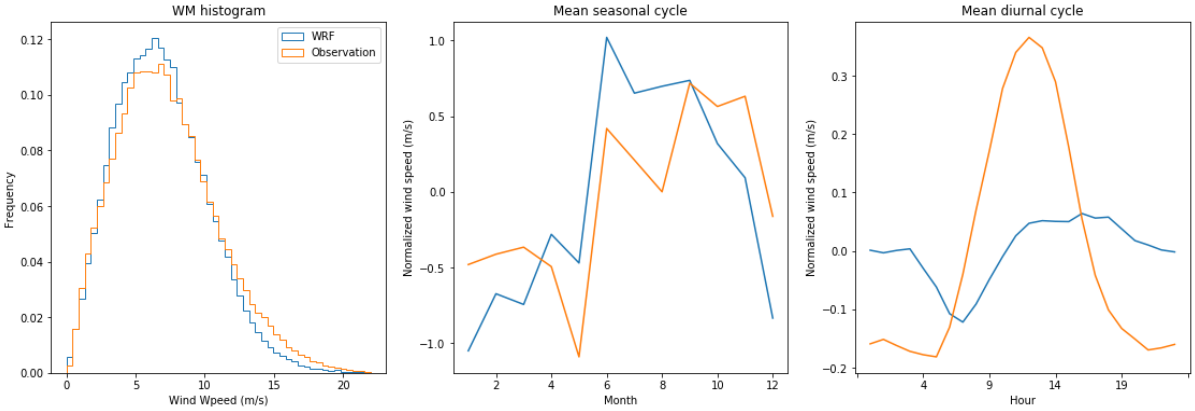

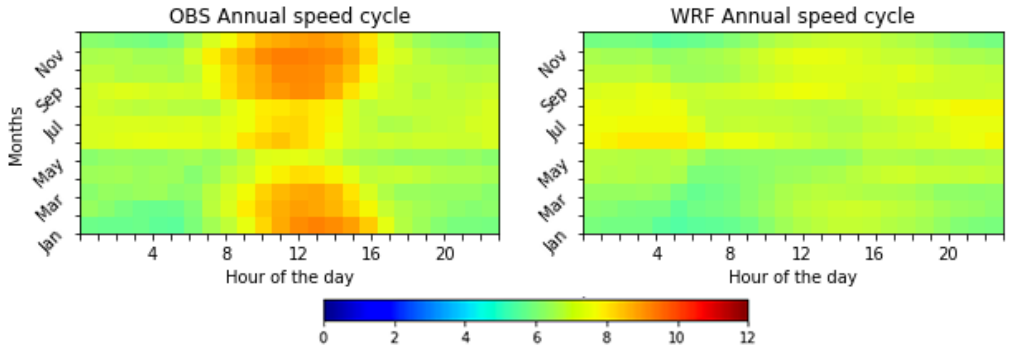

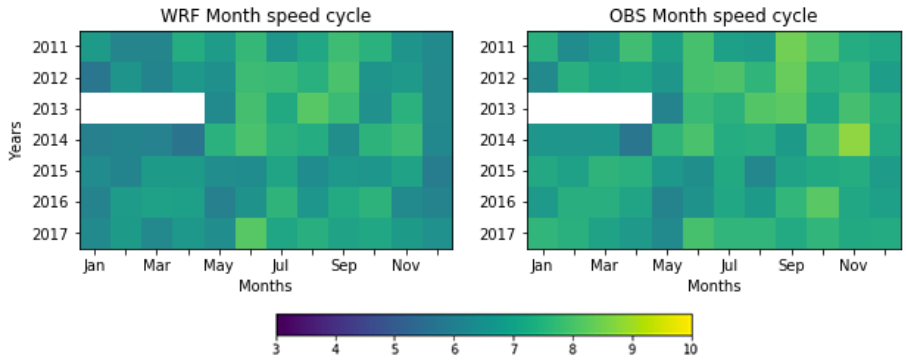

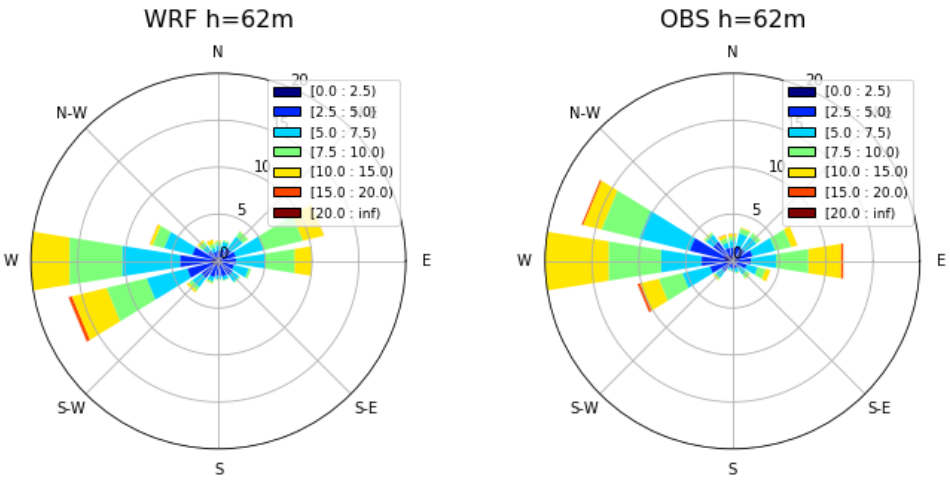

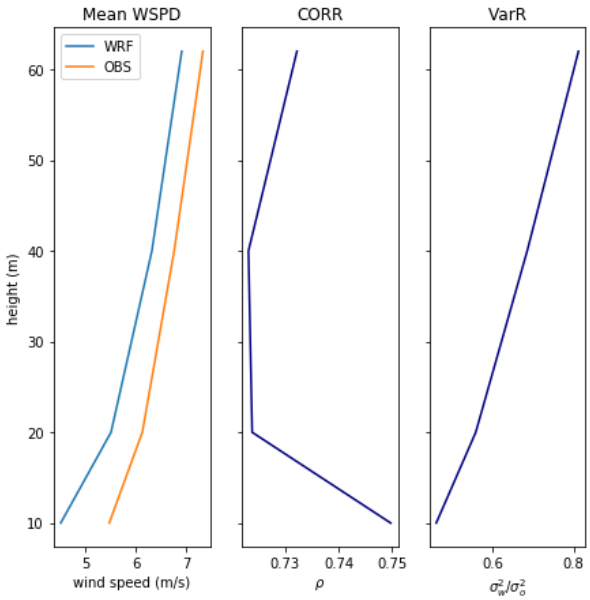

Figure 4.8 – As of 4.1 but for WM08.

At WM08 (Fig.4.8), the histogram of wind speeds shows that the model over-simulates the frequency of wind speeds between 5-9 $\mathrm{m\,s^{-1}}$ but under-simulates wind speeds higher than about 10 $\mathrm{m\,s^{-1}}$. The WRF model does not capture the shape of the mean seasonal cycle well and it over-simulates autumn and winter wind speeds and under-simulates spring and summer wind speeds. The model does not capture the shape nor magnitude of the diurnal cycle of wind speed and the diurnal cycle results were captured more accurately in the WASA1 simulations. The wind rose shows that the WRF simulations produce too few north westerly and too many south easterly winds. In the vertical structure there the model wind speeds are lower by typically 0.5 $\mathrm{m\,s^{-1}}$ and the best correlation is at the 10-meter level, ($0.725 < \mathrm{CORR} < 0.75$). At this mast lower wind speed variance is simulated by the model compared to the observed wind speed variance.

4.2.9 Noupoort (WM09)

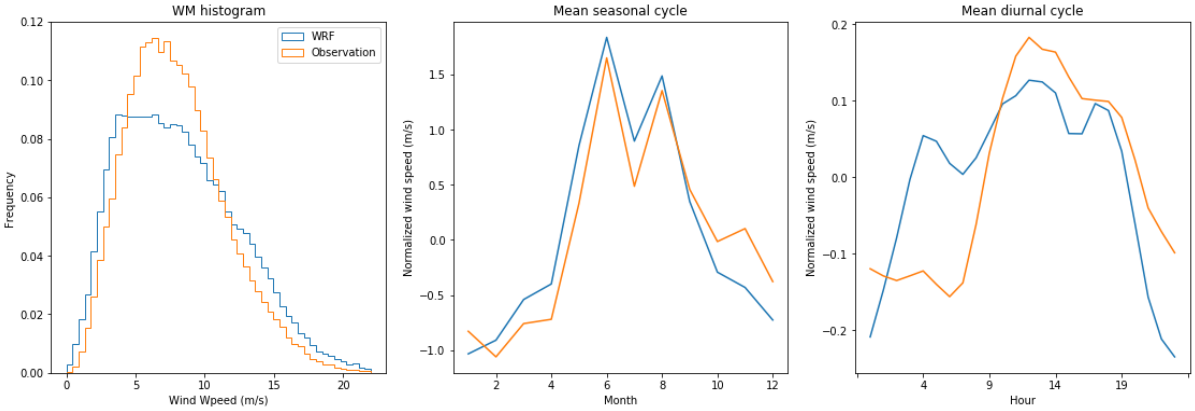

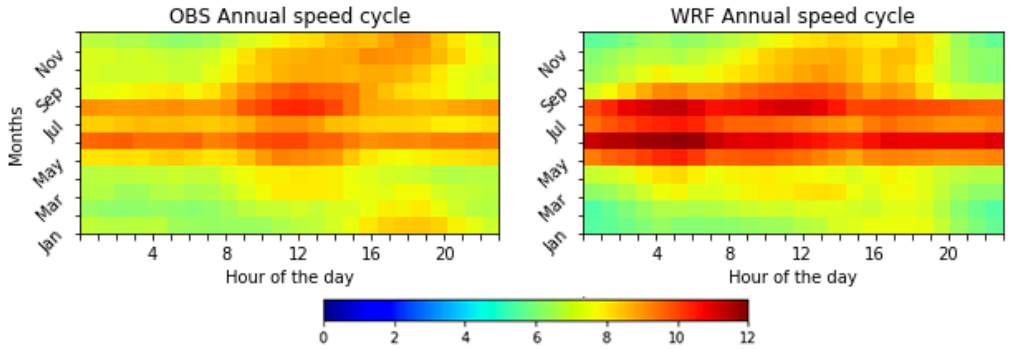

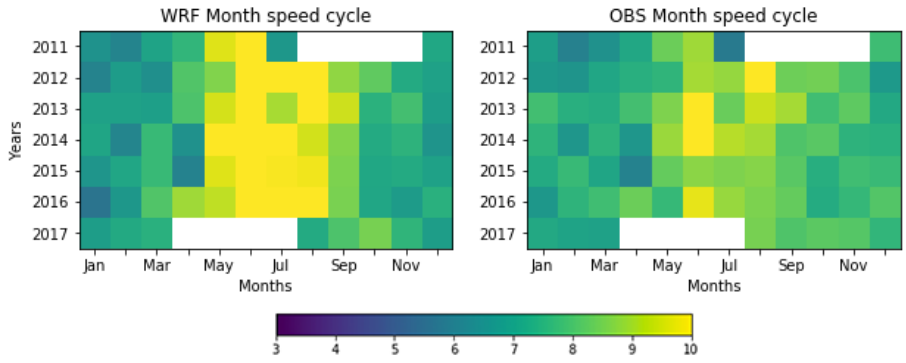

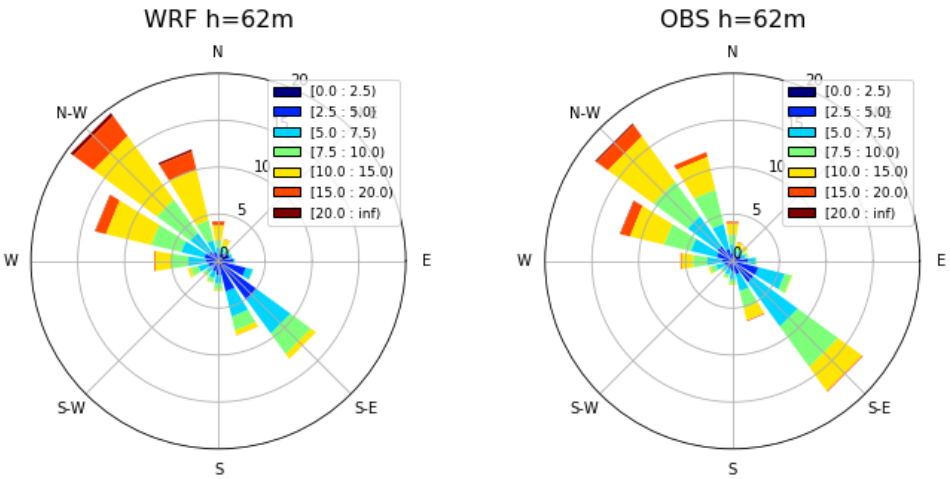

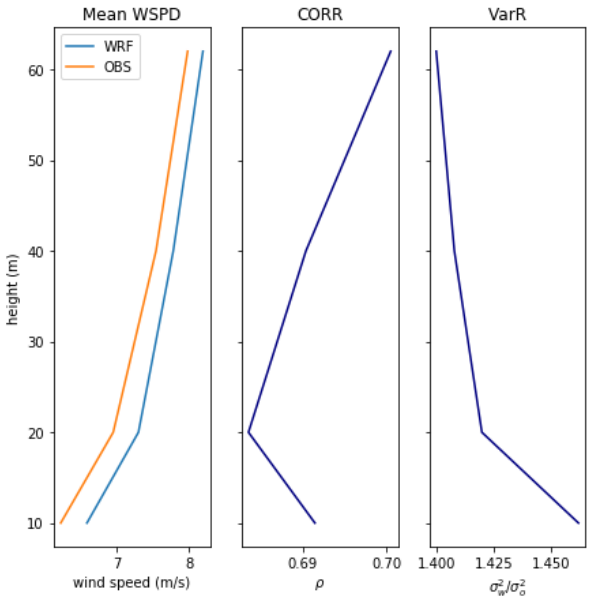

Figure 4.9 – As of 4.1 but for WM09.

At WM09 (Fig.4.9), the histogram of wind speeds shows that the model under-simulates the frequency of wind speeds between 4–10 $\mathrm{m\,s^{-1}}$ but over-simulates wind speeds higher than about 12 $\mathrm{m\,s^{-1}}$. The WRF model captures the shape of the mean seasonal cycle but it over-simulates wind speeds from mid-summer through winter into the following spring. The model does not capture the shape of the diurnal cycle of the morning when it simulates wind speeds that are too high, however the afternoon wind speeds, although too low, are well simulated and improve on the WASA1 afternoon wind simulations which were out of phase. The wind rose shows that the WRF simulations reproduce the directional frequency distribution well. In the vertical structure there the model wind speeds are similar, and the best correlation is at the 62-meter level, ($0.68 < \mathrm{CORR} < 0.70$). At this mast higher wind speed variance is simulated by the model compared to the observed wind speed variance.

4.2.10 Butterworth (WM10)

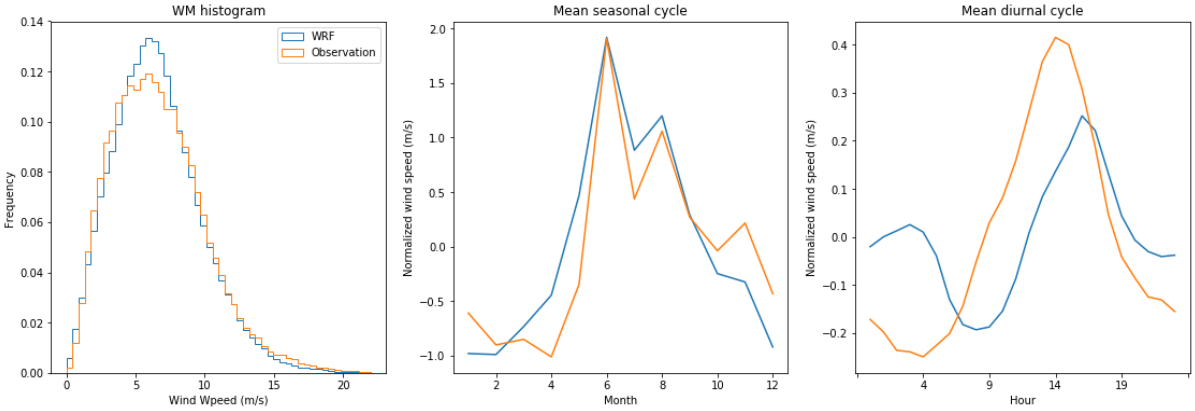

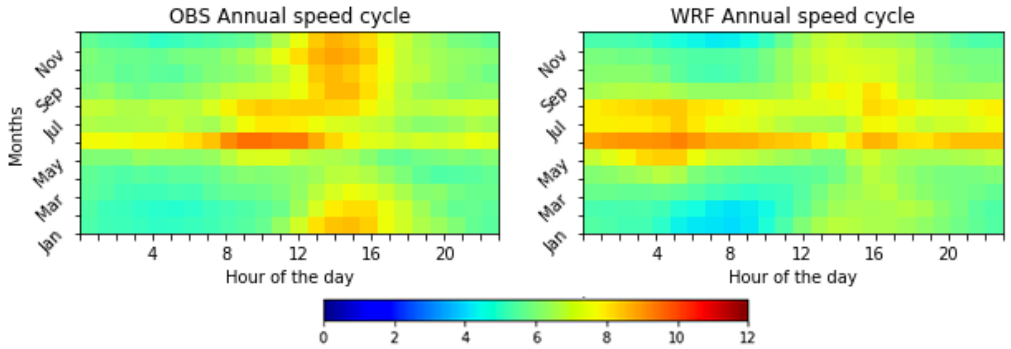

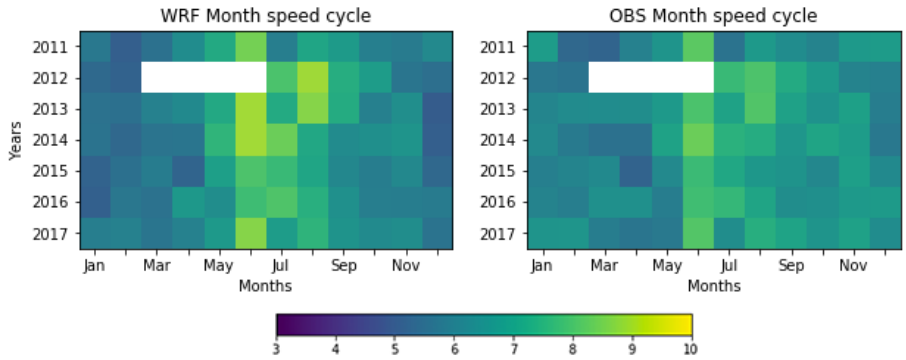

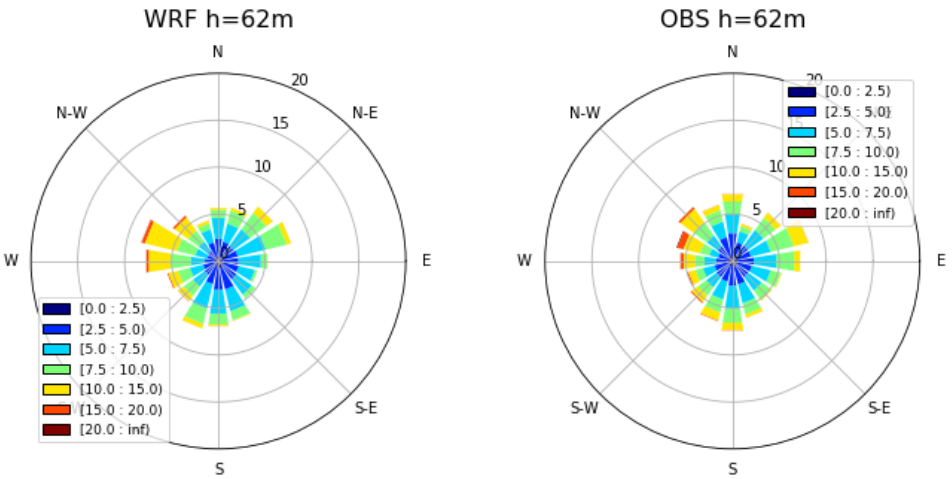

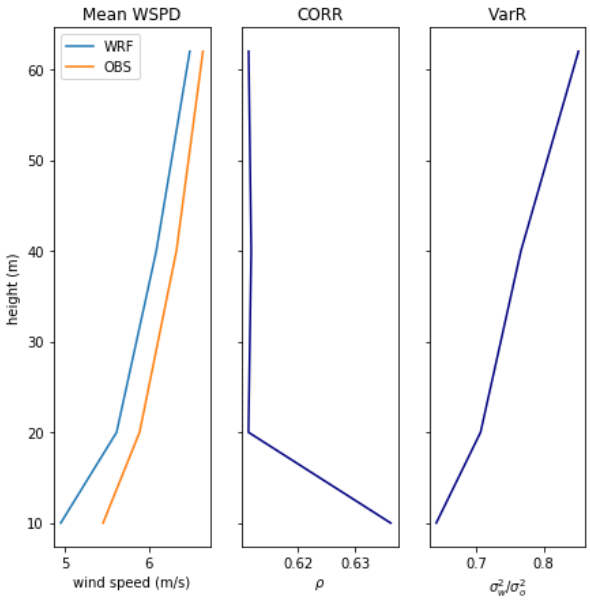

Figure 4.10 – As of 4.1 but for WM10.

At WM10 (Fig.4.10), the histogram of wind speeds shows that the model over-simulates the frequency of wind speeds between 5–10 $\mathrm{m\,s^{-1}}$ but captures the frequency of other wind speeds well. The WRF model captures the shape of the seasonal cycle but it over-simulates wind speeds in autumn mid-winter and under-simulates wind speeds in late spring and mid-summer. In the diurnal cycle the model simulates night time wind speeds that are too high and day time wind speeds that are too low. The wind rose shows that the WRF simulations reproduce the multi-sectoral directional frequency distribution adequately although too few winds in the northerly and north westerly sector are simulated and too many in the westerly and west-north-west sector. In the vertical structure there the model wind speeds are similar, but correlations are generally lower than at other masts ($0.61 < \mathrm{CORR} < 0.64$). At this mast lower wind speed variance is simulated by the model compared to the observed wind speed variance.

4.2.11 Rhodes (WM11)

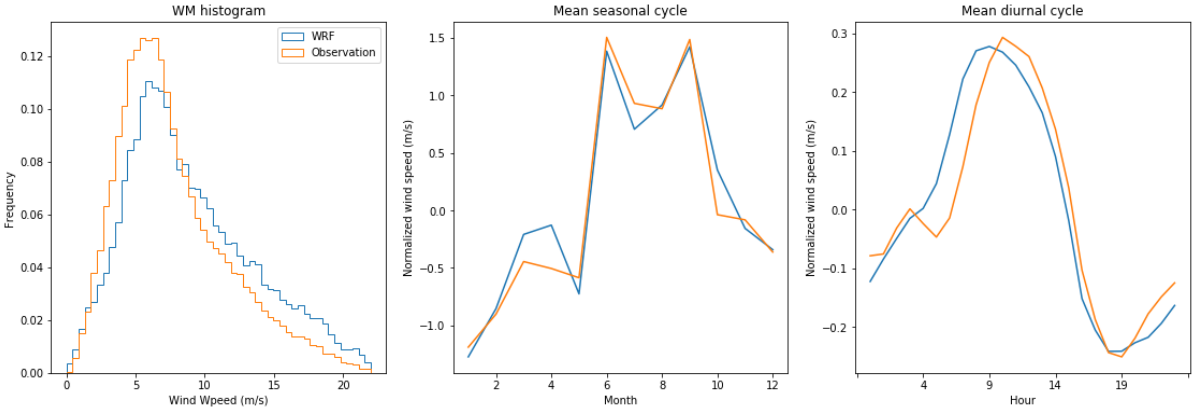

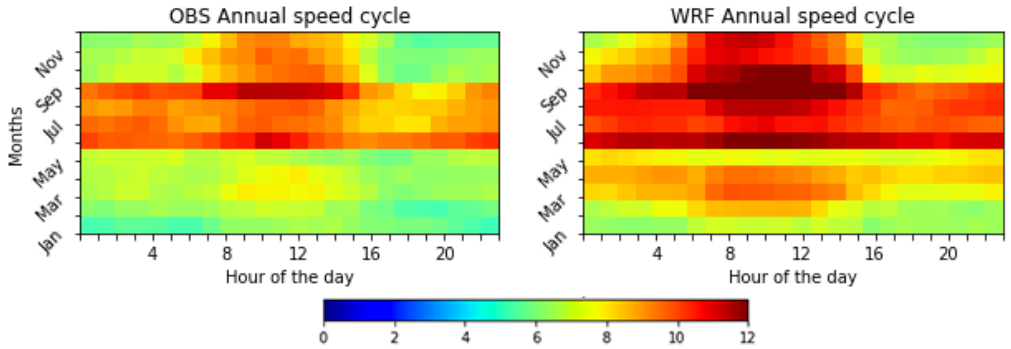

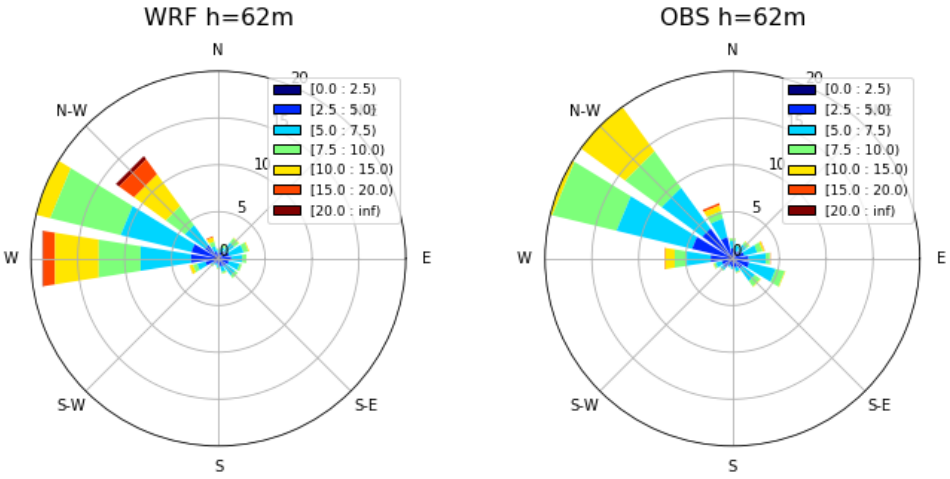

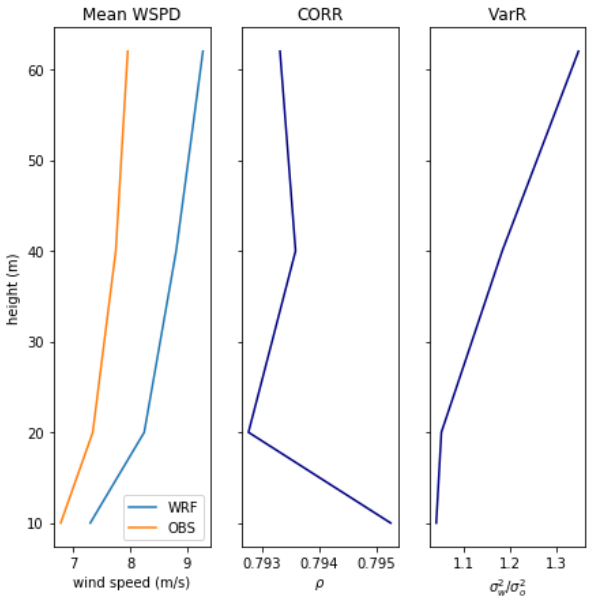

Figure 4.11 – As of 4.1 but for WM11.

At WM11 (Fig.4.11), the histogram of wind speeds shows that the model under-simulates the frequency of slower wind speeds (between 2–6 $\mathrm{m\,s^{-1}}$) and over-simulates the frequency of higher wind speeds ($>$9 $\mathrm{m\,s^{-1}}$). The WRF model captures the shape of the seasonal cycle well although there is a slight over-simulation of autumn and spring wind speeds. The diurnal cycle of wind speeds is well reproduced, however, there is a slight phase shift where the model simulates higher wind speeds in the morning than are observed. The wind rose shows the model simulates too many westerly winds and not enough north westerly winds. In the vertical structure there the model wind speeds are higher that the observed and the difference increases with height. Correlations between modelled and observed wind speeds are high (CORR = 0.79). At this mast higher wind speed variance is simulated by the model compared to the observed wind speed variance.

4.2.12 Eston (WM12)

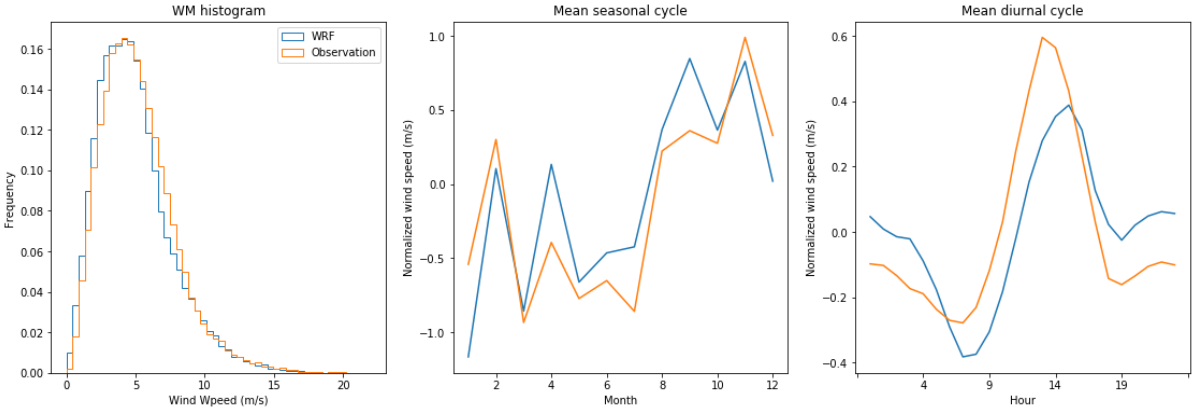

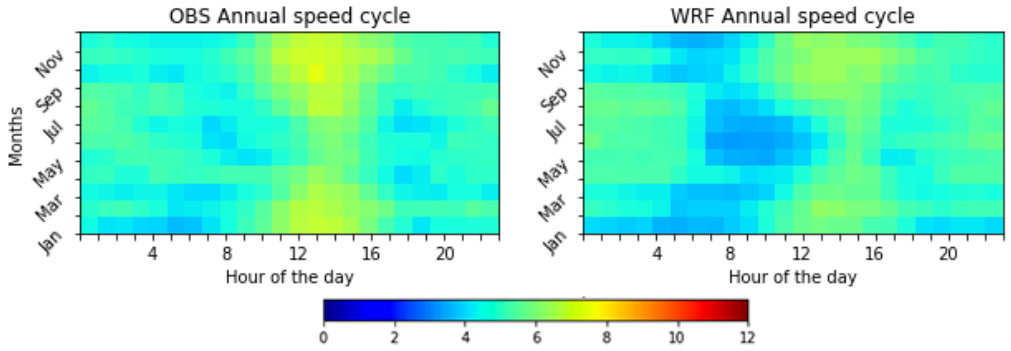

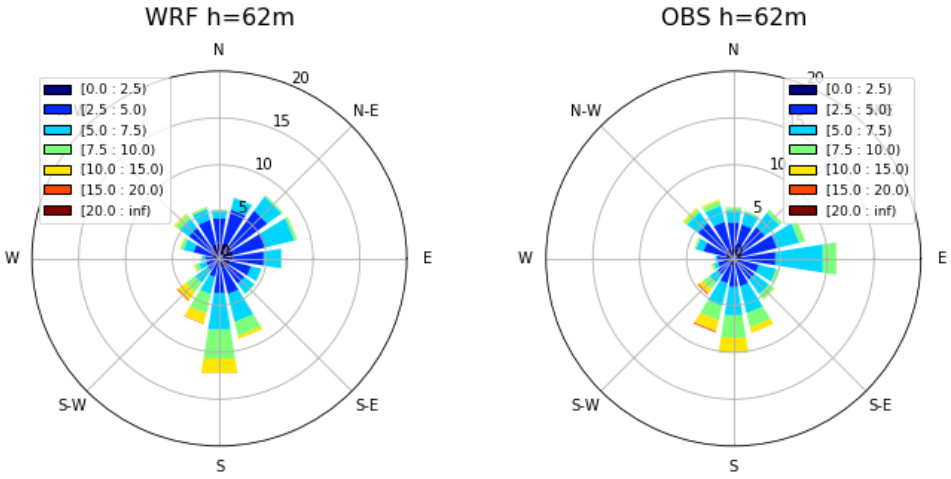

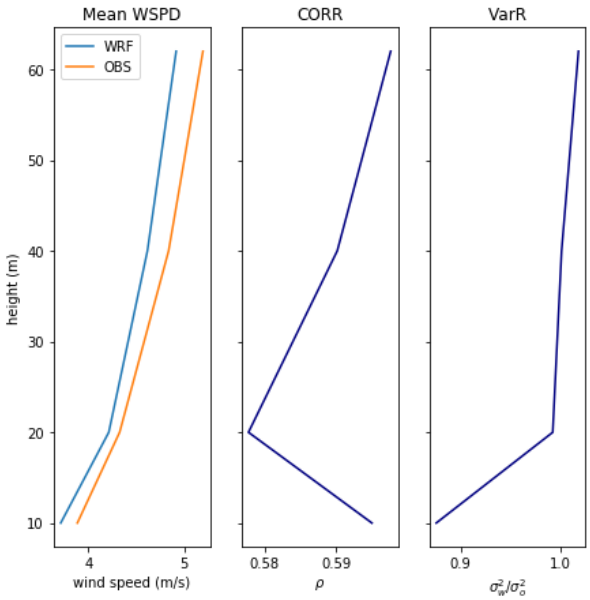

Figure 4.12 – As of 4.1 but for WM12.

At WM12 (Fig.4.12), the histogram of wind speeds shows that the model simulates the distribution of wind speeds very well. The WRF model captures the shape of the seasonal cycle well although it over-simulates autumn, winter and spring wind speeds and under-simulates summer wind speeds. In the diurnal cycle the model simulates night time wind speeds that are too high and day time wind speeds that are too low and there is a slight phase shift where the model simulates highest wind speeds later in the day compared to observed. The simulated wind rose compares well with the observed although the model simulates too many southerly winds and not enough easterly winds. In the vertical structure there the model and observed wind speeds are similar, although correlations between modelled and observed wind speeds are relatively low ($0.58 < \text{CORR} < 0.60$). At this mast simulated wind speed variance is comparable to observed wind speed variance.

4.2.13 Jozini (WM13)

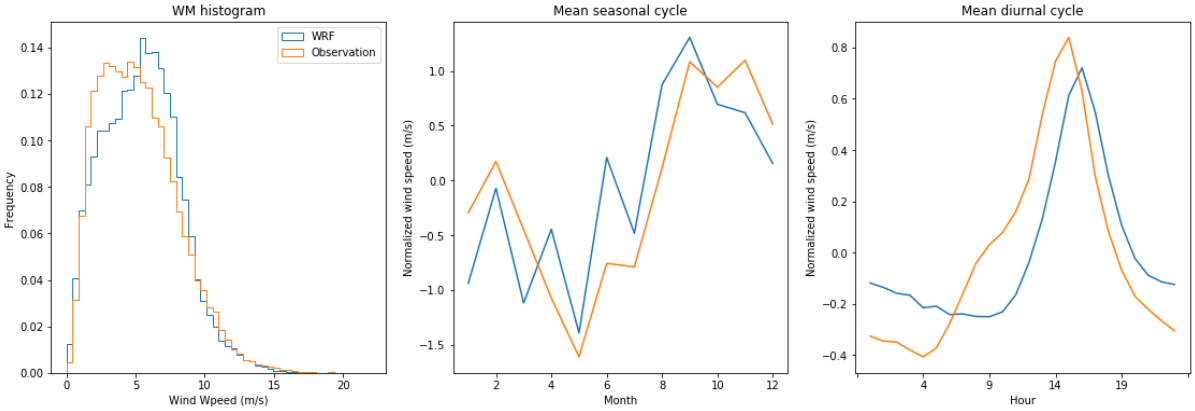

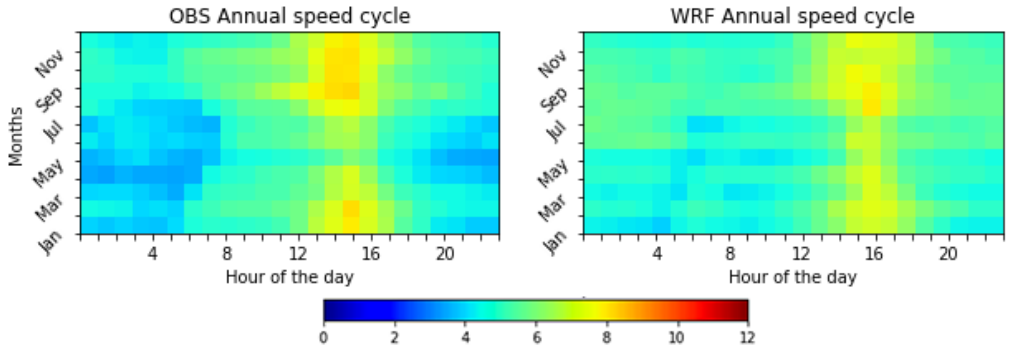

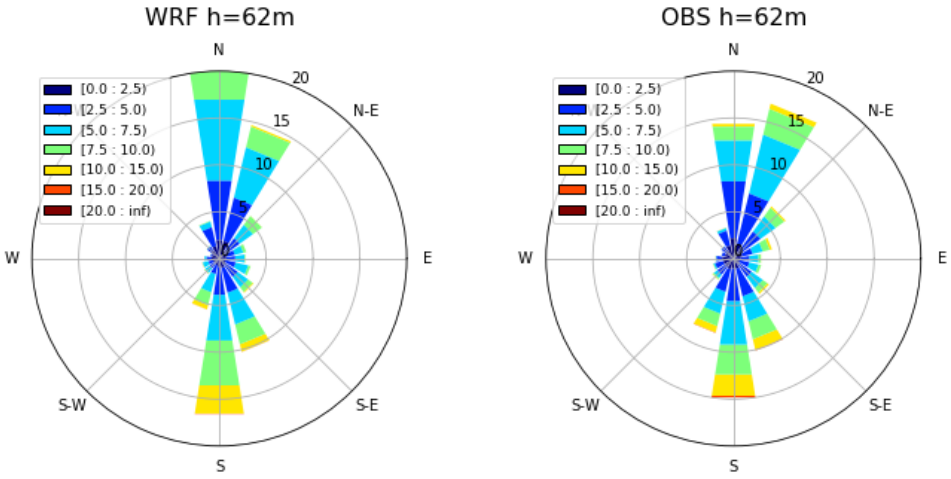

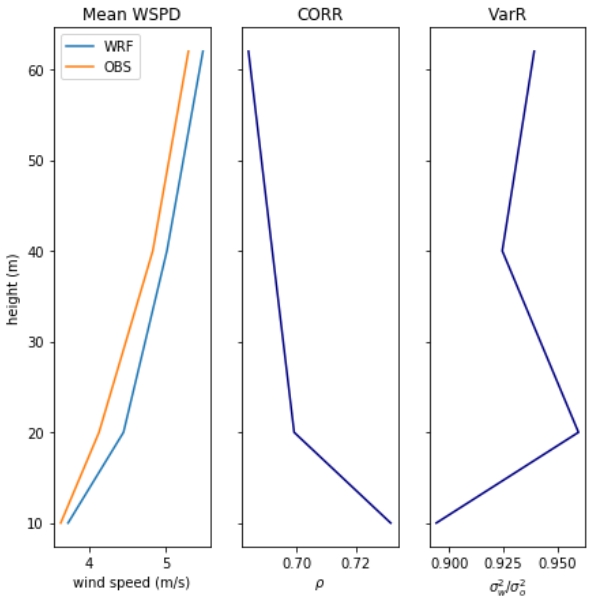

Figure 4.13 – As of 4.1 but for WM13.

At WM13 (Fig.4.13), the histogram of wind speeds shows that the model under-simulates the frequency of slower wind speeds (between 2-5 $\mathrm{m\,s^{-1}}$) and over-simulates the frequency of wind speeds between 5-10 $\mathrm{m\,s^{-1}}$. The WRF model captures the shape of the seasonal cycle although it over-simulates autumn, winter and spring wind speeds and under-simulates summer wind speeds. In the diurnal cycle the model simulates night time wind speeds that are too high and day time wind speeds that are too low and there is a slight phase shift where the model simulates highest wind speeds later in the day compared to observed. The simulated wind rose compares well with the observed although the model simulates too many northerly winds and not enough easterly winds. In the vertical structure there the model and observed wind speeds are similar and correlations between modelled and observed wind speeds are highest at the surface and lowest at the 62 m level ($0.69 < \mathrm{CORR} < 0.73$). At this mast simulated wind speed variance is comparable to observed wind speed variance.

4.2.14 Memel (WM14)

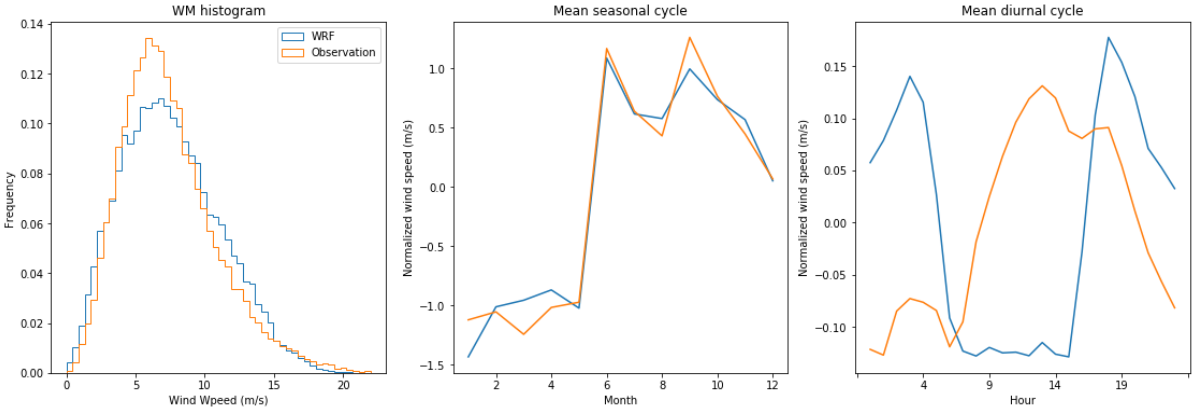

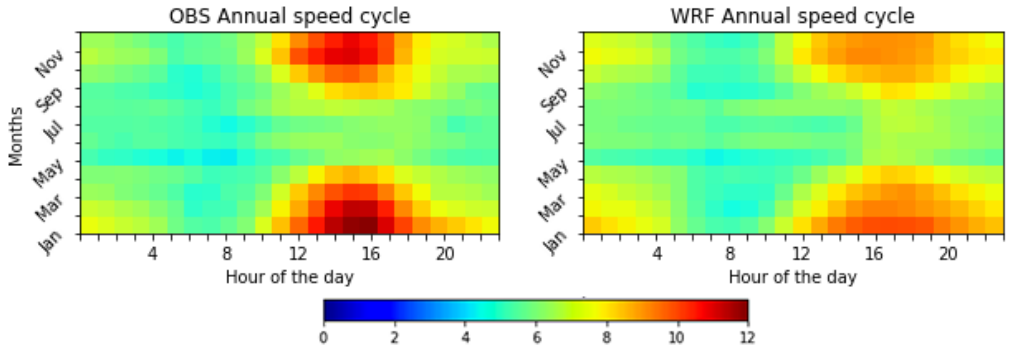

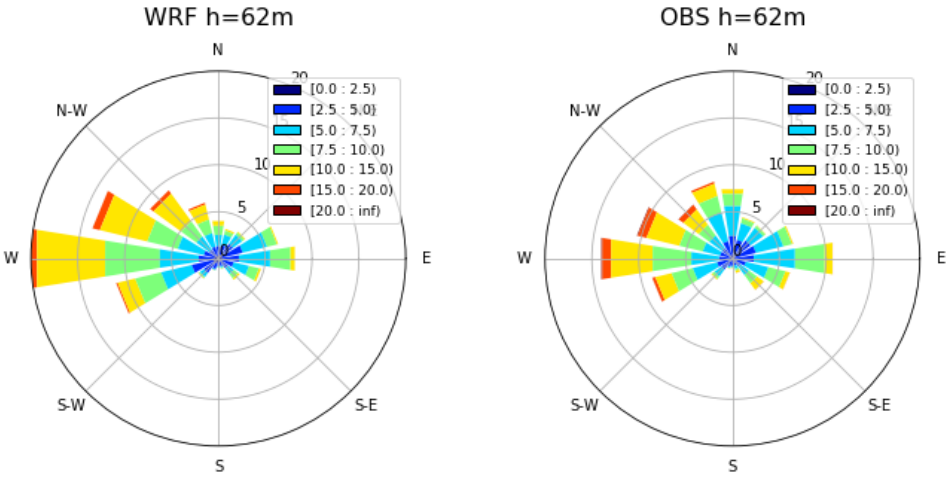

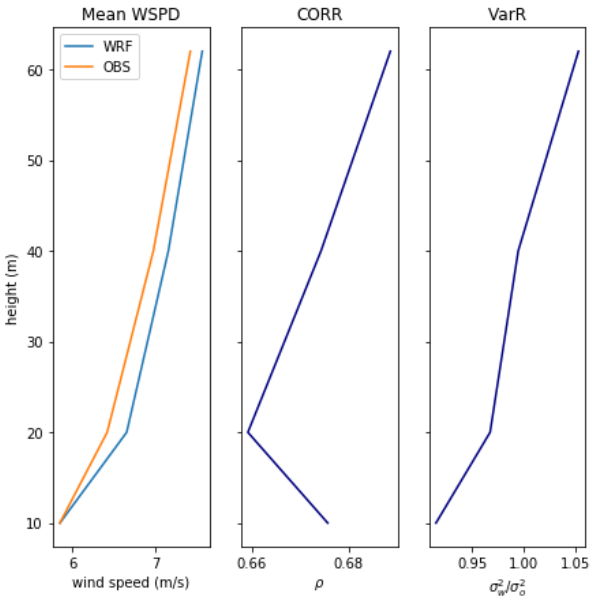

Figure 4.14 – As of 4.1 but for WM14.

At WM14 (Fig.4.2.14), the histogram of wind speeds shows that the model under-simulates the frequency of wind speeds between 4–8 $\mathrm{m\,s^{-1}}$) and slightly over-simulates the frequency of wind speeds between 10-15 $\mathrm{m\,s^{-1}}$. The WRF model captures the shape of the seasonal cycle well with only a small over-simulation of autumn wind speeds. The diurnal cycle of wind speed is very poorly reproduced by the model which produces 2 distinct wind speed peaks at (18:00 and 03:00) compared to an observed single peak at approximately 13h00. Low wind speeds in the model occur between 07:00-15:00 but in the observed record these occur between midnight and 07:00. Although the general shape of the simulated wind rose compares qualitatively with the observed, the model simulates too many westerly winds. In the vertical structure there the model and observed wind speeds are similar however, correlations between modelled and observed wind speeds are relatively low ($0.66 < \mathrm{CORR} < 0.68$). At this mast simulated wind speed variance is comparable to observed wind speed variance.

4.2.15 Winburg (WM15)

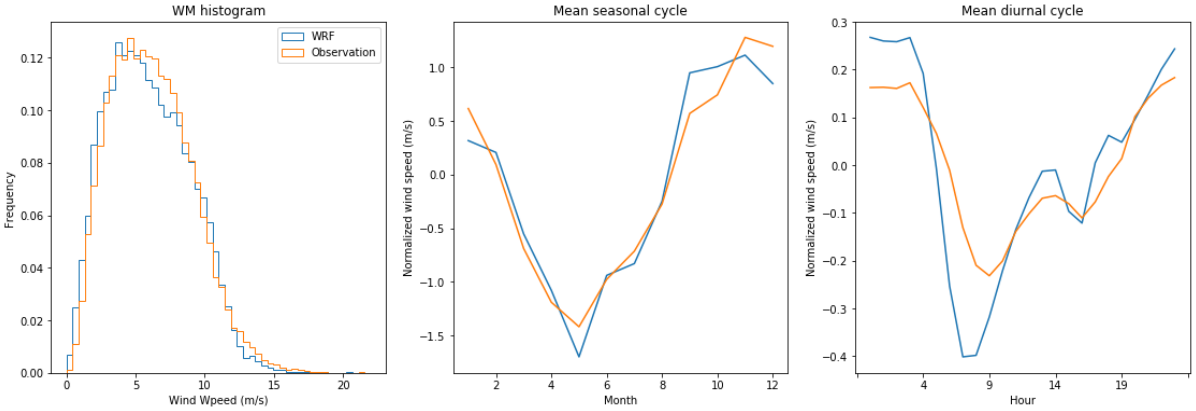

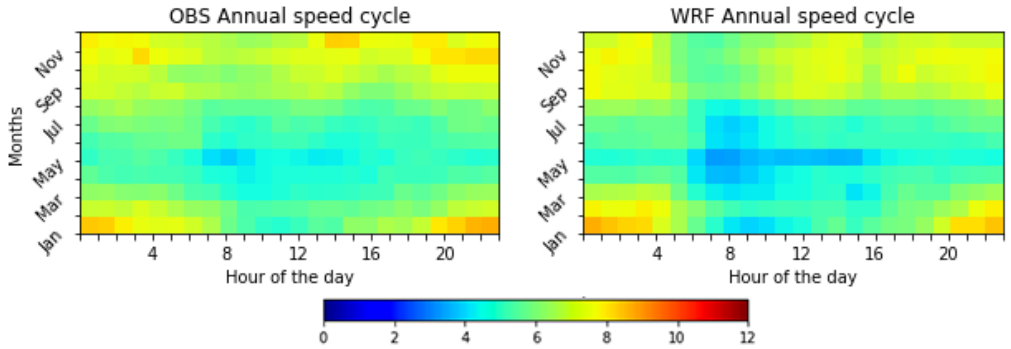

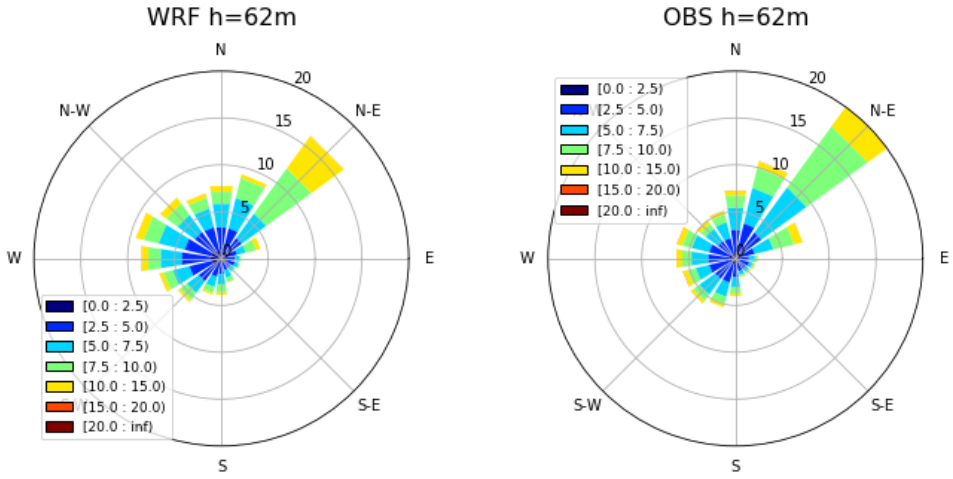

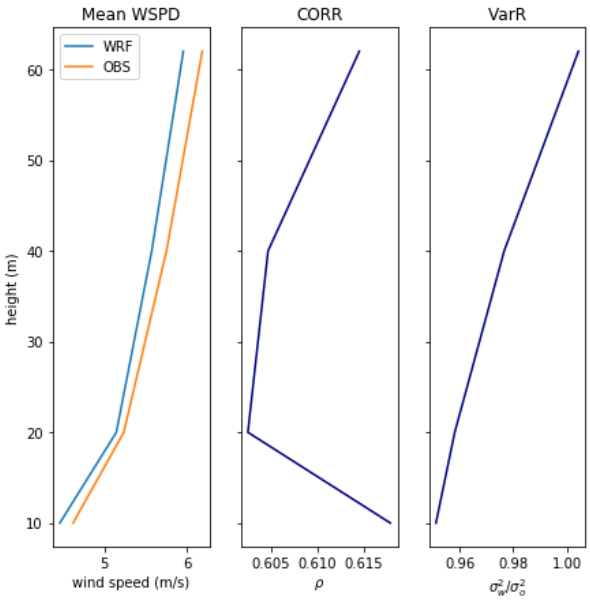

Figure 4.15 – As of 4.1 but for WM15.

At WM15 (Fig.4.2.15), the histogram of wind speeds shows that the model under-simulates the frequency of wind speeds between 5–9 $\mathrm{m\,s^{-1}}$. The WRF model captures the shape of the seasonal cycle well with only a small under-simulation of early winter wind speeds and over-simulation of spring wind speeds. The shape of the diurnal cycle of wind speed is reproduced by the model, however, simulated wind speeds between 00:00-04:00 are too high, between 04:00-10:00 too low, and generally too high for the rest of the day. The general shape of the simulated wind rose compares qualitatively with the observed, although the model does not simulate enough north easterly winds and slightly over-simulates the frequency of winds in most sectors of the western half of the wind rose. In the vertical structure there the model and observed wind speeds are similar however, correlations between modelled and observed wind speeds are relatively low ($0.60 < \mathrm{CORR} < 0.62$). At this mast simulated wind speed variance is comparable to observed wind speed variance.

4.3 Wind climatologies

A comparison between the observed wind climatology at the 62 m level of the masts and both WRF and downscaled WRF results is presented in Table 4.2 and Figure 4.16. Differences between the raw WRF output, UW(R), and observed wind speed climatologies are generally lower than 0.5 $\mathrm{m\,s^{-1}}$ with the notable exception of WM11 (1.53 $\mathrm{m\,s^{-1}}$) and also WM03 (-0.71 $\mathrm{m\,s^{-1}}$) and WM06 (0.66 $\mathrm{m\,s^{-1}}$). The difference between downscaled WRF wind speed climatologies, UW(D), and observed wind speed climatologies and are higher than 0.5 $\mathrm{m\,s^{-1}}$ at 4 masts, WM01 (-0.71 $\mathrm{m\,s^{-1}}$), WM03 (-0.72 $\mathrm{m\,s^{-1}}$), WM11 (0.91 $\mathrm{m\,s^{-1}}$) and WM13 (0.66 $\mathrm{m\,s^{-1}}$). The downscaled WRF wind speed climatologies improve on the WRF raw wind speed climatologies at masts WM05-WM12, degrade the the WRF raw wind speed climatologies at masts WM01, WM03, WM04, WM13–15 (although at WM03, WM04 and WM15 the values are small, between 0.01–0.08 $\mathrm{m\,s^{-1}}$) and produces the same the wind speed climatology at masts WM02. Downscaling of the raw WRF data results in the largest error reductions in regions of topographic complexity. In regions with a relatively flatter land surface the downscaling of the raw WRF data generally does not reduce error and in some cases introduces additional error, particularly at WM01, WM13 and WM14. However, the mean absolute error of wind speed climatology across all masts is reduced by downscaling of the raw WRF data.

Table 4.2 – Comparison of the mean wind speed at 62 m AGL for all WASA masts for the observations ($\overline{U}_O$), and the WRF raw ($\overline{U}_{W(R)}$) and WRF downscaled ($\overline{U}_{W(D)}$). All concurrent observations are used.

Station	N samples [-]	$\overline{U}_O$ ($\mathrm{m\,s^{-1}}$)	$\overline{U}_{W(R)}$ ($\mathrm{m\,s^{-1}}$)	$\overline{\Delta U}_{W(R)-O}$ (%)	$\overline{U}_{W(D)}$ ($\mathrm{m\,s^{-1}}$)	$\overline{\Delta U}_{W(D)-O}$ (%)
WM01	131,100	6.11	5.68	−7.03	5.40	−11.62
WM02	128,044	6.19	6.48	4.68	6.48	4.68
WM03	131,849	7.15	6.44	−9.93	6.43	−10.07
WM04	53,483	6.71	6.72	0.15	6.69	−0.30
WM05	122,832	8.39	8.08	−3.69	8.24	−1.79
WM06	127,604	7.33	7.99	9.00	7.62	3.96
WM07	131,559	6.93	7.32	5.63	6.68	−3.61
WM08	122,946	7.29	6.88	−5.62	7.46	2.33
WM09	111,651	7.98	8.23	3.13	8.11	1.63
WM10	121,735	6.67	6.55	−1.80	6.75	1.20
WM11	37,290	7.60	9.13	20.13	8.51	11.97
WM12	37,800	5.19	4.91	−5.39	5.39	3.85
WM13	38,721	5.23	5.45	4.21	5.89	12.62
WM14	39,405	7.41	7.56	2.02	7.80	5.26
WM15	37,062	6.22	5.97	-4.02	5.89	−5.31
Mean error				0.76		0.99
Mean absolute error (MAE)				5.43		4.83

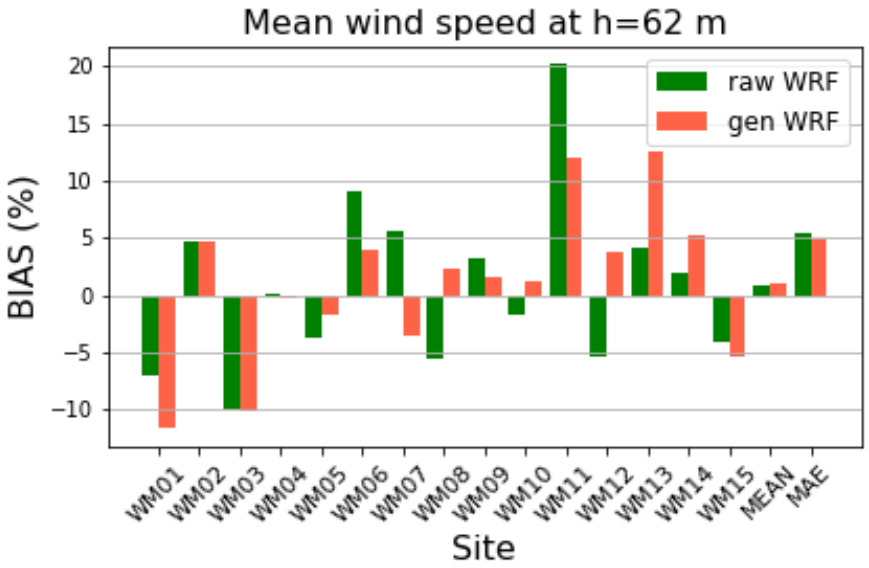

Figure 4.16 – Biases in the long-term wind speed at 62 m AGL for all sites. Last two are the mean error and Mean absolute error.

4.4 Verification at each site

Mast data is compared with values of the corresponding model grid cell the mast would be in. The WRF-derived climatologies are further generalised and downscaled to 62 m AGL using the procedure outlined in Chapter 2. The values of mean wind speed are compared in Table 4.2. Here we compare the wind roses from the observations, the raw WRF output and the downscaled WRF results. As the wind rose results are presented above (4.3), we focus on the differences between the raw WRF output and the downscaled WRF results to highlight where the downscaling is important and what type of value the downscaling adds in these cases. Not all masts are discussed, only those with notable differences, namely WM01, WM08, WM11, WM13 and WM14.

4.4.1 Alexander Bay (WM01)

The observed and simulated generalised wind climate at WM01 are shown in Fig. 4.17. Here the downscaling degrades the raw WRF result as it produces a lower wind speed climatology by -0.28 m s^{-1} compared to the raw WRF data. The downscaling produces too few wind speeds in the ranges 7.5–10 m s^{-1} and 10–15 m s^{-1} compared to the raw WRF results, which already has a negative bias as very high wind speeds from the south (15–20 m s^{-1}) are not correctly simulated.

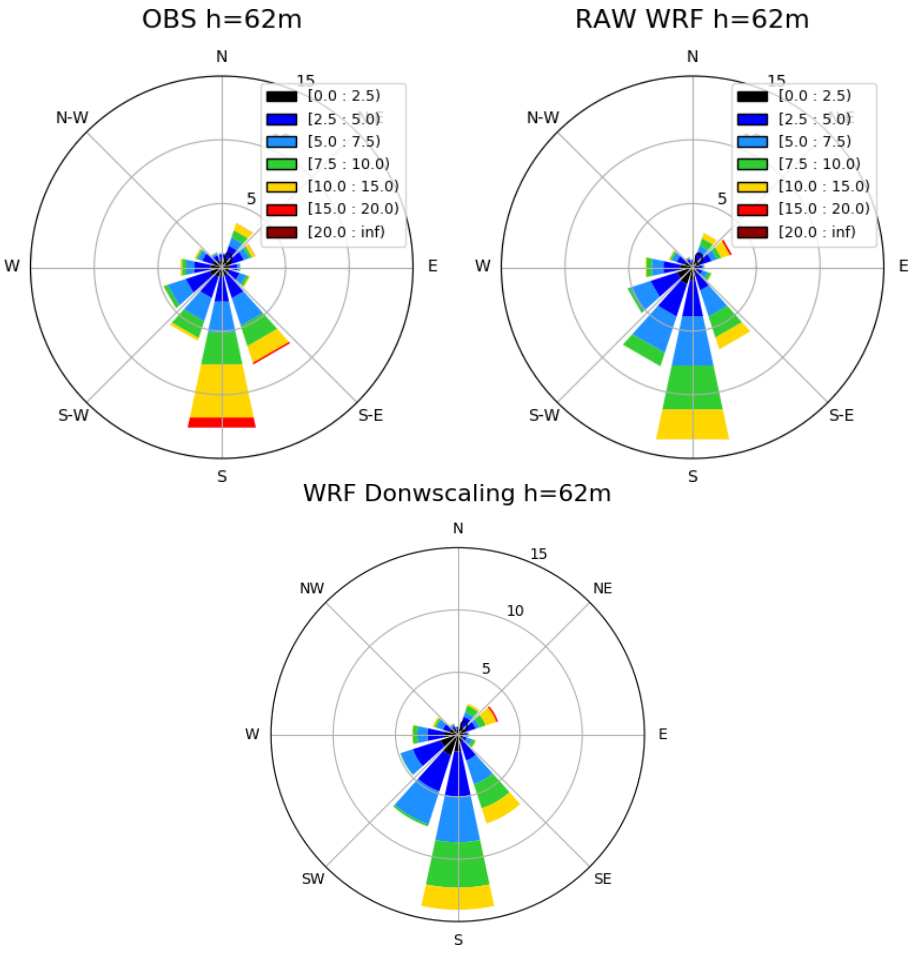

Figure 4.17 – Comparison of the WRF wind climatology at 62 m AGL at site WM01.

4.4.2 Clavinia (WM02)

The observed and simulated generalised wind climate at WM02 are shown in Fig. 4.18.

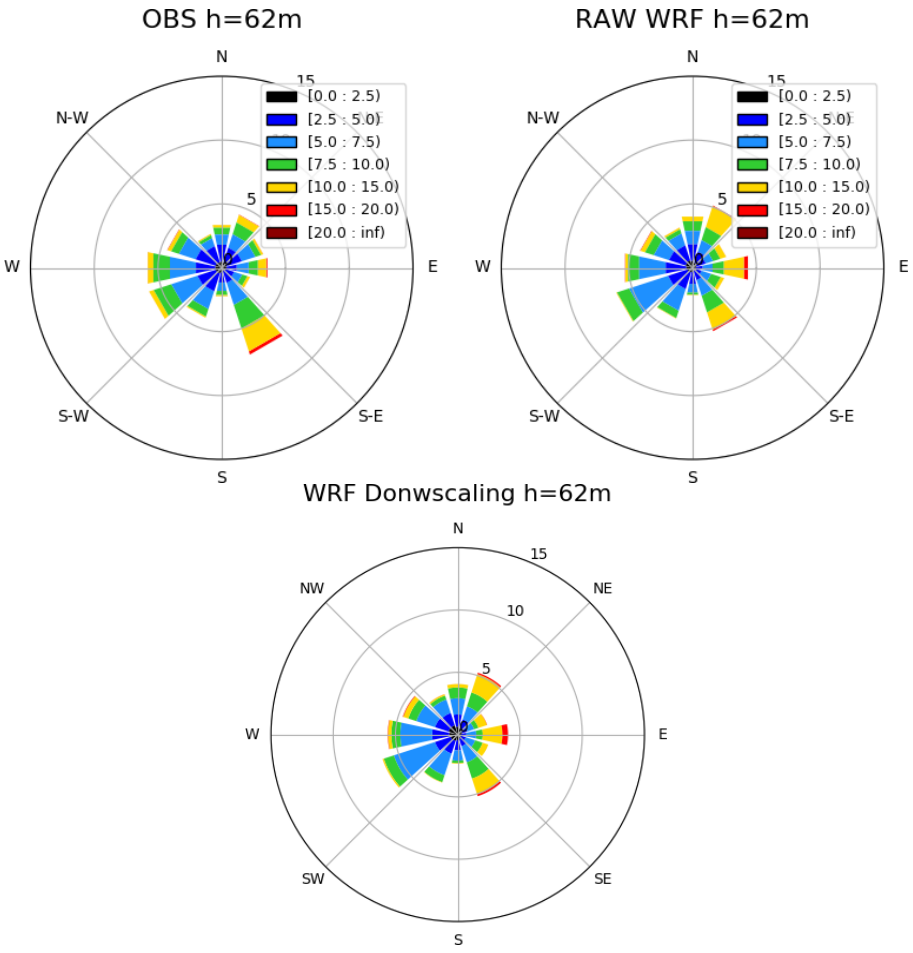

Figure 4.18 – Comparison of the WRF wind climatology at 62 m AGL at site WM02.

4.4.3 Vredendal (WM03)

The observed and simulated generalised wind climate at WM03 are shown in Fig. 4.19.

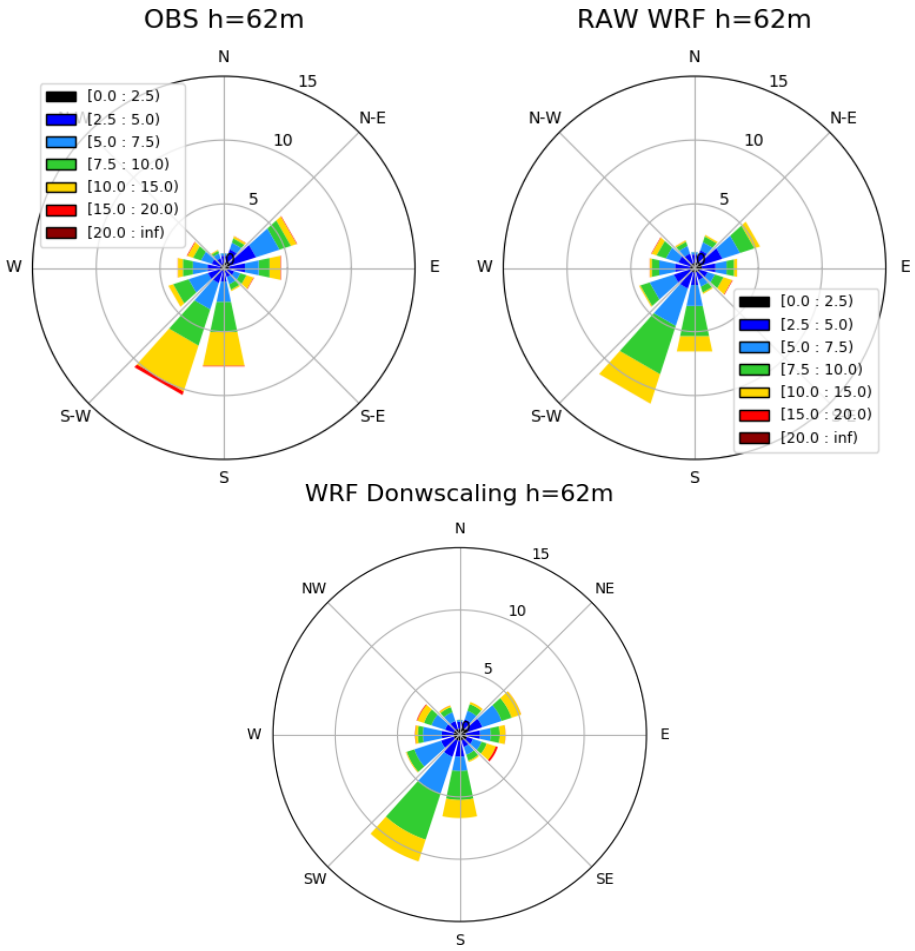

Figure 4.19 – Comparison of the WRF wind climatology at 62 m AGL at site WM03.

4.4.4 Vredenburg (WM04)

The observed and simulated generalised wind climate at WM04 are shown in Fig. 4.20.

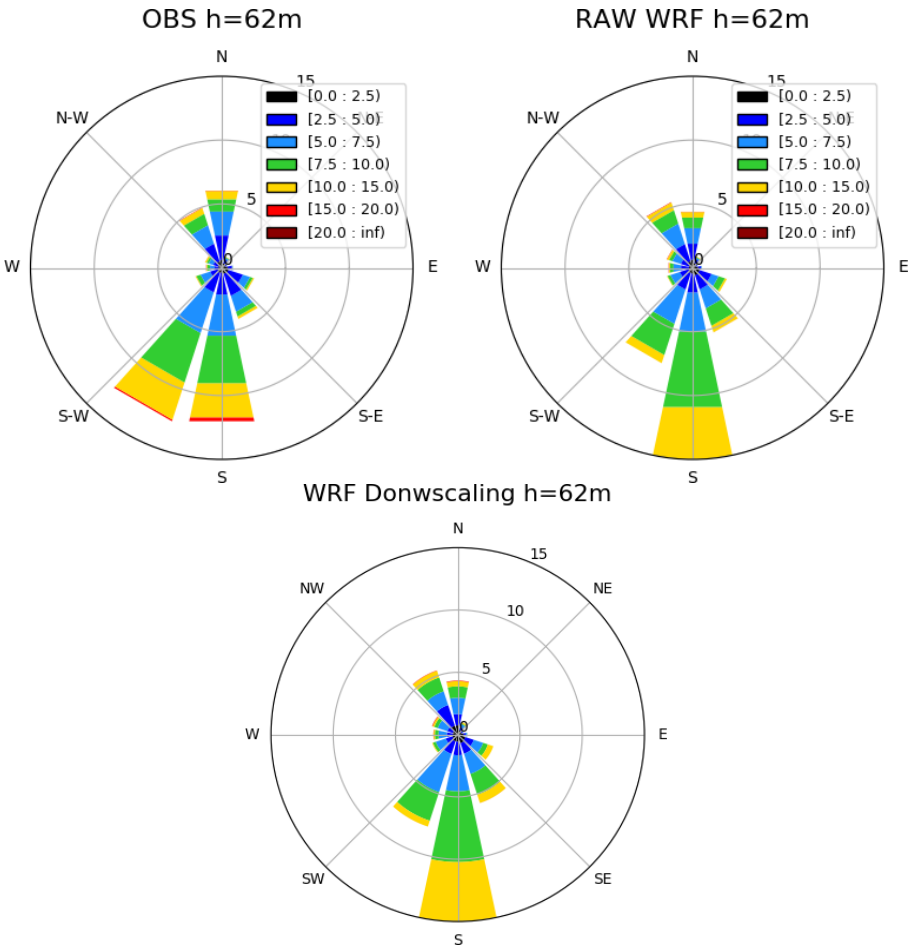

Figure 4.20 – Comparison of the WRF wind climatology at 62 m AGL at site WM04.

4.4.5 Napier (WM05)

The observed and simulated generalised wind climate at WM05 are shown in Fig. 4.21.

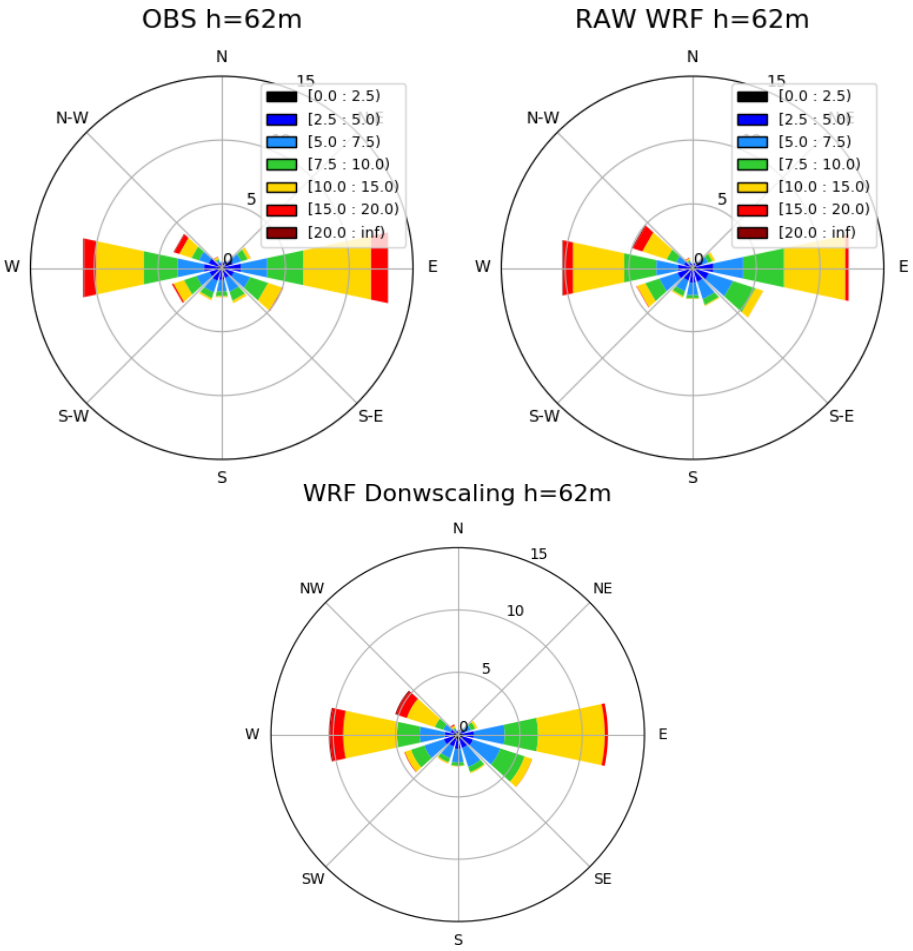

Figure 4.21 – Comparison of the WRF wind climatology at 62 m AGL at site WM05.

4.4.6 Sutherland (WM06)

The observed and simulated generalised wind climate at WM06 are shown in Fig. 4.22.

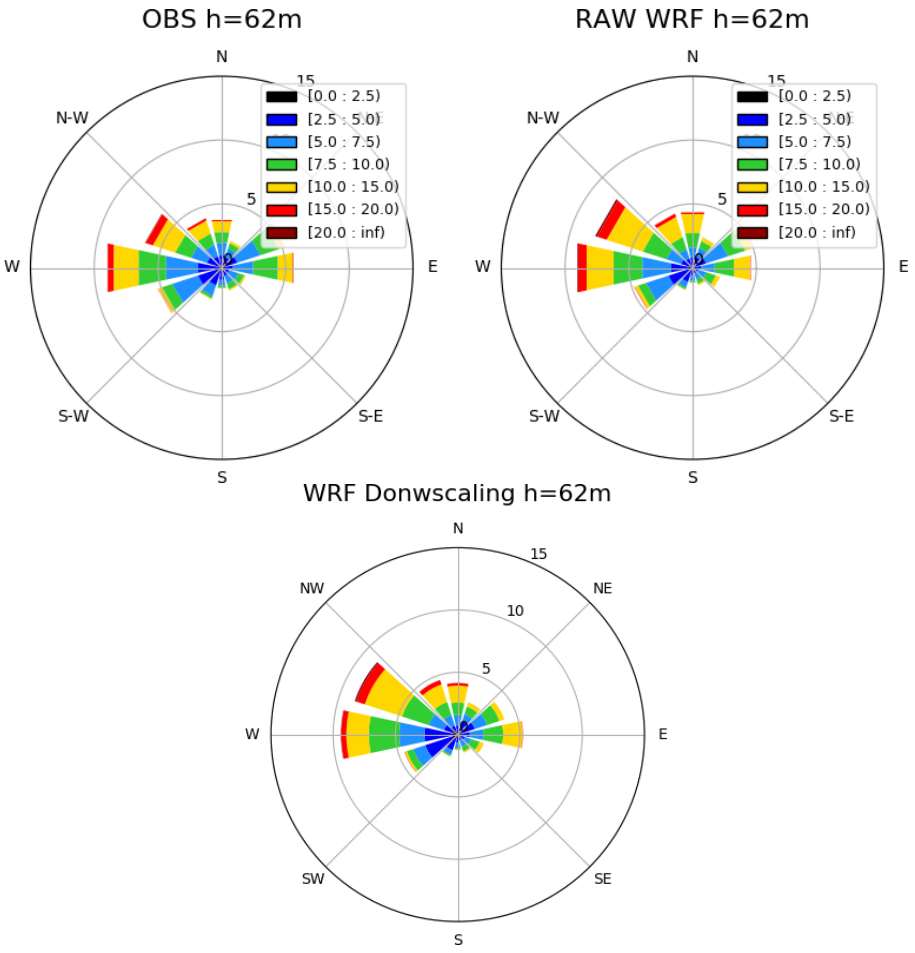

Figure 4.22 – Comparison of the WRF wind climatology at 62 m AGL at site WM06.

4.4.7 Beaufort West (WM07)

The observed and simulated generalised wind climate at WM07 are shown in Fig. 4.23.

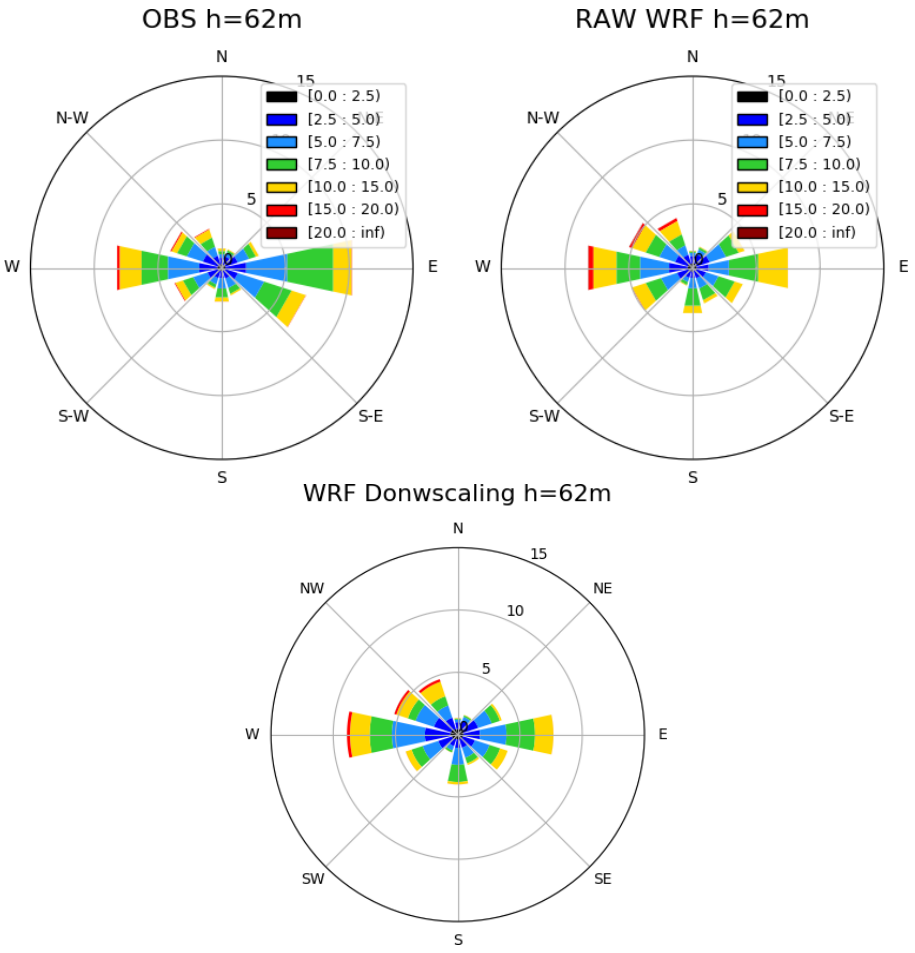

Figure 4.23 – Comparison of the WRF wind climatology at 62 m AGL at site WM07.

4.4.8 Humansdorp (WM08)

The observed and simulated generalised wind climate at WM08 are shown in Fig. 4.24. Here the downscaling improves on the raw WRF wind speed climatology results but degrades the wind rose. Too many occurrences of winds in the WSW sector are downscaled whereas in the raw WRF results the winds roses are more alike.

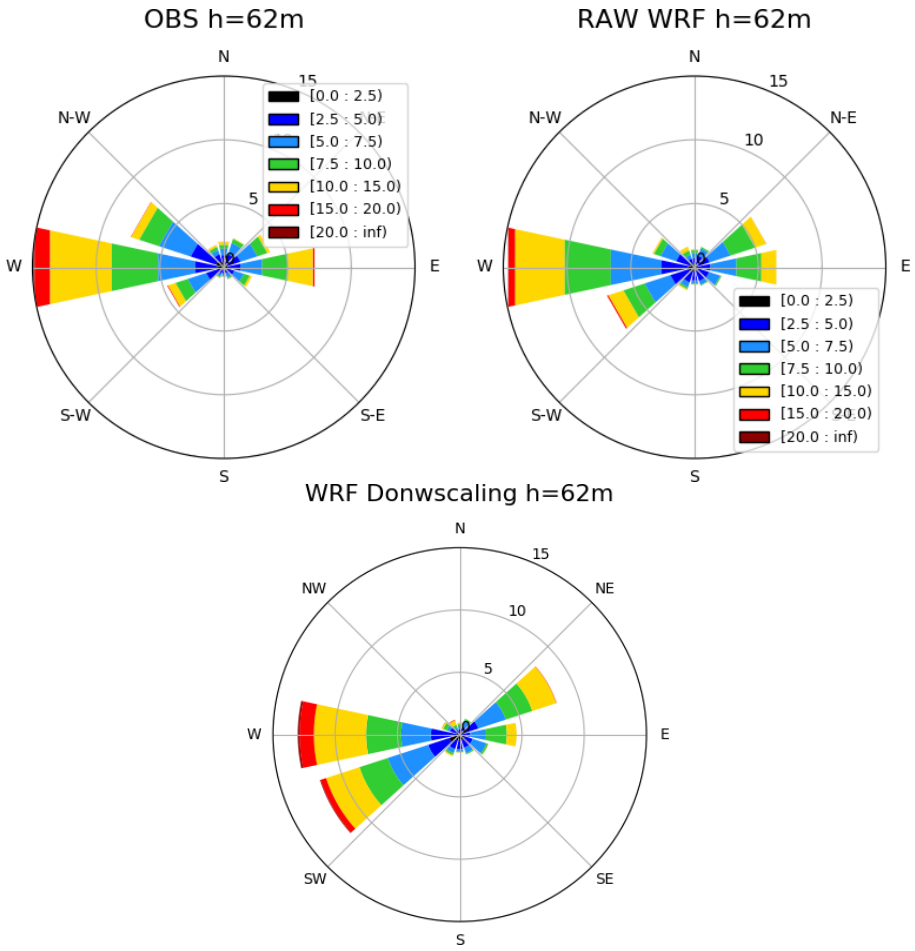

Figure 4.24 – Comparison of the WRF wind climatology at 62 m AGL at site WM08.

4.4.9 Noupoort (WM09)

The observed and simulated generalised wind climate at WM09 are shown in Fig. 4.25.

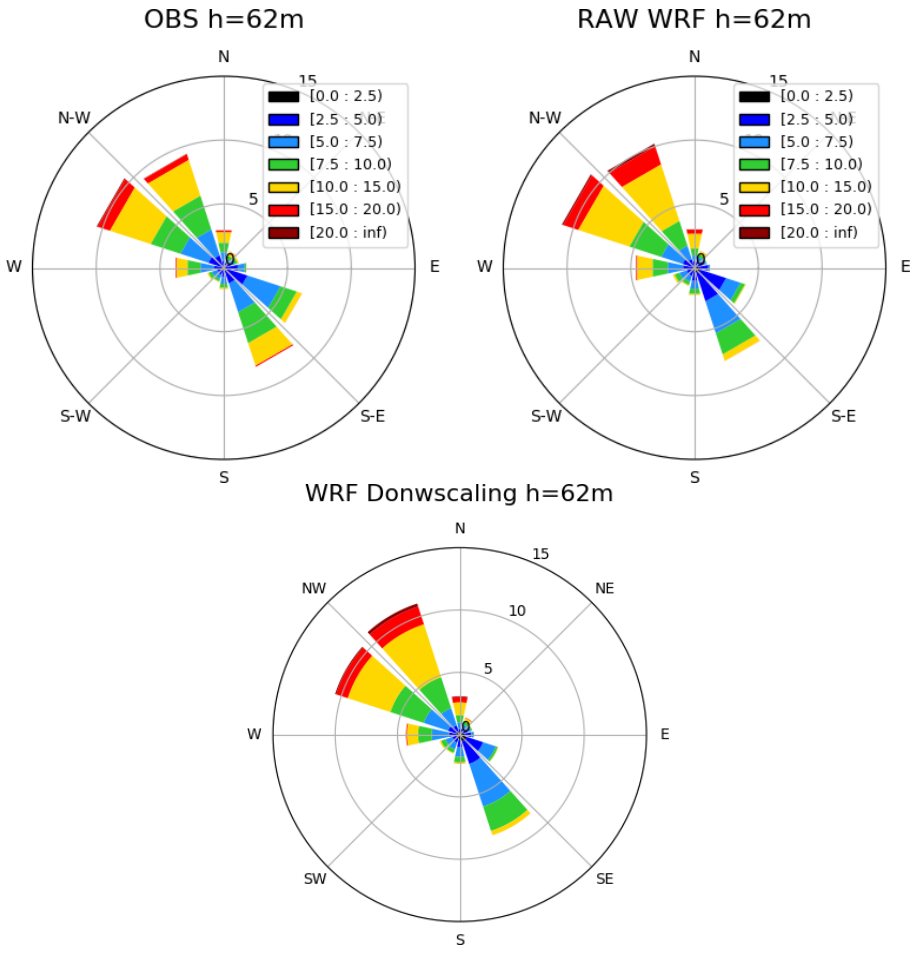

Figure 4.25 – Comparison of the WRF wind climatology at 62 m AGL at site WM09.

4.4.10 Butterworth (WM10)

The observed and simulated generalised wind climate at WM10 are shown in Fig. 4.26.

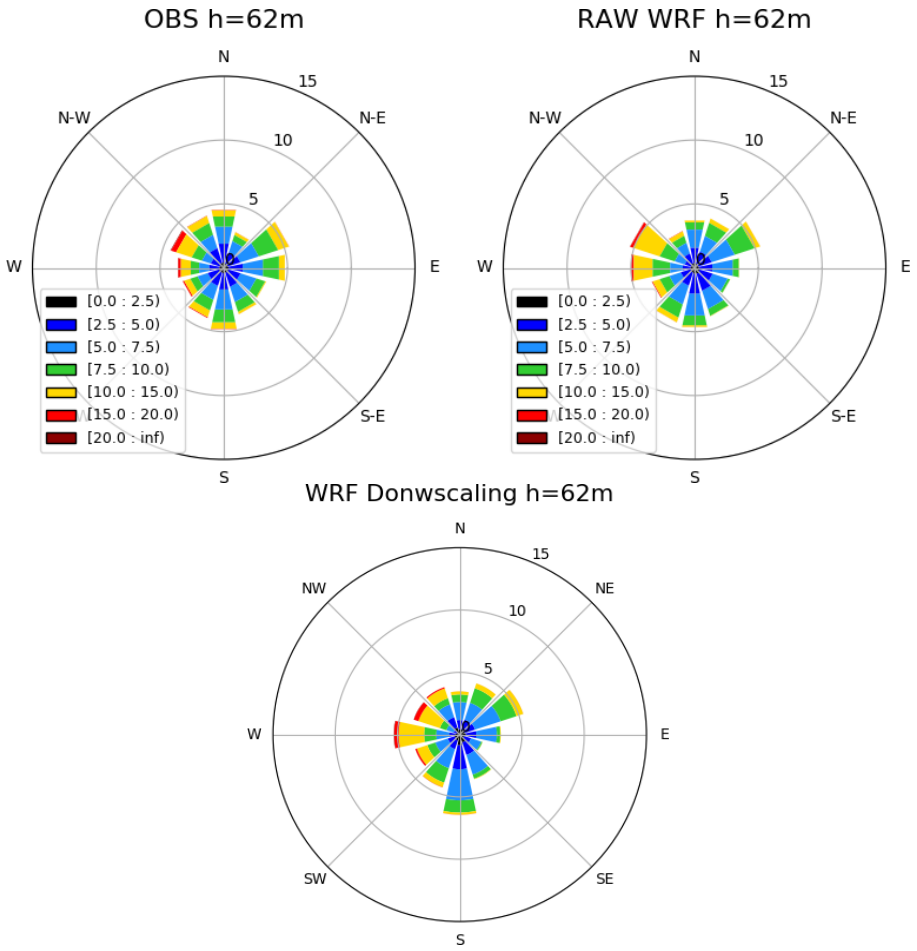

Figure 4.26 – Comparison of the WRF wind climatology at 62 m AGL at site WM10.

4.4.11 Rhodes (WM11)

The observed and simulated generalised wind climate at WM11 are shown in Fig. 4.27. Here, where the raw WRF has the largest wind speed climatology error, the downscaling reduces this over-speed error from 1.53 $m\,s^{-1}$ (20.13%) to 0.91 $m\,s^{-1}$ (12%). The wind rose shows the downscaling reduces the frequency of frequency of north westerly winds between 10-15 $m\,s^{-1}$ and westerly winds between 10–20 $m\,s^{-1}$, although westerly winds are still over simulated. At this very topographically complex site, the downscaling greatly improves on the raw WRF output.

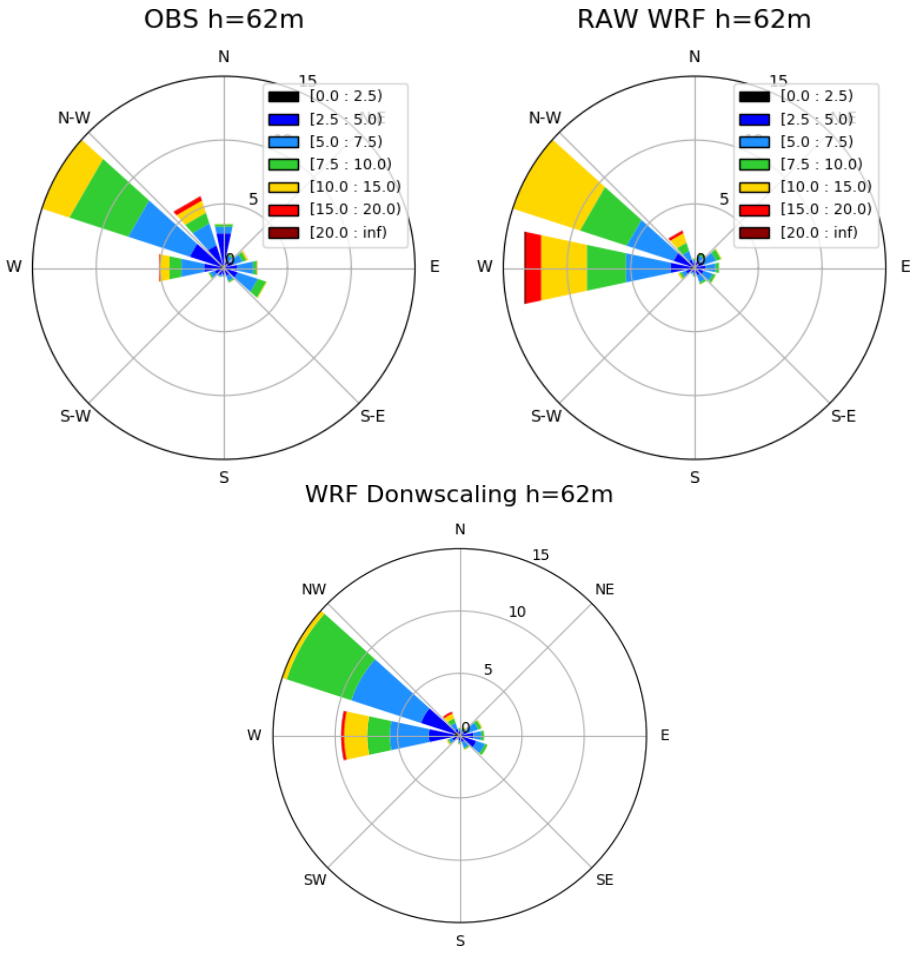

Figure 4.27 – Comparison of the WRF wind climatology at 62 m AGL at site WM11.

4.4.12 Eston (WM12)

The observed and simulated generalised wind climate at WM12 are shown in Fig. 4.28.

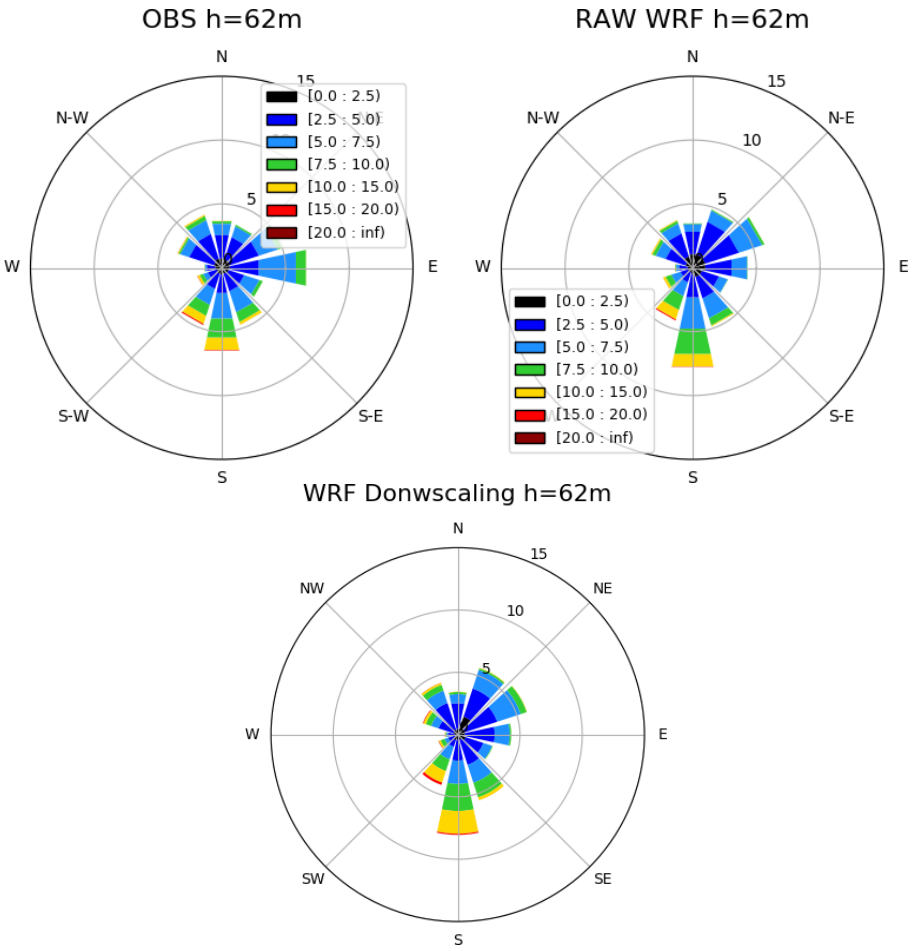

Figure 4.28 – Comparison of the WRF wind climatology at 62 m AGL at site WM12.

4.4.13 Jozini (WM13)

The observed and simulated generalised wind climate at WM13 are shown in Fig. 4.29. Here the downscaling degrades the raw WRF result as it produces a higher wind speed climatology by 0.44 m s^{-1} compared to the raw WRF data. The downscaling introduces a higher frequency of wind speeds in the 10–15 m s^{-1} particularly in the southerly and northerly sectors.

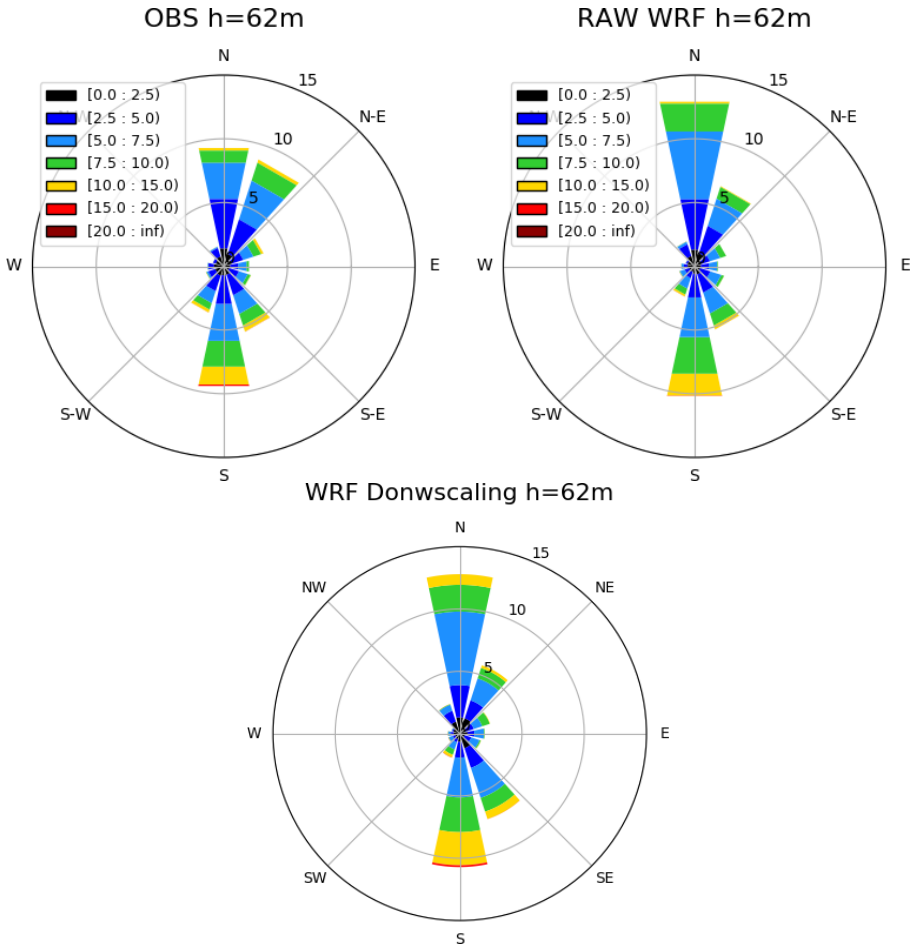

Figure 4.29 – Comparison of the WRF wind climatology at 62 m AGL at site WM13.

4.4.14 Memel (WM14)

The observed and simulated generalised wind climate at WM14 are shown in Fig. 4.30. Here the downscaling degrades the raw WRF result as it produces a higher wind speed climatology compared to the raw WRF results by 0.24 m s^{-1}. The downscaling introduces a much higher frequency of wind speeds in the 10–15 m s^{-1} in the westerly sector.

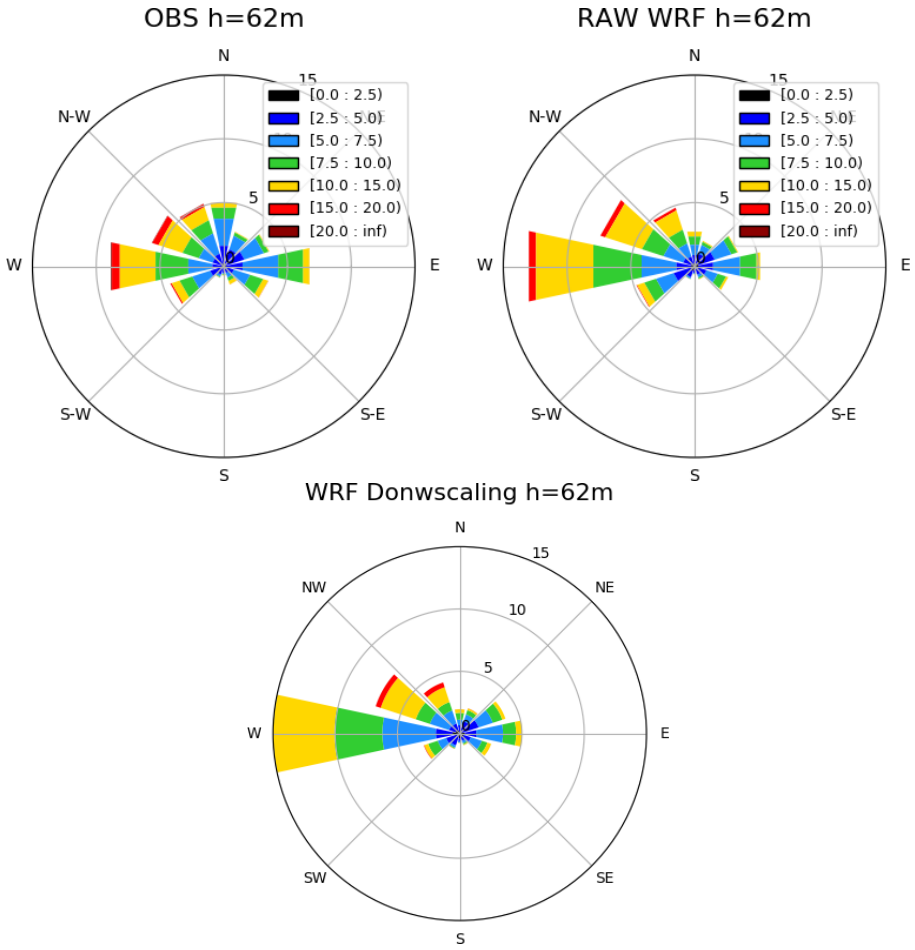

Figure 4.30 – Comparison of the WRF wind climatology at 62 m AGL at site WM14.

4.4.15 Winburg (WM15)

The observed and simulated generalised wind climate at WM15 are shown in Fig. 4.31.

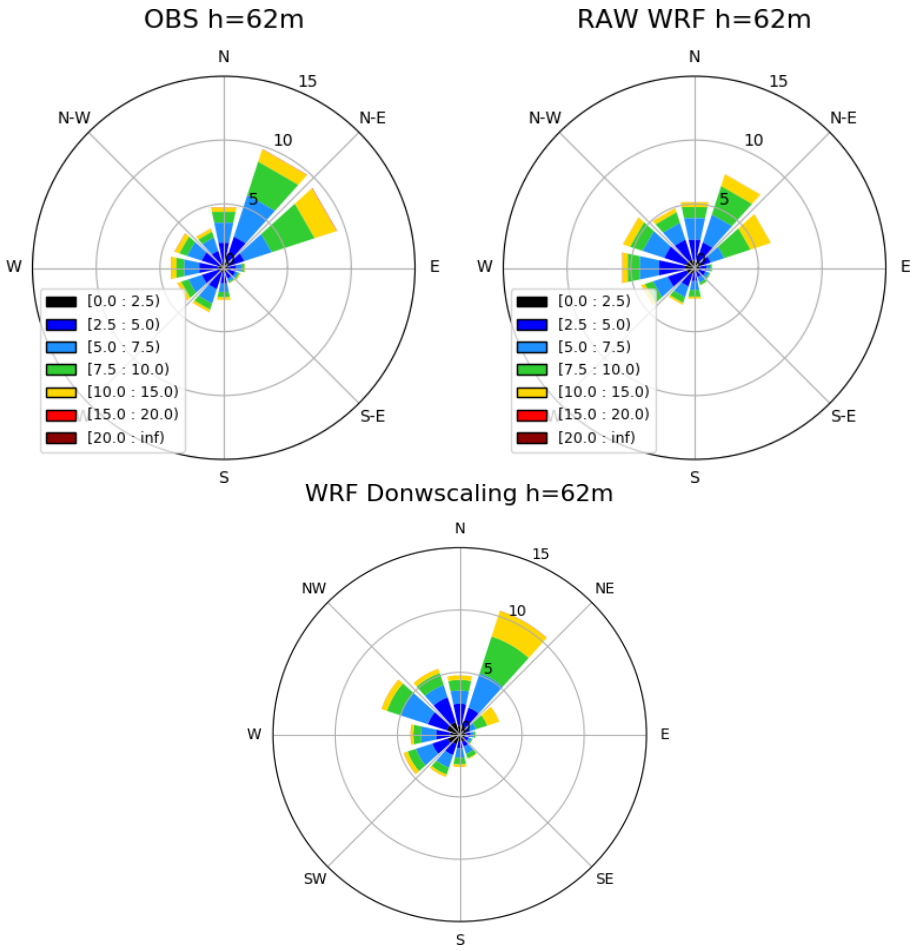

Figure 4.31 – Comparison of the WRF wind climatology at 62 m AGL at site WM15.

In the context of wind rose climatology, downscaling the WRF raw results both improves and degrades raw WRF results depending on the location. Downscaling can also improve the wind speed climatology but degrade the wind rose climatology as seen at WM08. However, relatively large changes in the wind rose climatology between the raw WRF and the downscaled WRF results were only noted at 3 of the 15 masts (WM08, WM11, WM14). Given the results reported in 4.3, this suggests that the downscaling contributes more to a general reduction of wind speed climatology bias than wind rose climatology bias.

Chapter 5

Ensemble modelling and uncertainty

Numerical wind atlas methodologies have been devised to facilitate estimating wind energy resources over large areas, since it is not possible to blanket the entire project with wind measurement masts. The wind atlas is a database that contains wind statistics (e.g., wind speed distributions) per wind direction and height above ground level often on a regular grid covering a large geographic area.

The method developed at DTU Wind Energy, and used in many wind atlas projects, uses the Weather Research and Forecasting (WRF) model in a dynamical downscaling mode to produce mesoscale analysis. The method has recently been documented in Hahmann et al. (2015c) and verified against tall masts in the North and Baltic Sea. The same method was used and verified against measurements in the recent Wind Atlas for South Africa (Hahmann et al., 2015a).

Numerical wind atlases are validated against measurements from tall wind masts. The validation errors are useful to assess the possible errors around the observation sites. However, because of their limited number the measurement masts only sample the large variety of wind climates and terrains across a given area providing an illustration of the range of errors and uncertainties that generally would be expected at similar sites. Away from these sites, it is not straightforward to estimate the possible errors in wind resource assessments made from the wind atlas, in particular at sites that are either far from validation masts or at sites of a different wind climate or topography.

In an analogous way to what is done in Numerical Weather Prediction (NWP) and climate prediction, we explore the possibility to estimate the uncertainty of the wind resource estimate based on and ensemble of WRF simulations. These ensemble simulations are created by runs with different physical parameterisations or by introducing variations in the initial atmosphere and surface conditions. The results of the ensemble simulations can be processed to give a "map" of the spread of the wind resource estimation. By comparing these "maps" with the observed wind resources at the sites and by relating these to the terrain complexity and wind climate complexity, it might be possible to diagnose the geographic distribution of possible errors in the wind resources away from the observation sites.

5.1 Ensembles in NWP

Early in the 20th century it was recognised that small uncertainties in the initial conditions or the prediction model will develop over time to meso- and synoptic-scale errors, and thus the

predictability of the detailed weather evolution is limited (Lorenz, 1969). In NWP an objective way to estimate the uncertainty of the forecast is to run an ensemble prediction system, which provides a probabilistic forecast of the atmospheric evolution (Berner et al., 2011).

To account for initial condition error, it is common practice to start each member of the ensemble from slightly different initial conditions, but in generating such set of initial conditions one must attempt to perturb the model in directions that will exhibit maximal error growth. However, even with the standard operational methods, ensemble forecasts tend to be underdispersive and underestimate the true uncertainty of the model evolution (Buizza et al., 2005).

Another major contribution to the forecast uncertainty is the model error, from either parameter and parameterisation uncertainty, or altogether unrepresented subgrid-scale processes (Berner et al., 2011). The errors that arise from a misrepresentation of subgrid-scale processes can affect both the variability and the mean error of a model. But contrary to the initial condition approach, there is no unique method to represent these errors in an ensemble prediction system. The suggested approaches are: stochastic dynamic models (Palmer, 2001), multiple physics schemes (e.g. Lee et al., 2012), or parameter variations in the physics schemes (Stainforth et al., 2005).

5.2 Ensembles in climate prediction

In long-term climate prediction, where exact prediction of the time evolution of the atmosphere is not of vital importance, ensemble simulations are being used to sample structural model uncertainties arising from choices such as resolution, the set of processes included in the model and the basic assumptions on which its parametrisations are based (Murphy et al., 2004). This approach is the standard in current Intergovernmental Panel on Climate Change reports (e.g. IPCC, 2013).

5.3 Ensembles in dynamical downscaling

Ensemble simulations are also used in the context of dynamical downscaling from an ensemble of global model predictions, e.g. CORDEX (Giorgi et al., 2009). The divergence of ensemble model results provides an indication of the range of uncertainty if it is not known which of the models forming the ensemble are more reliable; however, it does not properly describe probabilities of the possible outcome because the ensemble of models does not constitute a valid statistical sample (Takayabu et al., 2016).

The setup for the simulations used in dynamical downscaling for wind resource assessment are in the intersection of NWP and traditional dynamical downscaling. The simulations are reinitialised often (1–10 days), but in most instances we are interested in their skill in representing the spatial and temporal distribution of wind speed and not the exact match between each simulated and observed instance (Hahmann et al., 2015b).

In a recent paper, Al-Yahyai et al. (2012) used an "ensemble" approach to simulate the wind speed climatology over Oman. They used an ensemble of four simulations with two large scale forcings and two regional models. They conclude that "The results proved the effectiveness for the proposed approach and showed that the Ensemble Mean Approach performed better in average than the Individual Members Approach." However, in their

context, the ensemble mean just smooths out the details of each individual ensemble member. In the context of forecasting, when the models are averaged, the RMSE improves because the resulting time series are smoother. In the wind climate sense, averaging does not necessarily improve the model biases.

5.4 WRF setup

We make a first attempt to examine whether using an ensemble of simulations combining multiple physics, land initial conditions and re-initialisation strategy can be used to reliably estimate the uncertainty of the wind resource.

In Table 5.1 are the various parameters modified among the simulations. We use three different PBL schemes: the Mellor-Yamanda (MYJ) scheme (Janjic, 2001), the MYNN scheme (Nakanishi and Niino, 2006) and the YSU scheme (Hong et al., 2006). The soil moisture in the simulations is initialized from the same source as the atmospheric initial conditions (e.g. ERA Interim; Dee et al., 2011) or from the Global Land Data Assimilation system (LGDAS, Rodell and et al, 2004). Lastly, the model re-initialization strategy is varied. The "10D" simulations are initialized at 00:00 GMT and run for 11 days, disregarding the first 24 hours; the "1D" simulations are initialized at 12:00 GMT and run for 36 hours, disregarding the first 12 hours.

Table 5.1 – Description of various WRF simulations

Run name	PBL scheme	soil moisture source	simulation length (days)
MYJ-G	MYJ	GLDAS	10
MYJ	MYJ	ERA	10
MYJ-D	MYJ	ERA	1
MYN-G	MYNN	GLDAS	10
MYN	MYNN	ERA	10
MYN-D	MYNN	ERA	1
YSU-G	YSU	GLDAS	10
YSU	YSU	ERA	10
YSU-D	YSU	ERA	1

The simulations were carried out for a domain over South Africa as part of the Wind Atlas of South Africa (WASA) project for the one period from 1 June 2012 to 31 May 2013. We choose this domain and period because as part of the WASA project provides a high-quality set of observations, which are currently not available for an European domain. The stations used for validation are described in Mortensen et al. (2014). The domain (with a horizontal grid spacing of 45, 15 and 5 km) and the location of the sites is shown in Fig. 5.1. The 10 masts are equipped with identical instrumentation where the top-most anemometer is at a height of between 61.5 and 62 m AGL.

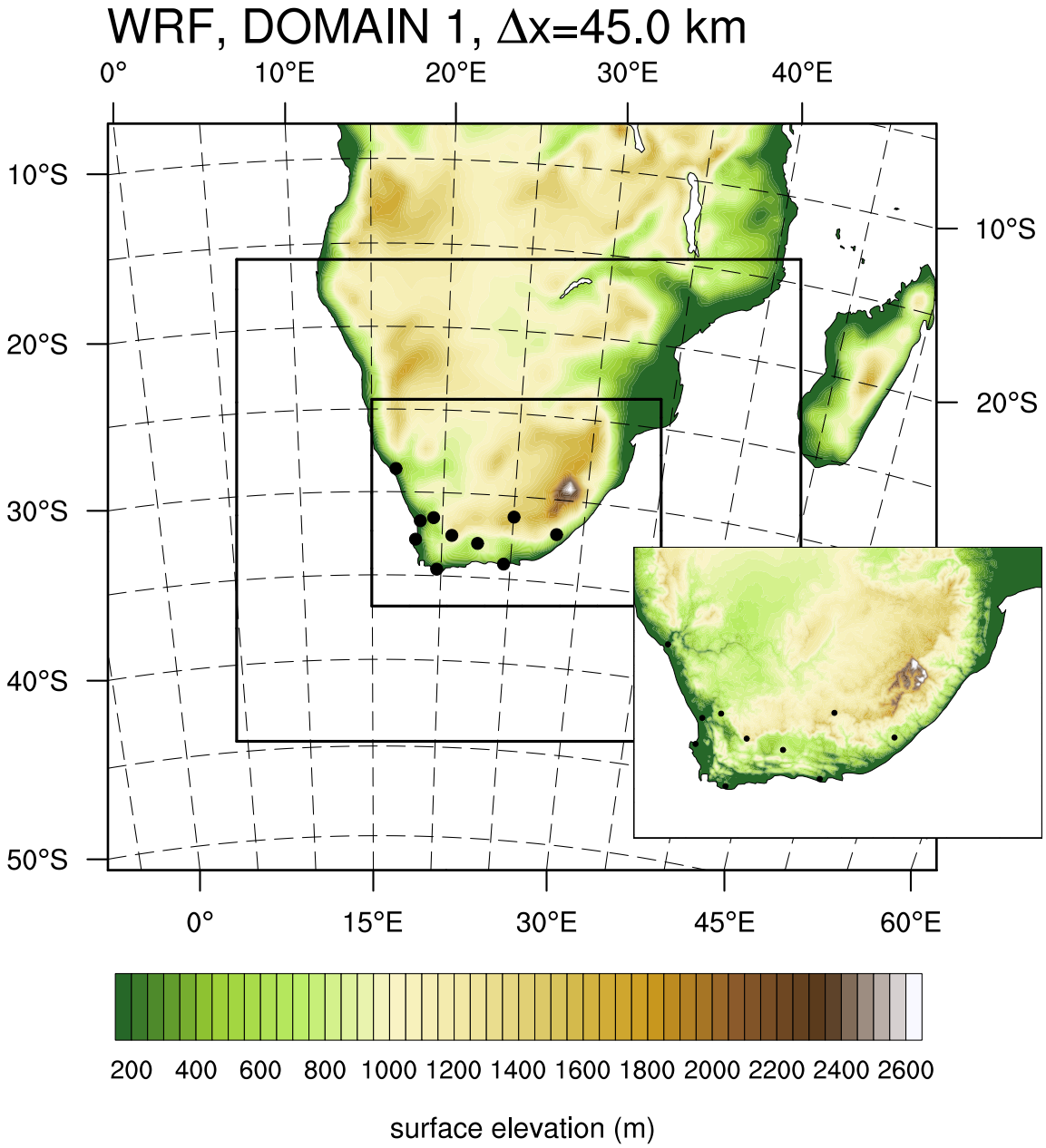

Figure 5.1 – Surface elevation (m) and domain configuration used in the WRF simulations. The black dots indicate the position of the 10 validation masts (WM01–WM10). The inset shows the surface elevation of the inner domain.

5.5 Results

Verification at sites

Figure 5.2 shows the mean bias in wind speed as defined

$$\text{Error} = (\overline{U}_{WRF} - \overline{U}_{OBS}) \tag{5.1}$$

$$\text{Relative Error} = (\overline{U}_{WRF} - \overline{U}_{OBS})/\overline{U}_{OBS}, \tag{5.2}$$

where $\overline{U}_{WRF}$ and $\overline{U}_{OBS}$ are the mean wind speed simulated by WRF and observed, respectively, at each of the sites. Positive errors mean that the WRF model overestimates the mean wind speed at the site. The observed means are computed as the simple arithmetic mean of the wind speed over all available measurements during the period 1 June 2012 to 31 May 2013. The WRF model estimate is obtained by direct downscaling of the inner grid (5 km horizontal resolution) model output to the site by the method described in Hahmann et al. (2019). Missing periods in the observations are removed from the time series of WRF model wind speeds, so that both samples are of equal size.

Figure 5.2 shows the errors and relative errors in mean wind speed at the height of the top anemometer (61.4–62 m) for the WRF output downscaled to each site, respectively. The errors are for all 9 simulations and 10 tall mast sites. The absolute errors are $<1\,\mathrm{m\,s^{-1}}$ at all sites and all model configurations, except for the MYJ-G run at WM03, and $<0.4\,\mathrm{m\,s^{-1}}$ for the combined MAE at all sites. For a given site, the errors may vary considerable among the various simulations, but the MAE is almost indistinguishable among them.

Figure 5.3 shows another way to look at the errors in Fig. 5.2. The errors are presented as boxplots, where the red line and red box show the median and mean error, respectively. The box boundaries represent the lower (25%) and upper (75%) quartiles, and the whiskers the minimum and maximum values. Here it is possible to see that on average the relative errors are smaller and have the smaller spread in the MYNN-based experiments.

Finally we can combine the error statistics as a function of site. This is done in Figure 5.4, where the y-axis now displays the absolute value of the mean error to facilitate interpretation. Four of the five sites with the smallest error spread are also the sites with the smallest mean error (except for WM01). The other five sites with larger spread are also the five sites with larger absolute mean error.

Another encouraging characteristic of the distribution of the errors is apparent in Fig. 5.2. For each site the performance of each simulation varies from site to site. For example, the MYN-D is "worst" simulation at WM01, but one of the "bests" at WM08. This characteristic of the errors suggest that one model configuration might be most accurate under certain conditions but worse under others. Thus, it might be possible to optimize the combination of the results to create a more precise wind atlas and to use the model spread as a measure for uncertainty.

Ensemble mean and spread

From the mean wind speed of each ensemble simulation, $\overline{U}_i$, it is possible to compute and plot the ensemble mean, $\tilde{U}$, and the ensemble spread, $S_{\tilde{U}}$, defined as

$$\tilde{U} = \frac{1}{N}\sum_{i=1}^{N}\overline{U}_i \tag{5.3}$$

$$S_{\tilde{U}} = \sqrt{\sum_{i=1}^{N}\frac{(\overline{U}_i - \tilde{U})^2}{N-1}}, \tag{5.4}$$

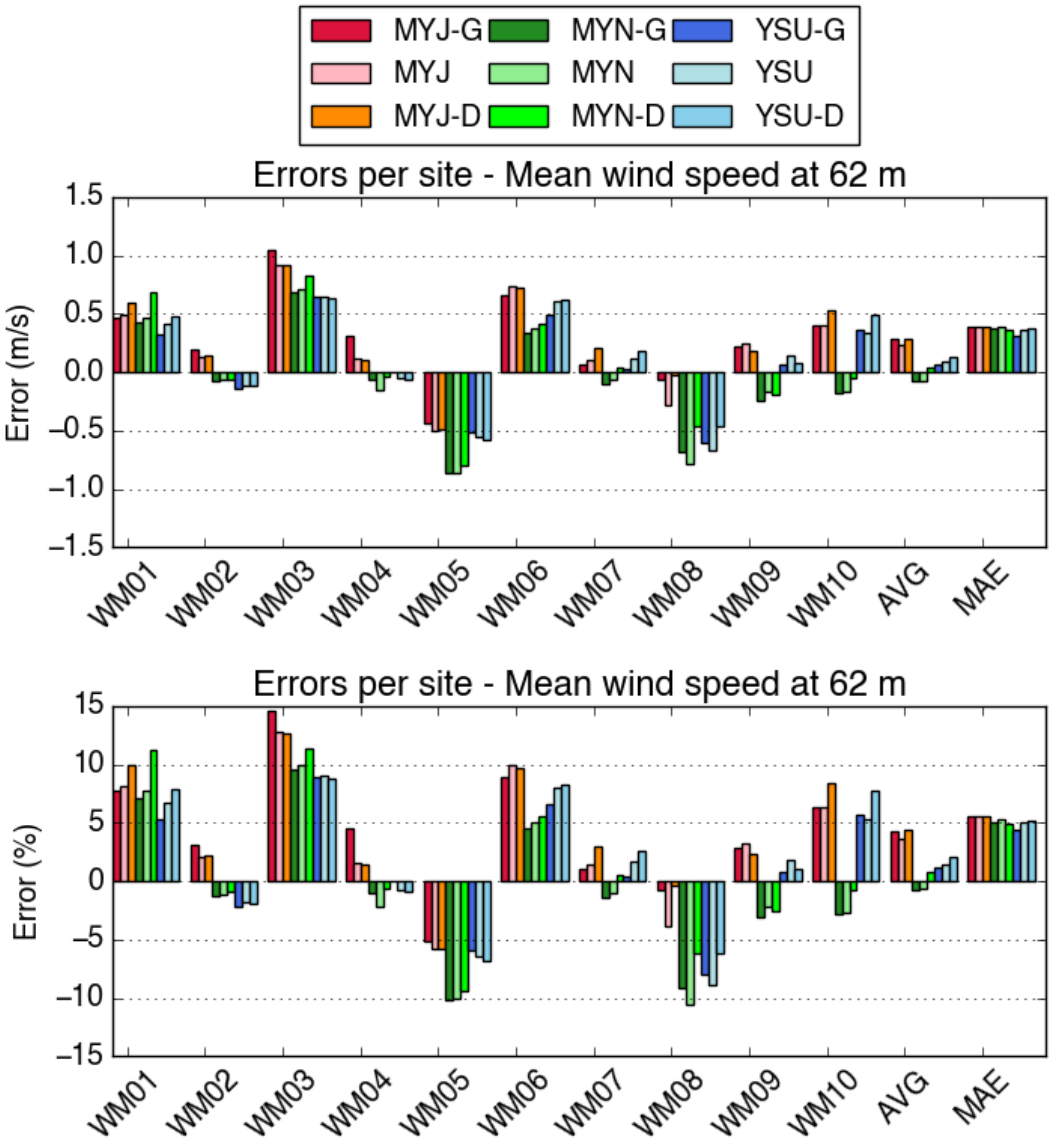

Figure 5.2 – Mean error (top; $\mathrm{m\,s^{-1}}$) and relative mean error (bottom; %) and in the downscaled wind speed at about 62 m for each ensemble member in Table 5.1 for each of the 10 WASA sites. The last two sets of bars represent the mean error (AVG) and the mean absolute error (MAE) over all the sites.

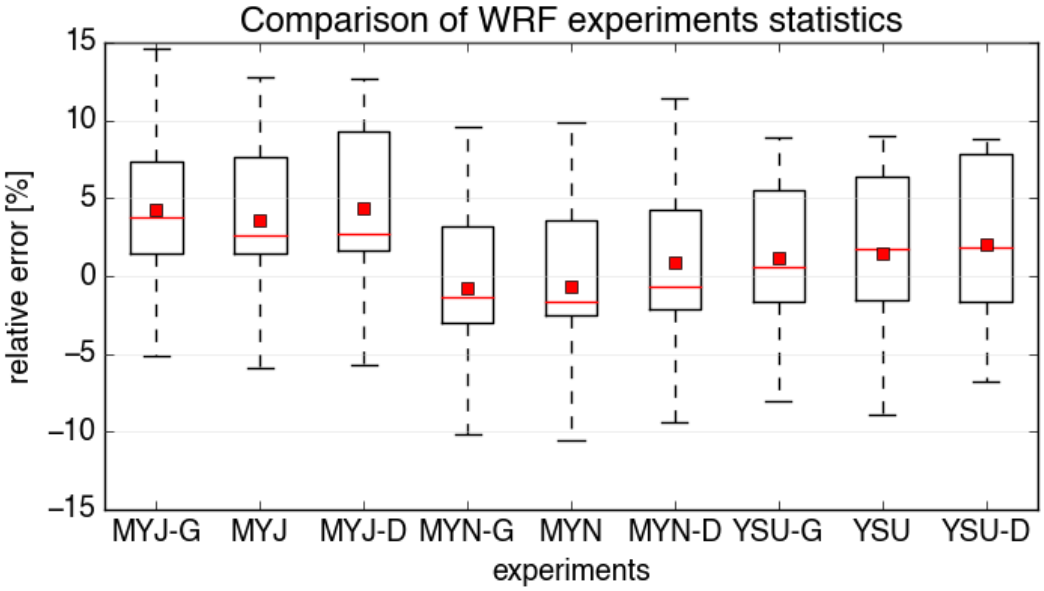

Figure 5.3 – Comparison of statistics of the wind speed errors for each ensemble member in Table 5.1. The meaning of the box is as in regular boxplots: the red line and red box show the median and mean error, respectively. The box boundaries represent the lower (25%) and upper (75%) quartiles, and the whiskers the minimum and maximum values.

Figure 5.4 – Comparison of statistics of the wind speed errors for each site of the various ensembles in Table 5.1. The meaning of the box is as in regular boxplots: the red line and red box show the median and mean error, respectively. The box boundaries represent the lower (25%) and upper (75%) quartiles, and the whiskers the minimum and maximum values.

where $N = 9$ is the total number of ensemble members. The ensemble spread is simply the standard deviation of the mean of the ensemble members.

Figure 5.5 shows the ensemble mean of wind speed at 100 m AGL for the 9 ensemble members. Wind speeds are high ($\lesssim 8\,\mathrm{m\,s^{-1}}$) over many areas of elevated terrain (see Fig. 5.1) and over the sea. The map of the ensemble mean shows many interesting features, which do not directly correspond to areas of complex terrain or high winds. It remains to be verified if these patterns are correlated with areas of reduced or enhanced uncertainties.

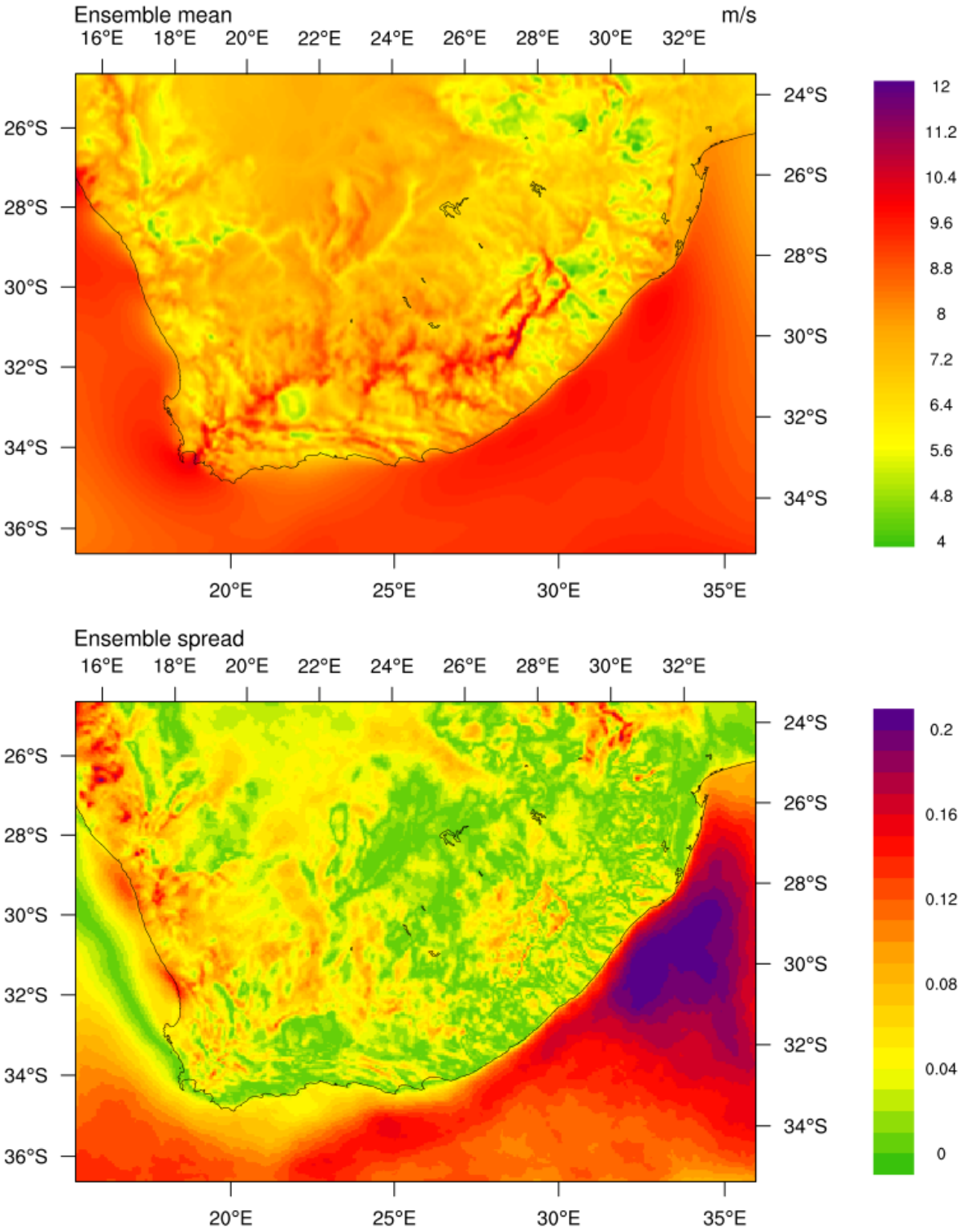

Figure 5.5 – Top: Ensemble mean, $\tilde{U}$, and Bottom: ensemble spread, $S_{\tilde{U}}$, of the wind speed ($\mathrm{m\,s^{-1}}$) at 100 m AGL for the period from 1 June 2012 to 31 May 2013.

5.5.1 Summary and discussion

We have performed a series of nine one year simulations with varied PBL schemes, simulation length and source of land surface conditions to explore the possibility of using an ensemble of runs to estimate the uncertainty of a wind resource map. The results of the simulations are encouraging, but further analysis of the results is necessary to quantify how useful they are.

The principal disadvantage of the use of the ensemble mean and spread of the simulations is that it can be misleading, and will not be the best estimate of the most accurate value and its uncertainty, if clusters of similar simulations outcomes exist, and the ensemble mean lies between those clusters. Therefore, it is vital to design an ensemble system where the ensemble members do not cluster around similar simulation outcomes. This is definitely not the case for the ensemble used in this report, because the errors do cluster as a function of PBL scheme (Fig. 5.2).

Since most ensembles using initial condition perturbations alone tend not to have enough spread, combined ensemble methods (i.e., a combination of perturbed initial conditions and physical parameterizations) should, at least theoretically, give better results in terms of covering all possible forecast outcomes.

5.5.2 Recommendations

We recommend to expand the ensemble members used in this study to:

- Use different reanalysis to initialise and nudge the WRF simulations, e.g. NOAA Climate Forecast System Reanalysis (CFSR) and Modern Era Retrospective-Analysis for Research and Applications (MERRA and MERRA2);
- Use the various ensemble members' output from the new reanalysis ERA5 (ECMWF, 2016), whose data products will include information about uncertainties, which will be provided for each parameter at 3-hourly intervals and at a horizontal resolution of 62 km.
- Find a method to quantify if two ensemble simulations are too similar and should be removed from the set;
- Identify potential statistical techniques (e.g. machine learning) to optimally combine the results from the various ensemble members into a single wind resource map.

Chapter 6

Long-term wind resources in South Africa

Maps of the WRF-based numerical wind atlas are now presented. The averages correspond to the period of simulation January 2010 to 31 December 2017. In the last section the variability in annual mean wind speed is shown for the 8 years of the simulation.

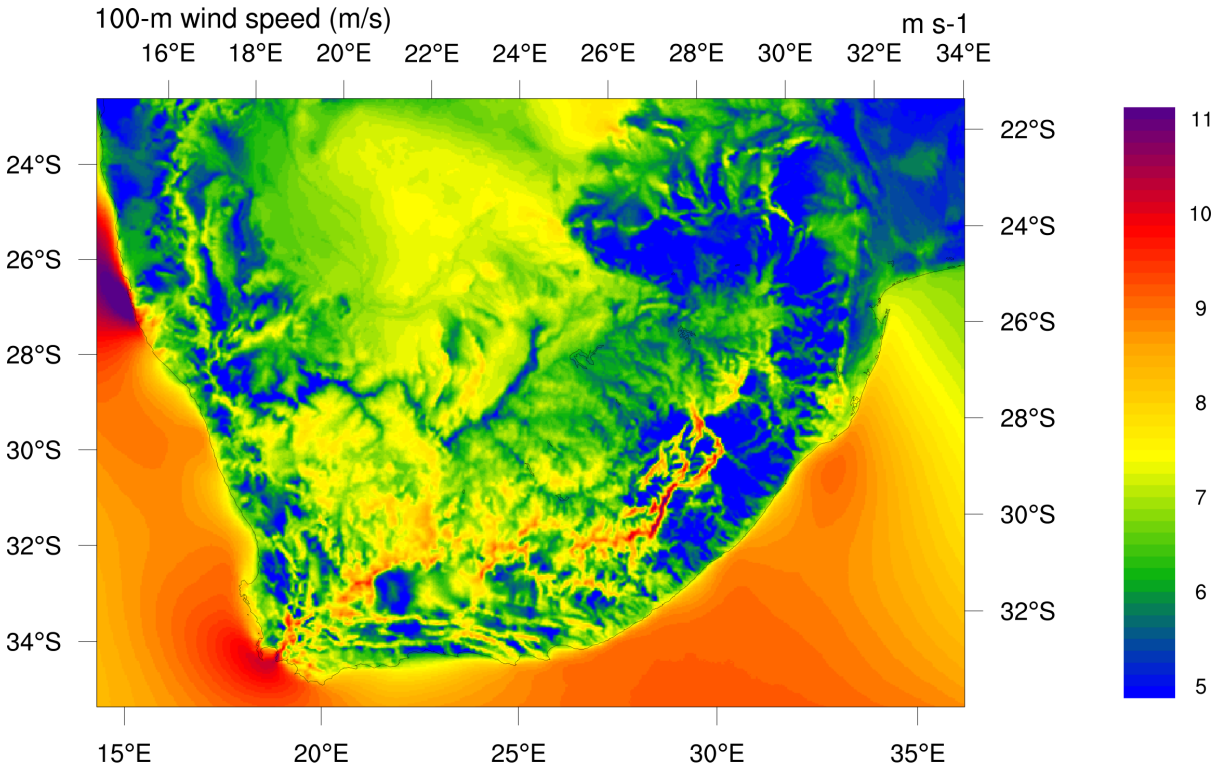

Figure 6.1 – Long-term (2010–2017) averaged wind speed ($m\,s^{-1}$) at 100 m AGL simulated by the WRF model.

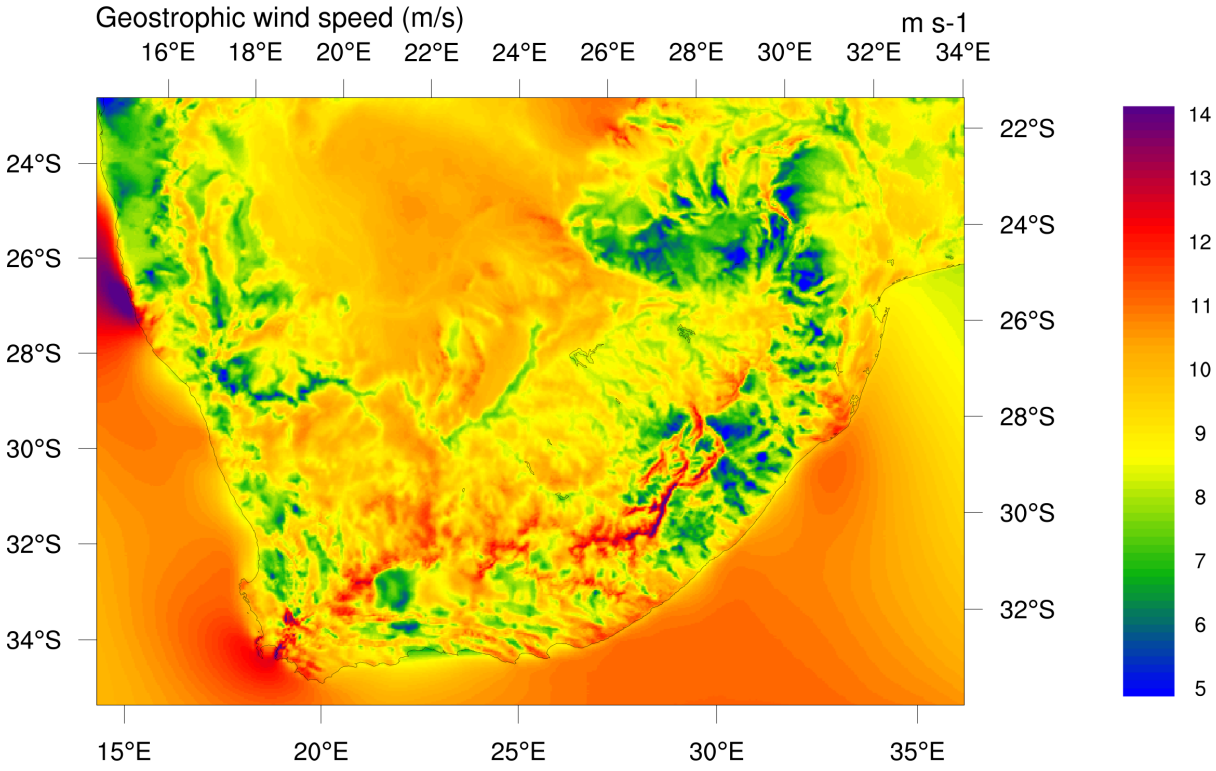

Figure 6.2 – Long-term (2010–2017) averaged geostrophic wind speed at 100 m AGL simulated by the WRF model.

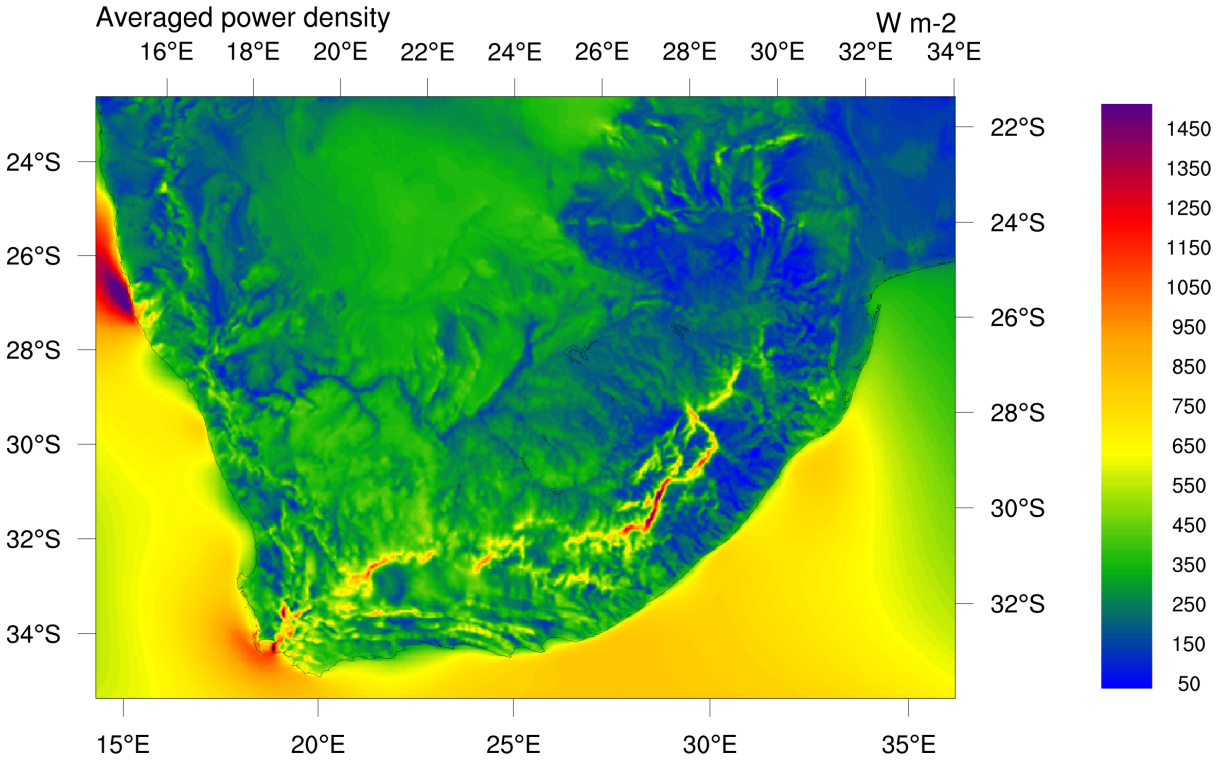

Figure 6.3 – Long-term (2010–2017) averaged power density ($W\,m^{-2}$) at 100 m AGL simulated by the WRF model.

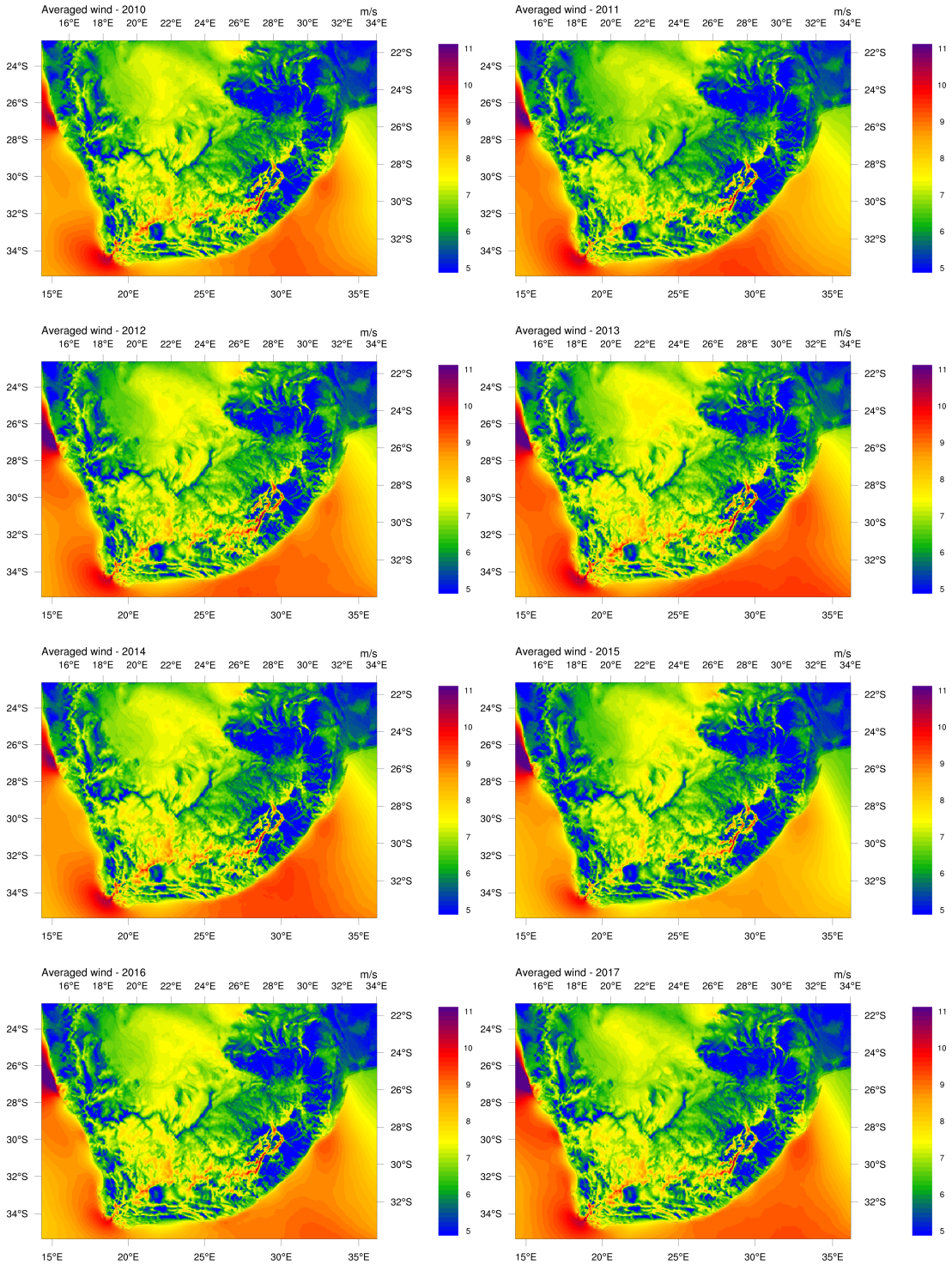

Figure 6.4 – Yearly (from 2010 to 2017) averaged wind speed at 100 m AGL simulated by the WRF model.

Chapter 7

Summary and conclusions

There have been various updates from the configuration of the WASA simulations in 2014 documented in Hahmann et al. (2015a). Among the most important:

1. Domain covering all South Africa at 3 1/3 km $\times$ 3 1/3 km grid spacing.
2. New atmospheric forcing data from latest reanalysis ERA5 at $0.3^\circ \times 0.3^\circ$ spacial resolution; new high-resolution OSTIA SST at a resolution of $1/20^\circ$ (approx. 5km).
3. New land cover and land use dataset from ESA/CCI at 300 m resolution.
4. Increased number of vertical levels, from 41 to 61, which results in a much smaller spacing between levels in the PBL.
5. Use of adaptive time step that considerably speeds up the simulations without lost of quality.
6. New PBL and surface layer parameterizations.
7. New translation table from ESA/CCI land cover types to land surface roughness length adapted for South Africa vegetation types (see section 3.3).

We have performed a series of nine one year simulations with varied PBL schemes, simulation length and source of land surface conditions to explore the possibility of using an ensemble of runs to estimate the uncertainty of a wind resource map. The results of the simulations are encouraging, but further analysis of the results is necessary to quantify how useful they are.

The WRF mesoscale analysis method, utilises the WRF mesoscale model to directly simulate atmospheric conditions over the region surrounding South Africa. In the WRF-based method there is, on average, a difference of 4.8% (either positive or negative) between the WRF-based wind climatology downscaled to the site and the corresponding observed values. The combined average across all the sites is an over-estimate of 1%. When comparing only the WASA1 sites (WM01–WM10), the MEA is 3.9%.

Many factors contribute to the uncertainty of the results. A few known sources errors in the WRF-based wind atlas are listed below:

1. Uncertainty in the forcing reanalysis.
   Due to the sparse observing system, the ERA5 reanalysis, while of superior quality than the previously used ERA-Interim reanalysis, is expected to contain larger errors in Southern Africa than in other parts of the world. These errors directly impact the quality of the WRF analyses.

2. Uncertainty in the WRF simulations:
   The veracity of the WRF simulations themselves, and how these vary with the various setting in the simulations, will introduce errors in the final wind atlas. For example, as seen in the ensemble model results (5.5) show large differences for specific sites. However, when the errors are averaged over all sites, the differences are rather small.

3. Representativeness of the simulated period:
   An additional error is introduced in the estimates derived from the WRF simulations because only eight years (2010–2017) are used. This error is expected to be small, however, to quantify it, an analysis of the representativeness of these 8 years in the long-term wind climatology will have to be carried out.

4. Errors in the generalisation method:
   The generalisation method used was originally developed for use within the KAMM model infrastructure (see Chapter 2). We later adapted it for use with the WRF model output, and, because the models and the simulating methods are different in the two models, additional errors can be introduced. Several constants were used in the generalisation procedure, which can considerably change the downscalled results. Further evaluation of these options is required.

Bibliography

Al-Yahyai, S., Y. Charabi, A. Al-Badi, and A. Gastli, 2012: Nested ensemble NWP approach for wind energy assessment. *Renew. Energy*, **37**, 150–160.
URL http://dx.doi.org/10.1016/j.renene.2011.06.014

Badger, J., H. Frank, A. N. Hahmann, and G. Giebel, 2014: Wind-climate estimation based on mesoscale and microscale modeling: Statistical-dynamical downscaling for wind energy applications. *Journal of Applied Meteorology and Climatology*, **53**, 1901–1919.
URL http://journals.ametsoc.org/doi/abs/10.1175/JAMC-D-13-0147.1

Berner, J., S.-Y. Ha, J. P. Hacker, A. Fournier, and C. Snyder, 2011: Model Uncertainty in a Mesoscale Ensemble Prediction System: Stochastic versus Multiphysics Representations. *Mon. Weather Rev.*, **139**, 1972–1995.
URL http://journals.ametsoc.org/doi/abs/10.1175/2010MWR3595.1

Buizza, R., P. L. Houtekamer, G. Pellerin, Z. Toth, Y. Zhu, and M. Wei, 2005: A Comparison of the ECMWF, MSC, and NCEP Global Ensemble Prediction Systems. *Mon. Weather Rev.*, **133**, 1076–1097.

Deacon, E. L., 1973: Geostrophic drag coefficients. *Boundary-Layer Meteorol.*, **5**, 321–340.

Dee, D. P., S. M. Uppala, A. J. Simmons, P. Berrisford, P. Poli, S. Kobayashi, U. Andrae, M. A. Balmaseda, et al., 2011: The ERA-Interim reanalysis: configuration and performance of the data assimilation system. *Q. J. R. Meteorol. Soc.*, **137**, 553–597.
URL http://doi.wiley.com/10.1002/qj.828

Donlon, C. J., M. Martin, J. D. Stark, J. Roberts-Jones, E. Fiedler, and W. Wimmer, 2011: The operational sea surface temperature and sea ice analysis (ostia). *Remote Sensing of the Environment*.

ECMWF, 2016: ERA5 reanalysis is in production.
URL http://www.ecmwf.int/en/newsletter/147/news/era5-reanalysis-production

Floors, R., 2013: Measuring and modelling of the wind on the scale of tall wind turbines. PhD-0034(EN). Phd, Technical University of Denmark.

Gill, A. E., 1968: Similarity theory and geostrophic adjustment. *Q. J. R. Meteorol. Soc.*, **94**, 586–588.

Giorgi, F., C. Jones, and G. R. Asrar, 2009: Addressing climate information needs at the regional level: the CORDEX framework. *Bull. - World Meteorol. Organ.*, **58**, 175–183.

Hahmann, A. N., J. Badger, C. L. Vincent, M. C. Kelly, P. J. H. Volker, and J. Refslund, 2015a: Mesoscale modeling for the wind atlas for South Africa (WASA) Project. Tech. rep., DTU Wind Energy.
URL http://orbit.dtu.dk/services/downloadRegister/107110172/DTU_Wind_Energy_E_0050.pdf

Hahmann, A. N., D. Rostkier-Edelstein, T. T. Warner, F. Vandenberghe, Y. Liu, R. Babarsky, and S. P. Swerdlin, 2010: A Reanalysis System for the Generation of Mesoscale Climatographies. *Journal of Applied Meteorology and Climatology*, **49**, 954–972.
URL http://journals.ametsoc.org/doi/abs/10.1175/2009JAMC2351.1

Hahmann, A. N., C. L. Vincent, A. Peña, J. Lange, and C. B. Hasager, 2015b: Wind climate estimation using WRF model output: Method and model sensitivities over the sea. *Int. J. Climatol.*, **35**, 3422–3439.
URL http://dx.doi.org/10.1002/joc.4217

Hahmann, A. N., C. L. Vincent, A. Peña, J. Lange, and C. B. Hasager, 2015c: Wind climate estimation using WRF model output: Method and model sensitivities over the sea. *International Journal of Climatology*, **35**, 3422–3439.

Hahmann, A. N., P. J. H. Volker, J. Badger, N. G. Mortensen, and D. C. J. Schillebeeckx, 2019: Generalization of wrf-derived wind climatologies for validation and coupling of mesoscale and microscale models. *Wind Energy Science*, **In preparation**.

Hong, S.-Y., Y. Noh, and Dudhia., 2006: A new vertical diffusion package with an explicit treatment of entrainment processes. *Mon. Wea. Rev.*, **134**, 2318–2341.

IPCC, 2013: Climate Change 2013: The Physical Science Basis. Contribution of Working Group I to the Fifth Assessment Report of the Intergovernmental Panel on Climate Change. Tech. rep., Cambridge University Press, Cambridge, United Kingdom and New York, NY, USA.

Janjic, Z. I., 2001: Nonsingular implementation of the Mellor-Yamada level 2.5 scheme in the NCEP Meso model. Tech. rep., National Centers for Environmental Prediction: Camp Springs, MD, USA.

Kelly, M. and I. Troen, 2016: Probabilistic stability and "tall" wind profiles: theory and method for use in wind resource assessment. *Wind Energy*, **19**, 227–241.

Kristensen, L. and G. Jensen, 1999: Geostrophic winds in Denmark : a preliminary study. Risø-R-1145(EN). Tech. Rep. November, Risø National Laboratory, Roskilde, Denmark.

Lee, J. A., W. C. Kolczynski, T. C. McCandless, and S. E. Haupt, 2012: An objective methodology for configuring and down-selecting an NWP ensemble for low-level wind prediction. *Mon. Weather Rev.*, **140**, 2270–2286.
URL http://journals.ametsoc.org/doi/abs/10.1175/MWR-D-11-00065.1

Lorenz, E. N., 1969: The predictability of a flow which possesses many scales of motion. *Tellus*, **21**, 289–307.
URL http://tellusa.net/index.php/tellusa/article/view/10086

Mortensen, N. G., J. C. Hansen, and M. C. Kelly, 2014: Wind Atlas for South Africa (WASA) Western Cape and parts of Northern and Eastern Cape Observational Wind Atlas for 10 Met. Masts in Northern, Western and Eastern Cape Provinces. Tech. Rep. April, DTU Wind Energy.

Murphy, J. M., D. M. H. Sexton, D. N. Barnett, G. S. Jones, M. J. Webb, M. Collins, and D. A. Stainforth, 2004: Quantification of modelling uncertainties in a large ensemble of climate change simulations. *Nature*, **430**, 768–772.
URL http://www.ncbi.nlm.nih.gov/pubmed/15306806http://www.nature.com/doifinder/10.1038/nature02771

Nakanishi, M. and H. Niino, 2006: An Improved Mellor-Yamada Level-3 Model: Its Numerical Stability and Application to a Regional Prediction of Advection Fog. *Boundary-Layer Meteorol.*, **119**, 397–407.
URL http://www.springerlink.com/content/j04441r721280776/

Nawri, N., G. N. Petersen, H. Bjornsson, A. N. Hahmann, K. Jónasson, C. B. Hasager, and N.-E. Clausen, 2014: The wind energy potential of Iceland. *Renewable Energy*, **69**, 290–299.
URL http://linkinghub.elsevier.com/retrieve/pii/S0960148114002043

Niino, H. and M. Nakanishi, 2006: An Improved Mellor–Yamada Level-3 Model: Its Numerical Stability and Application to a Regional Prediction of Advection Fog. *Boundary-Layer Meteorol.*, **119**, 397–407.
URL http://link.springer.com/10.1007/s10546-005-9030-8

Palmer, T. N., 2001: A nonlinear dynamical perspective on model error: A proposal for non-local stochastic-dynamic parametrization in weather and climate prediction models. *Q. J. R. Meteorol. Soc.*, **127**, 279–304.
URL http://doi.wiley.com/10.1002/qj.49712757202

Rodell, M. and et al, 2004: The global land data assimilation system. *Bull. Am. Meteorol. Soc.*, **85**, 381–394.

Skamarock, W. C., J. B. Klemp, J. Dudhia, D. O. Gill, D. M. Barker, M. G. Duda, X.-Y. Huang, W. Wang, et al., 2008: A Description of the Advanced Research WRF Version 3. Tech. Rep. NCAR/TN–475+STR, National Center for Atmospheric Research.

Stainforth, D. A., T. Aina, C. Christensen, M. Collins, N. Faull, D. J. Frame, J. A. Kettleborough, S. Knight, et al., 2005: Uncertainty in predictions of the climate response to rising levels of greenhouse gases. *Nature*, **433**, 403–6.
URL http://dx.doi.org/10.1038/nature03301

Takayabu, I., H. Kanamaru, K. Dairaku, R. Benestad, H. von Storch, and J. H. Christensen, 2016: Reconsidering the Quality and Utility of Downscaling. *J. Meteorol. Soc. Japan. Ser. II*, **94A**, 31–45.
URL https://www.jstage.jst.go.jp/article/jmsj/94A/0/94A{_}2015-042/{_}article

Tammelin, B., T. Vihma, E. Atlaskin, J. Badger, C. Fortelius, H. Gregow, M. Horttanainen, R. Hyvönen, et al., 2012: Production of the finnish wind atlas. *Wind Energy*, n/a–n/a. URL `http://dx.doi.org/10.1002/we.517`

Troen, I. and E. L. Petersen, 1989: *European Wind Atlas*. Published for the Commission of the European Communities, Directorate-General for Science, Research, and Development, Brussels, Belgium by Risø National Laboratory.

Tuller, S. E. and A. C. Brett, 1984: The characteristics of wind velocity that favor the fitting of a Weibull distribution in wind-speed analysis. *J. Appl. Meteor. Clim.*, **23**, 124–134.

Appendix A

WRF namelist

```
&time_control
 interval_seconds                    = 21600,
 input_from_file                     = .T., .T., .T.,
 history_interval                    = 60, 60, 30,
 frames_per_outfile                  = 12, 12, 12,
 restart                             = .false.,
 restart_interval                    = 100000,
 io_form_history                     = 2
 io_form_restart                     = 2
 io_form_input                       = 2
 io_form_boundary                    = 2
 auxinput4_inname                    = "wrflowinp_d<domain>",
 auxinput4_interval                  = 360,360,360,
 io_form_auxinput4                   = 2,
 iofields_filename                   = "WAFields.txt","WAFields.txt","WAFields.txt",
 ignore_iofields_warning             = .true.,
 debug_level                         = 0,
/

&domains
 max_dom                             = 3,
 time_step                           = 90,
 use_adaptive_time_step              = .true.,
 step_to_output_time                 = .true.,
 target_cfl                          = 0.84, 0.84, 0.84,
 target_hcfl                         = 0.84, 0.84, 0.84,
 max_step_increase_pct               =    5,  51,  51,
 starting_time_step                  =  120,  40,  13,
 max_time_step                       =  180,  60,  20,
 min_time_step                       =   36,  12,   4,
 adaptation_domain                   =   1,
 parent_id                           =   1,    1,   2,
 parent_grid_ratio                   =   1,    3,   3,
```

```
 e_sn                                = 140,271,454,
 e_we                                = 160,331,631,
 i_parent_start                      =   1,   25,  60,
 j_parent_start                      =   1,   25,  60,
 s_sn                                =    1,   1,   1,
 s_we                                =    1,   1,   1,
 e_vert                              =   61,  61,  61,
 grid_id                             =    1,   2,   3,
 parent_time_step_ratio              =    1,   3,   3,
 num_metgrid_levels                  = 33,
 num_metgrid_soil_levels             = 4,
 dx                                  = 30000.,10000.,3333.333,
 dy                                  = 30000.,10000.,3333.333,
 p_top_requested                     = 5000,
 eta_levels = 1.000000, 0.998600, 0.996000, 0.994000, 0.992000,
              0.990000, 0.987592, 0.984486, 0.980977, 0.977016,
              0.972544, 0.967500, 0.961813, 0.955403, 0.948185,
              0.940062, 0.930929, 0.920670, 0.909158, 0.896257,
              0.881820, 0.859633, 0.830162, 0.794019, 0.751945,
              0.704330, 0.659043, 0.615990, 0.575078, 0.536219,
              0.499329, 0.464324, 0.431126, 0.399657, 0.369845,
              0.341616, 0.314904, 0.289641, 0.265763, 0.243210,
              0.221922, 0.201841, 0.182641, 0.164410, 0.148206,
              0.132526, 0.117709, 0.104002, 0.091398, 0.079808,
              0.069150, 0.059351, 0.050340, 0.042054, 0.034434,
              0.027428, 0.020986, 0.015062, 0.009615, 0.004606,
              0.000000,
 smooth_option = 2,
 feedback = 0,
/

&physics
 mp_physics                          =  4,  4,  4,
 ra_lw_physics                       =  4,  4,  4,
 ra_sw_physics                       =  4,  4,  4,
 radt                                = 12,  9,  3,
 swint_opt                           =  1,
 sf_surface_physics                  =  2,  2,  2,
 sf_sfclay_physics                   =  5,  5,  5,
 bl_pbl_physics                      =  5,  5,  5,
 bl_mynn_mixlength                   =  0,
 bldt                                =  0,  0,  0,
 cu_physics                          =  1,  1,  0,
 cudt                                =  5,  5,  5,
 fractional_seaice                   = 1,
 tice2tsk_if2cold                    = .true.,
```

```
 seaice_threshold                    = 0.,
 isfflx                              = 1,
 icloud                              = 1,
 surface_input_source                = 1,
 num_land_cat                        = 28,
 num_soil_layers                     = 4,
 sst_update                          = 1,
 ensdim                              = 144,
 prec_acc_dt                         = 60, 60, 30,
/
&fdda
 grid_fdda                           = 2,     0,    0,
 gfdda_inname                        = "wrffdda_d<domain>",
 gfdda_end_h                         = 300,   0,    0,
 gfdda_interval_m                    = 360,   0,    0,
 fgdt                                = 0,     0,    0,
 if_no_pbl_nudging_uv                = 0,     0,    0,
 if_no_pbl_nudging_t                 = 1,     0,    0,
 if_no_pbl_nudging_q                 = 1,     0,    0,
 if_zfac_uv                          = 1,     0,    0,   0,
  k_zfac_uv                          = 20,    0,    0,   0,
 if_zfac_t                           = 1,     0,    0,   0,
  k_zfac_t                           = 20,    0,    0,   0,
 if_zfac_q                           = 1,     0,    0,   0,
  k_zfac_q                           = 20,    0,    0,   0,
 guv                                 = 0.0003, 0.000075, 0.000075,
 gt                                  = 0.0003, 0.000075, 0.000075,
 gq                                  = 0.0003, 0.000075, 0.000075,
 xwavenum                            = 14,
 ywavenum                            = 10,
 if_ramping                          = 0,
 dtramp_min                          = 60.0,
 io_form_gfdda                       = 2,
/

&dynamics
 w_damping                           = 1,
 diff_opt                            = 1,
 km_opt                              = 4,
 diff_6th_opt                        = 2,    2,    2,
 diff_6th_factor                     = 0.06, 0.08, 0.1,
 base_temp                           = 290.
 damp_opt                            = 0,
 zdamp                               = 5000., 5000., 5000.,
 dampcoef                            = 0.15,  0.15,  0.15,
 khdif                               = 0,     0,    0,
```

```
 kvdif                               = 0,     0,    0,
 non_hydrostatic                     = .true.,.true.,.true.,
 moist_adv_opt                       = 1,     1,    1,
 scalar_adv_opt                      = 1,     1,    1,
/
&bdy_control
 spec_bdy_width                      = 5,
 spec_zone                           = 1,
 relax_zone                          = 4,
 specified                           = .true., .false.,.false.,
 nested                              = .false., .true., .true.,
/
&grib2
/
&namelist_quilt
  nio_tasks_per_group = 0,
  nio_groups = 1,
/
```

Mesoscale Modelling for the Wind Atlas of South Africa (WASA) Project – Phase II

DTU Wind Energy is a department of the Technical University of Denmark with a unique integration of research, education, innovation and public/private sector consulting in the field of wind energy. Our activities develop new opportunities and technology for the global and Danish exploitation of wind energy. Research focuses on key technical-scientific fields, which are central for the development, innovation and use of wind energy and provides the basis for advanced education at the education.

We have more than 230 staff members of which approximately 40 are PhD students. Research is conducted within ten research programmes organized into three main topics: Wind energy systems, Wind turbine technology and Basics for wind energy.

Technical University of Denmark
Department of Wind Energy
Frederiksborgvej 399
Building 118
4000 Roskilde
Denmark
Telephone 46 77 50 85

info@vindenergi.dtu.dk
www.vindenergi.dtu.dk